Promoter Decoding of Transcription Factor Localization Dynamics and DNA Binding

By

Kieran Sweeney

A dissertation submitted in partial fulfillment of

the requirements for the degree of

Doctor of Philosophy

(Biomedical Engineering)

at the

UNIVERSITY OF WISCONSIN-MADISON

2022

Date of final oral examination: 8/17/2022

The dissertation is approved by the following members of the Final Oral Committee:

Megan N. McClean, Associate Professor, Biomedical Engineering
Pamela K. Kreeger, Professor, Biomedical Engineering
Krishanu Saha, Associate Professor, Biomedical Engineering
Matthew J. Merrins, Associate Professor, Biomolecular Chemistry
Kevin W. Eliceiri, Professor, Biomedical Engineering

Abstract

A growing number of studies have shown that cells may encode environmental information in the temporal dynamics of transcription factor (TF) activation and that downstream genes can decode these dynamics to enact an appropriate gene expression response. Most of these studies have focused on the encoding and decoding of information in TF nuclear localization dynamics, yet cells control the activity of TFs in myriad other ways, including by regulating their ability to bind DNA. Therefore, the aim of this thesis was to investigate the decoding of TF activity dynamics by promoters and examine how decoding is affected by changes in the ability of the TF to bind DNA. To do this, we first created a light-controlled mutant of the *Saccharomyces cerevisiae* general stress response TF Msn2 and measured the expression of its target genes following defined patterns of nuclear localization generated with time-varying light doses. Using a mathematical model of gene expression, we categorized the genes based on how they filtered Msn2 nuclear localization dynamics: high sensitivity genes were readily induced by nuclear Msn2, while low sensitivity genes filtered out low amplitude, short duration, or pulsatile doses of nuclear Msn2. Our model predicted that changes in the ability of Msn2 to bind DNA would have a stronger effect on the expression of low sensitivity genes than high sensitivity genes. To test this prediction, we created light-controlled Msn2 mutants with an increased or decreased ability to bind DNA and measured how Msn2 target genes decoded their nuclear localization dynamics. These experiments showed that such changes indeed had a stronger effect on the low sensitivity genes and that increasing the ability of Msn2 to bind DNA generally increased the expression of its target genes, making them less noisy and more responsive to shorter, weaker, and pulsatile doses of nuclear Msn2. We also found that the relative ability to respond to pulsatile versus continuous doses of nuclear Msn2 was set largely by the promoter, rather than the TF. Subsequent analysis of our gene expression model indicated that a low sensitivity to Msn2, slow activation kinetics, or fast deactivation kinetics may cause a promoter to exhibit divergent responses to Msn2 mutants with different DNA binding abilities. We also reasoned that changing the ability of Msn2 to bind DNA would disrupt the ability of its target genes to decode nuclear localization dynamics generated by environmental stress. Indeed, measurements of gene expression following glucose starvation and hyperosmotic shock revealed that increasing the ability of Msn2 to bind DNA disrupted the ability of some promoters to discriminate between the two stresses. Lastly, over the course of our experiments we found evidence that nuclear localization triggers the degradation of Msn2, which may act as a timer on the expression of genes that require high levels of nuclear Msn2 to activate. Overall, this thesis contributes to the growing understanding how promoters decode TF localization dynamics and points to strategies by which cells, or biomedical engineers, may control both TF localization dynamics and DNA binding to enact specific gene expression programs.

Acknowledgements

I count myself lucky to have had the opportunity and support to pursue the work presented in this thesis. I am grateful to my advisor, Professor Megan McClean, for giving me that opportunity and her generous help and guidance ever since. Thank you.

I would also like to thank the members of my committee, Professors Pamela Kreeger, Krishanu Saha, Matthew Merrins, Audrey Gasch, and Kevin Eliceiri, for their time and their insights; Professor Walter Block for encouraging me to apply to graduate school; and Professor David Schwartz and Dr Louise Pape for the opportunity to participate in the Genomic Sciences Training Program.

To all members of the McClean Lab, past and present, thank you for the help, feedback, and genial spirit of our lab. I am especially grateful to Stephanie Geller for patiently helping me find my feet in lab and Taylor Scott for his countless insights.

I am also grateful to Lindsey Osimiri and Professor Hana El-Samad for providing us with their CLASP plasmid and Edvard Grødem, who created or refined some of the tools I counted on to do my experiments, even after a pandemic dispatched him back to Norway and off the UW payrolls.

Above all, I would like to thank my parents, my wife Lesley, and son Cillian for their love, support, and especially their patience over the long, irregular hours I spent bothering yeast.

This research was supported by an NHGRI training grant to the Genomic Sciences Training Program (5T32HG002760).

List of abbreviations

AUC	area under curve
CLASP	controllable light-activated shuttling and plasma membrane sequestration
DBD	DNA binding domain
ESR	environmental stress response
LANS	light-activated nuclear shuttle
LFM	low fluorescence media
LINUS	light induced nuclear localization signal
LPA	light plate apparatus
NES	nuclear export signal
NLS	nuclear localization signal
ORF	open reading frame
PKA	protein kinase A
PP1/2	protein phosphatase 1/2
PTM	post-translational modification
PWM	pulse width modulation
STRE	stress response element
TAD	transactivation domain
TF	transcription factor

List of figures

Figure 2.1 Encoding cellular information in TF activity dynamics. 5

Figure 2.2 Studying TF dynamics. 7

Figure 3.1 LPA calibration process. 12

Figure 3.2 Results of LPA calibration...14

Figure 3.3 LPA standard curve. 15

Figure 3.4 Irradiance before and after calibration. 16

Figure 3.5 Testing LPA calibration with an optogenetic system. 17

Figure 4.1 Automated measurement of optoPlate LEDs. 20

Figure 4.2 Calibrating optoPlate LEDs...21

Figure 4.3 Validating optoPlate calibration. 22

Figure 4.4 Measuring optoPlate dose-response relationship..23

Figure 5.1 Controlling Msn2 localization with CLASP...36

Figure 5.2 Optimizing Msn2 for optogenetic control. 37

Figure 5.3 Screening Msn2 mutants. 38

Figure 5.4 Dose-response of Msn2 ± CLASP mutants. 39

Figure 5.5 Light sweep experiments for Msn2*...40

Figure 5.6 Gene expression model. 41

Figure 5.7 Top promoter parameters. 42

Figure 5.8 Categorizing Msn2 target promoters. 43

Figure 5.9 Localization triggered degradation of Msn2. 46

Figure 5.10 Predicted versus measured expression of Msn2 affinity mutants...........................47

Figure 5.11 Msn2 DBD mutants..48

Figure 5.12 Light sweep experiments for all Msn2 DBD mutants. 49

Figure 5.13 Signal decoding behavior of high and low sensitivity promoters. 50

Figure 5.14 Degradation causes expression of low sensitivity promoters to plateau.................52

Figure 5.15 Promoter response to continuous versus pulsed Msn2. 53

Figure 5.16 Mutating Msn2 DBD versus mutating promoter. 54

Figure 5.17 Expression noise increased for pulsatile dynamics and decreased Msn2 affinity ...55

Figure 5.18 Modeling DNA binding differences between Msn2 DBD mutants. 57

Figure 5.19 Sensitivity analysis of gene expression model. 58

Figure 5.20 Expression for Msn2 DBD mutants diverges at low pulse amplitudes. 59

Figure 5.21 Changing Msn2 affinity affects discrimination of stresses by promoters. 61

Figure 5.22 Expression measurements and model fits for low sensitivity promoters.................67

Figure 5.23 Expression measurements and model fits for mid sensitivity promoters. 68

Figure 5.24 Expression measurements and model fits for high sensitivity promoters. 69

Figure 5.25 Overview of light programs and Msn2 localization timecourses. 70

Figure 5.26 Light sweep experiment reporters and controls. 71

Figure 5.27 Scaling K and n in gene expression model. 71

Figure 5.28 Calculating amplitude and duration thresholds. 72

Figure 5.29 Addition Msn2 degradation timecourses. 73

Figure 5.30 Amplitude thresholds and activation timescales for all Msn2 DBD mutants. 74

Figure 5.31 Expression versus noise. 74

Figure 5.32 Modeling binding differences between Msn2 mutants (additional details). 75

Figure 5.33 Predicted maximum expression of selected hypothetical promoters. 76

Figure 5.34 Predicted expression of hypothetical promoters versus nuclear localization. 77

Figure 5.35 Reporter expression and Msn2 localization for glucose starvation and salt shock..78

Table of contents

Abstract .... **i**

Acknowledgements .... **iii**

List of abbreviations .... **iv**

List of figures .... **v**

Table of contents .... **vii**

Chapter 1 : Thesis overview **1**

1.1 Introduction 1

1.2 Key findings 2

Chapter 2 : Background **4**

2.1 Encoding cellular information in transcription factor dynamics 4

2.2 Studying TF localization dynamics 7

2.3 Other cellular mechanisms for regulating TF activity 9

Chapter 3 : Calibrating and standardizing a light plate apparatus **10**

3.1 Introduction 10

3.2 Calibrating an LPA 12

3.3 Standard curve procedure 13

3.4 Method Validation 13

3.5 Conclusion 17

Chapter 4 : Calibrating and characterizing the light output of an optoPlate **18**

4.1 Introduction 18

4.2 Automated measurement of optoPlate LEDs 19

4.3 Calibrating optoPlate LEDs 20

4.4 Validating optoPlate calibration 21

4.5 Measuring the optoPlate dose-response relationship 22

4.6 Conclusion..24

Chapter 5 : Promoter decoding of TF dynamics and DNA binding........................ 25

5.1 Introduction..25

5.2 Methods..27

5.2.1 Strain construction 27

5.2.2 Blue light delivery..29

5.2.3 Light sweep experiments 29

5.2.4 Flow cytometry experiments with natural stress 33

5.2.5 Gene expression model..35

5.3 Results 36

5.3.1 Construction and optimization of a light-controlled Msn2 36

5.3.2 Light sweep experiments reveal promoter decoding of Msn2 localization dynamics .40

5.3.3 Categorizing promoters based on their sensitivity to Msn2 42

5.3.4 Nuclear localization triggers Msn2 degradation..45

5.3.5 Changing DNA-binding ability of Msn2 has strongest effect on low sensitivity genes 47

5.3.6 Relative ability to respond to pulsed versus continuous doses of nuclear Msn2 is primarily set by the promoter 52

5.3.7 Expression noise increased for pulsatile dynamics and low Msn2 affinity.................55

5.3.8 Sensitivity analysis reveals that slow activation or fast deactivation kinetics cause the relative expression for the Msn2 DBD mutants to diverge 56

5.3.9 Changing Msn2 affinity alters a promoter's ability to discriminate between stresses 60

5.4 Discussion 62

5.5 Supplementary figures 67

Chapter 6 : Conclusions and future directions 79

6.1 Introduction 79

6.2 Promoter decoding of Msn2 localization dynamics 80

6.3 The role of DNA binding affinity in promoter decoding of TF localization dynamics 82

6.4 Potential applications of our work 83

6.5 Localization triggered degradation of Msn2 83

Appendix 86

A.1 The cellular role of Msn2 86

A.1.1 Msn2 is a key regulator of the stress response in yeast 86

A.1.2 Functional domains of Msn2 88

A.1.3 Gene induction by Msn2 90

A.1.4 Msn4, the paralog of Msn2 94

A.2 Integrating optogenetic stimulation and microscopy 95

A.2.1 Introduction 95

A.2.2 Refinements to the optoPlate to facilitate microscopy 95

A.2.3 Control of high-throughput microscopy 95

A.2.4 Segmentation and measurement of yeast from microscopy images 96

A.2.5 Integrating optogenetic control, microscopy, and image analysis 98

A.3 A custom pipeline for high-throughput analysis of flow cytometry data 99

A.4 LOV actually: controlling Msn2 with LINUS 100

A.5 List of strains used in light sweep experiments 101

A.6 Quantifying yeast colony growth from images of plates 110

A.7 Biological signal generators 113

A.7.1 Abstract 113

A.7.2 Introduction 113

A.7.3 Components of a biological signal generator 114

A.7.4 The importance of biological signal generators 116

A.7.5 Synthetic biology tools for biological signal generators 117

A.7.6 *In silico* controllers for biological signal generators 119

A.7.7 Insights gained from biological signal generators 121

A.7.8 Conclusions and Perspectives 124

A.7.9 Glossary 125

References 127

Chapter 1: Thesis overview

1.1 Introduction

Cells survive changes in their environment by regulating the expression of their genes. To achieve this, cells control the activity of transcription factors (TFs) by, among other things, regulating their nuclear localization or ability to bind DNA. In fact, environmental information may be encoded in the temporal dynamics of TF nuclear localization and subsequently decoded by promoters to enact stimulus-specific gene expression responses [1]. Some TFs, like p53 and NF-κB, exhibit stimulus-specific nuclear localization dynamics and are subject to post-translational modifications that regulate their ability to bind DNA [2]–[5], but it was unclear how changing the ability of a TF to bind DNA would affect how promoters decode its localization dynamics.

In this thesis, we use the yeast general stress response TF Msn2 as a model system to further investigate promoter decoding of TF localization dynamics and examine how decoding is affected by changes in the ability of a TF to bind DNA. Previous studies investigated the relationship between Msn2 localization dynamics and downstream gene expression by modulating the activity of protein kinase A (PKA), an upstream regulator of Msn2 [6]–[9]. These studies found that Msn2 target genes decode Msn2 localization dynamics by exhibiting differential responses to the amplitude, duration, and frequency of Msn2 nuclear localization. However, PKA has other targets that affect gene expression [10]–[12]. To avoid their influence, we use an optogenetic system to directly control the nuclear localization of Msn2 with light.

Such optogenetic experiments require the reliable delivery of precise light doses to cells under study, yet most light arrays used for optogenetic stimulation use inexpensive, off-the-shelf LEDs whose brightnesses vary considerably. Therefore, in Chapters 3 and 4 we describe tools and methods we developed for calibrating two light delivery systems—the light plate apparatus and optoPlate—and demonstrate the ability to consistently deliver precise, targeted light doses. These tools, and others highlighted in the Appendix, enabled the experiments of Chapter 5, where we systematically dissect how promoters decode Msn2 nuclear localization dynamics and how decoding is affected by changes in the ability of Msn2 to bind DNA.

1.2 Key findings

In Section 5.3.1, we create a light-controlled Msn2 mutant and demonstrate the ability to precisely control its nuclear localization dynamics with light. In Section 5.3.2, we use that optogenetic tool to measure the response of Msn2 target genes to defined patterns of Msn2 nuclear localization generated with time-varying light doses. This reveals that the signal decoding behavior of Msn2 target promoters previously reported in response to PKA modulation persists when Msn2 localization is controlled directly with light. Then, in Section 5.3.3, we use a mathematical model of gene expression to identify high sensitivity promoters, which are readily induced by nuclear Msn2, and low sensitivity promoters, which filter out low amplitude, short duration, and pulsatile doses of nuclear Msn2.

In Section 5.3.4, we present evidence that the nuclear localization of Msn2 triggers its degradation, which begins about 14 min after Msn2 first enters the nucleus and may cause the expression of low sensitivity promoters to plateau for doses of nuclear Msn2 longer than 30 min, as discussed in Section 5.3.5.

In Sections 5.3.5 – 5.3.7, we create high and low affinity light-controlled Msn2 mutants and use them to verify model predictions that changes in the ability of Msn2 to bind DNA have a stronger effect on the expression of low sensitivity promoters than high sensitivity promoters. In general, we find that increasing the ability of Msn2 to bind DNA increases the expression of its target genes, making them less noisy and more responsive to shorter, weaker, and pulsatile doses of nuclear Msn2. We also find that increasing the ability of a promoter to bind Msn2 by adding extra binding sites has broadly similar effects, but that the relative ability to respond to pulsed versus continuous doses of nuclear Msn2 is largely set by the promoter.

In Section 5.3.8, we perform a sensitivity analysis of our gene expression model to identify properties of a promoter that may cause it to exhibit divergent responses to Msn2 mutants with different DNA binding abilities. We find that a low sensitivity to Msn2, slow activation kinetics, or fast deactivation kinetics can cause a promoter to exhibit divergent responses to Msn2 mutants with different DNA binding abilities. We also find that low amplitude doses of nuclear localization have a similar effect.

Lastly, in Section 5.3.9, we measure the ability of our Msn2 affinity mutants to activate target genes in response to natural stresses—without optogenetic control—and find that changing the ability of Msn2 to bind DNA can disrupt the ability of its target promoters to discriminate between glucose starvation and hyperosmotic shock.

Chapter 2: Background

2.1 Encoding cellular information in transcription factor dynamics

Cells survive changes in their environment by regulating the expression of their genes: environmental information is passed through signaling pathways to transcription factors (TFs), which initiate a gene expression response. Signaling pathways often exhibit a bowtie topology where multiple signals converge on a single TF (Figure 2.1) [13]. In these cases, how does the TF activate the appropriate set of genes needed for a stimulus-specific response? It has been proposed that cells can overcome this challenge by encoding environmental information in the temporal dynamics of TF activity. Just as Morse code enables a simple on-off switch to communicate virtually any message, these regulatory mechanisms enable a single TF to coordinate multiple gene expression programs, allowing cellular signaling pathways to convey an expanded range of information using a limited set of components. A well-studied example of this is Crz1, which coordinates the cellular response to calcium in *Saccharomyces cerevisiae*. Extracellular calcium causes Crz1 to translocate to the nucleus in one of two modes, continuous or pulsatile, and recent work has shown that Crz1 target genes can decode its localization dynamics by preferentially activating in response to one mode over the other [14], [15]. In the pulsatile mode, the timing of Crz1 pulses varies between cells, but their overall frequency is proportional to the concentration of extracellular calcium. This frequency modulation of nuclear localization allows the proportional regulation of Crz1 target genes, despite differences in their expression strength or sensitivity to nuclear Crz1 [15].

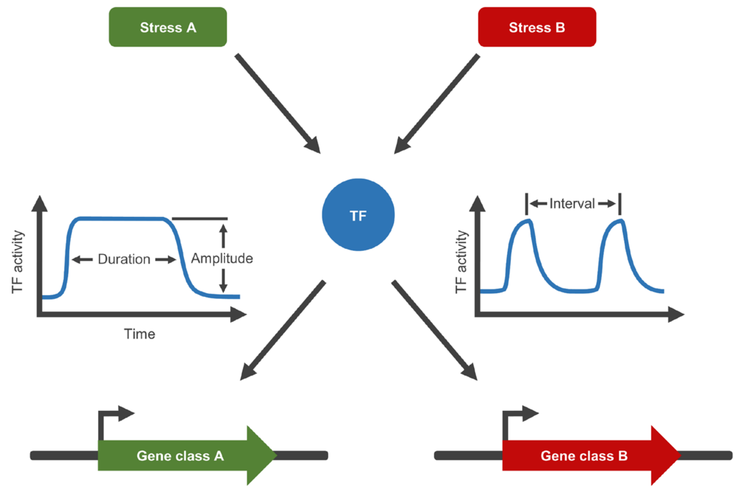

Figure 2.1 Encoding cellular information in TF activity dynamics. A cartoon example showing how environmental information may be encoded in the temporal dynamics of TF activity and subsequently decoded by gene promoters to enact stimulus-specific gene expression programs. Here, two stresses activate the same TF, but with different dynamics such that stress A preferentially activates gene class A and stress B preferentially activates gene class B.

A prime example of the bowtie topology is the yeast general stress response TF Msn2, a C2H2 zinc finger protein (the largest structural class of TF in eukaryotes) that regulates over 200 genes. As detailed in Section A.1, multiple signaling pathways (PKA, TOR, SNF) converge on Msn2, which in turn plays a key role in the environmental stress response (ESR) [16], [17]. Under normal growth conditions, residues of the nuclear localization signal (NLS) and nuclear export signal (NES) of Msn2 are phosphorylated by protein kinase A (PKA) to sequester Msn2 to the cytoplasm, but in response to environmental stress, these residues are dephosphorylated and Msn2 translocates to the nucleus where it regulates its target genes by binding stress response elements (STREs) in their promoters [18]. Information describing the environmental stresses is encoded in the nuclear localization dynamics of Msn2: hyperosmotic shock causes an early, continuous pulse of Msn2 nuclear localization whose duration is dose-dependent, while glucose starvation causes a similar early pulse that’s followed by short, sporadic bursts of nuclear localization whose frequency is dose-dependent [6]. These stresses elicit distinct transcriptional responses and previous work using chemical inhibition of PKA showed that Msn2 target genes decode Msn2 dynamics by exhibiting differential responses to the amplitude, duration, and frequency of Msn2 nuclear localization [7], [8], [17].

At least 10 yeast TFs and a variety of mammalian TFs exhibit similar pulsatile dynamics [19]–[22]. The mammalian TF NF-κB, which is involved in the inflammatory response, pulses in and out of the nucleus in response to tumor necrosis factor-α (TNFα), but undergoes sustained nuclear localization in response to bacterial lipopolysaccharides (LPS) [2]. How immune response genes decode these temporal dynamics to enact stimulus-specific gene expression programs remains an active area of research, though NF-κB target genes have been shown to exhibit differential responses to the amplitude (both absolute and fold-change) and duration of nuclear NF-κB [20], [23], [24]. Both continuous and pulsatile doses of nuclear NF-κB can activate gene expression in mouse macrophages, but only continuous nuclear localization of NF-κB causes epigenetic reprogramming by sustained disruption of histone-DNA interactions [25].

Similarly, gamma irradiation causes double-stranded DNA breaks and short, fixed amplitude pulses of the tumor suppressor p53 whose frequency increases with the gamma radiation dose [26]. In contrast, UV irradiation causes DNA lesions and a single, sustained pulse of p53 whose amplitude and duration is proportional to the UV radiation dose [22]. When controlled using a drug, these different patterns of p53 activity lead to different patterns of gene expression and different outcomes: cells with pulsatile dose of p53 activity tend to recover, while cells with sustained p53 activity frequently activate terminal genes, leading to apoptosis or senescence [4]. Two p53 targets (CDKN1A and MDM2) have been shown to exhibit distinct responses to the amplitude, duration, and frequency of p53 activity: CDKN1A is best activated by high amplitude, low frequency pulses of p53 activity, while MDM2 is readily activated by low amplitude pulses of p53 and is most strongly induced when p53 is pulsed at its natural frequency [27]. Recently, differences in p53 dynamics between tissues have been linked with differences in radiation sensitivity [28].

2.2 Studying TF localization dynamics

To study how cells decode TF activity dynamics, one must at minimum be able to generate different patterns of TF activity and measure the downstream response (Figure 2.2). Perhaps the simplest way to do this is to subject cells to environmental stimuli and measure the resulting changes in TF activity and gene expression [2], [4], [6], [15], [29]–[32]. While such stimuli represent physiologically-relevant conditions, this approach presents two challenges. First, due to the stochastic nature of intracellular signaling networks, TF activity dynamics generated by environmental stimuli vary substantially between cells [20], [28], [33]. Second, environmental stimuli often activate other factors, making it difficult to isolate the contribution of TF dynamics to changes in gene expression. This occurs for Msn2, which as regulator of the yeast environmental stress response is activated by a range of stresses including heat shock, glucose starvation, and hyperosmotic shock and is subject to complex upstream regulation that also controls the activity of other, stress-specific factors such as Hog1 or Mig1 (see Section A.1.1) [17], [34].

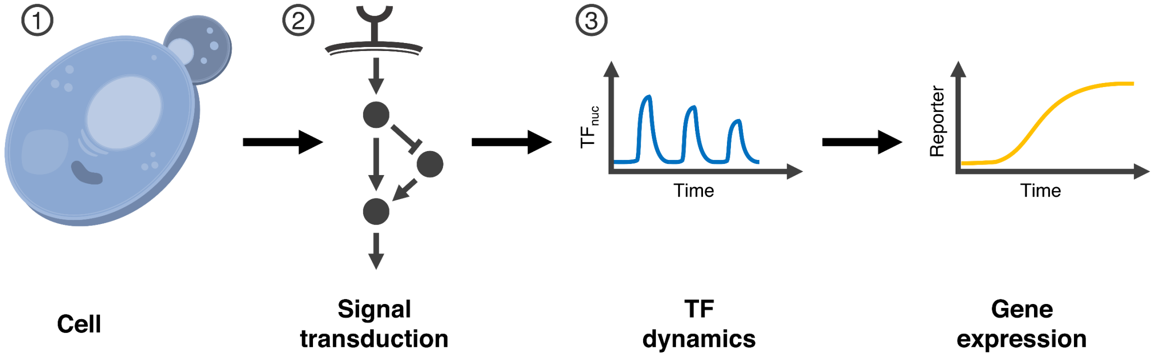

Figure 2.2 Studying TF dynamics. To study promoter decoding of TF dynamics, one must generate different patterns of TF activity and measure the resulting gene expression response. This may be achieved by 1) applying a cell-wide stress known to activate the TF, 2) perturbing the activity of signaling component upstream of the TF such as a kinase, or 3) directly perturbing the activity of the TF itself.

A more precise approach for investigating TF activity dynamics is to perturb the activity of an upstream regulator of the TF under study. The relationship between Msn2 nuclear localization dynamics and downstream gene expression was studied using an analog sensitive allele of PKA whose activity is inhibited by the small molecule 1-NM-PP1 [6]–[9], [35]. In these studies, defined patterns of Msn2 nuclear localization were generated by time-varying doses of 1-NM-PP1 delivered by a microfluidic device and the resulting changes in gene expression were measured. A similar microfluidic approach was used to generate controlled doses of p53 activity with time-varying doses of the drug Nutlin-3, which inhibits p53 degradation [27]. However, small molecules capable of modulating the activity of an upstream regulator, if they exist, are often expensive and the microfluidic devices used to deliver them are generally low-throughput. Moreover, modulating the activity of an upstream regulator can have unexpected effects if that regulator has multiple targets that affect gene expression. For example, other proteins downstream of PKA include the TFs Hsf1, Sok2, and Dot6 and components of the mediator complex [10]–[12].

Developments in optogenetics have made it possible to directly control the subcellular localization of proteins with light [36]. Many of these approaches exploit the *Avena sativa* LOV2 domain, which features a Jα tail that unwinds when excited by blue light to expose an effector epitope: optogenetic systems such as LINUS and LANS feature an NLS epitope for light-induced nuclear import, while LEXY features an NES epitope for light-induced nuclear export [37]–[39]. One drawback of these LOV2-based systems is “leakiness”, the occasional unfolding of the Jα tail in the dark, which causes unwanted nuclear translocation events. To reduce leakiness, Chen *et al* recently developed CLASP (controllable light-activated shuttling and plasma membrane sequestration)—which pairs a LOV2-based light-activated NLS with a Zdk1 domain that preferentially binds a plasma membrane anchor in the dark—and used it to explore how yeast calcium response genes differentially interpret continuous versus pulsatile doses of Crz1 nuclear localization [14].

2.3 Other cellular mechanisms for regulating TF activity

Studies relating TF activity dynamics to downstream gene expression have typically focused on nuclear localization dynamics, which can be easily measured by tagging TFs with fluorescent proteins. However, cells control TF activity in myriad other ways, such as regulating their ability to recruit transcriptional machinery or bind DNA via post-translational modifications (PTMs) like acetylation [40]–[42] or phosphorylation [43]–[45]. In fact, NF-κB exhibits pulsatile nuclear localization dynamics and is subject to PTMs that control its ability to bind DNA [46]–[50]. Moreover, its five subunits can dimerize in almost any combination with varying, but overlapping affinities for different NF-κB binding sites. Similarly, various PTMs modulate the ability of p53 to bind DNA and the activation of low sensitivity terminal cell fate genes may involve both sustained nuclear p53 and the acetylation of its DBD [4], [22], [42], [51]–[53]. On the other hand, there is no strong evidence that the DNA binding affinity of Msn2 is regulated by PTMs, though previous studies have identified mutations to its DBD that increase or decrease its ability to bind DNA [54], [55]. This makes Msn2 an excellent model system for investigating the interplay of TF localization dynamics and DNA binding affinity in gene induction, especially because Msn2 naturally exhibits pulsatile localization dynamics and regulates hundreds of genes in its role as general stress response TF (as detailed in Section A.1).

Chapter 3: Calibrating and standardizing a light plate apparatus

3.1 Introduction

Optogenetic systems provide a promising toolkit for cell biology. These systems utilize genetically-encoded light-sensitive proteins to actuate processes within the cell. The optogenetic toolkit is improving and expanding; genetically-encoded light sensitive proteins have been developed to control cellular events such as gene expression, protein localization, and phase separation [56]–[58]. Because the response of these proteins is light dose-dependent and excessive light is harmful to cells, it is important to administer precise, quantifiable, and reproducible light doses during optogenetic experiments. Until recently, the hardware necessary to do this has made the use of optogenetic tools difficult for non-specialist research groups.

The Light Plate Apparatus (LPA) is a recently-developed, flexible, and user-friendly hardware platform that promises to improve the accessibility of optogenetic technology [59]. The LPA is an open source programmable LED array that delivers controlled light doses to each well of a 24-well plate. The LPA has two LEDs (top and bottom) for each well and consists of a printed circuit board, a microcontroller, three LED drivers, and other commercially available electronic components that can be ordered and assembled within a 3D-printed enclosure. The LPA is programmed using an open-source web-based tool called Iris [60], making sophisticated illumination patterns accessible to researchers without engineering or programming experience.

A newly assembled LPA will exhibit unwanted brightness differences between wells due to differences in LED performance. It is therefore necessary to calibrate the LPA before use so that each LED outputs the correct light intensity. The current applied to each LED can be adjusted independently by scaling a dot correction (dc) value, which ranges from 0 to 63. Finer adjustments to brightness can be made by pulse width modulation of the current by scaling a grayscale value (gcal), which ranges from 0 to 255 [61]. The dc and gcal calibration values per LED are stored as space-delimited integers in the files “dc.txt” and “gcal.txt”, which can be manually loaded onto the LPA via an SD card. Once calibrated, a user can set the LPA to administer timed light doses for each LED using the Iris webtool, which outputs “Iris” values that control the intensity of each LED. The Iris values further scale the current to each LED, such that it is ultimately pulse width modulated by:

$$(Iris\ x\ gcal)/255$$

With dc, gcal, and Iris set to their maximum values a current of 17.8 mA can be supplied to each LED in the array simultaneously. On a calibrated LPA, two LEDs assigned the same Iris value should output the same light dose. These Iris values (and other light program properties) are saved to the file “program.lpf” (which is loaded onto the LPA via the SD card) and range between 0 (no LED output) and 4095 (100% LED output).

The published LPA documentation included two methods for calibrating an LPA. Both methods generally involve tuning the dc and gcal values such that the brightest LEDs are dimmed to match the brightness of the dimmest LEDs. In the first method, a MATLAB script is used to calculate tuned gcal values based on relative LED intensity measurements extracted from digital photos of the LPA. In the second approach, each LED is manually measured with a probe spectrometer and the gcal value for each LED is scaled to produce a desired intensity reading. Both methods produce more uniform LED output after successive rounds of calibration.

We have developed a third method for calibrating the LEDs based on absolute irradiance measurements acquired using a standard photodiode optical power sensor. A power meter with an optical power sensor represents the minimal equipment for any lab interested in performing quantitative optogenetic experiments. A 3D-printed adapter that interfaces with the 24-well plate and appropriate MATLAB code allow a single user to quickly measure absolute irradiance per well and perform subsequent calibration. We extend our methodology to calculate a standard curve for each LPA, allowing Iris values to be chosen such that a desired irradiance can be attained per well. This allows us to utilize multiple LPAs simultaneously to administer equivalent light doses, increasing experimental throughput. Supplementary materials including custom hardware, software, and step-by-step protocols are available online [62].

3.2 Calibrating an LPA

In our protocol (Figure 3.1A), the user measures the irradiance of each well of the LPA in order, generating an irradiance signal which resembles a series of 24 repeated square waves (Figure 3.1B). A MATLAB script (LPA_calibration.m) then identifies the wells from the signal, measures the mean irradiance value per well, and calculates the calibration values needed for uniform LED output across the LPA (Figure 3.1C).

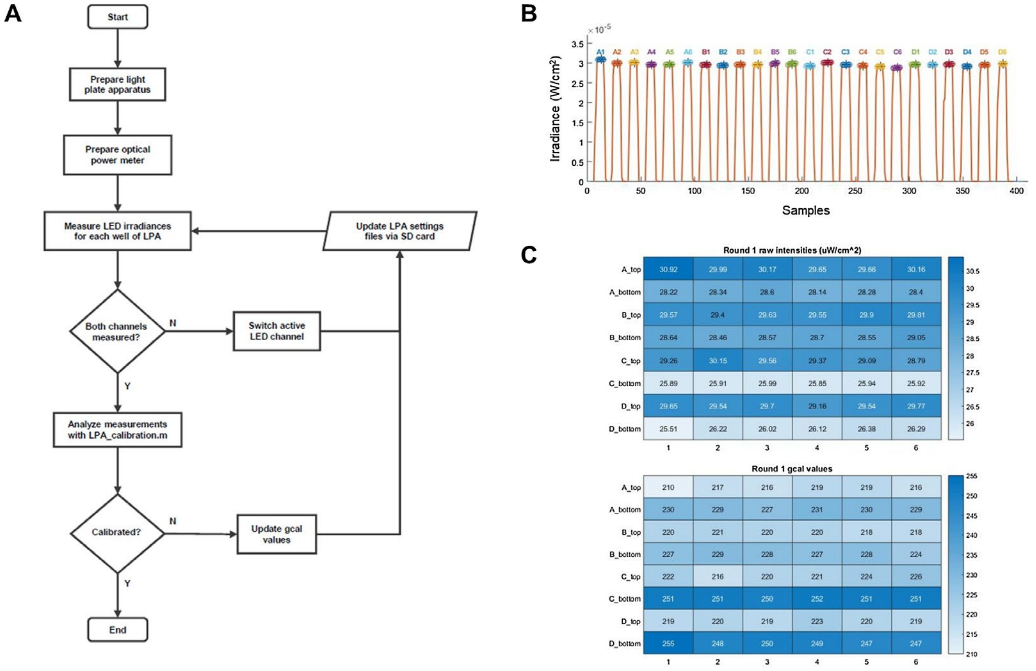

Round 1 raw intensities (uW/cm^2)

	1	2	3	4	5	6
A_top	30.92	29.99	30.17	29.65	29.66	30.16
A_bottom	28.22	28.34	28.6	28.14	28.28	28.4
B_top	29.57	29.4	29.63	29.55	29.9	29.81
B_bottom	28.64	28.46	28.57	28.7	28.55	29.05
C_top	29.26	30.15	29.56	29.37	29.09	28.79
C_bottom	25.89	25.91	25.99	25.85	25.94	25.92
D_top	29.65	29.54	29.7	29.16	29.54	29.77
D_bottom	25.51	26.22	26.02	26.12	26.38	26.29

Round 1 gcal values

	1	2	3	4	5	6
A_top	210	217	216	219	219	216
A_bottom	230	229	227	231	230	229
B_top	220	221	220	220	218	218
B_bottom	227	229	228	227	228	224
C_top	222	216	220	221	224	226
C_bottom	251	251	250	252	251	251
D_top	219	220	219	223	220	219
D_bottom	255	248	250	249	247	247

Figure 3.1 LPA calibration process. Calibration process for an LPA fitted with two blue LEDs per well. (**A**) A flow chart detailing the steps of the calibration process. (**B**) Representative image of well irradiance measurements acquired in series as identified by “LPA_calibration.m”. Well identifiers (e.g. “A1”) are

indicated. Each well was covered by on average 5 samples. We sampled at a rate of 1 Hz so there is 1 second between each sample. The entire plate was measured in less than 400 s. (**C**) Representative well irradiance measurements and tuned gcal values per LED as calculated by “LPA_calibration.m”.

3.3 Standard curve procedure

Once calibrated, the LPA delivers a uniform light dose across all the wells of the LPA. At this stage, it is useful to generate an equation relating the Iris values set when designing a light program to the light output of each well. This allows a user to predict the Iris values necessary to achieve a desired light dose and enables higher-throughput experiments by allowing multiple LPAs to deliver equivalent light doses. In general, this is done by measuring the light output of the LPA at a given light dose and solving for the equation relating light dose to Iris value. This can be done with measurements made at a single Iris value, though here we do this over a wide range of Iris values to demonstrate that our script can accept measurements made over an arbitrary number of Iris values in order to make accurate predictions and to show that the relationship between Iris and light dose is linear.

3.4 Method Validation

To confirm that our LPA calibration process leads to the convergence of LED irradiances across the LPA, we tracked the irradiance of each LED as we performed three successive rounds of calibration with a fixed Iris value of 2000 on a representative LPA (Figure 3.2). Before the first round of calibration, the mean irradiance of all LEDs was 109.6 μW/cm^2 with a coefficient of variation of 12.6%. After the third round of calibration, the brightest LEDs were dimmed to match the irradiance of the dimmest LED, such that the mean irradiance of all LEDs was 83.5 μW/cm^2 with a coefficient of variation (CV) of 0.82%. We consider LPAs with a CV lower than 1% to be calibrated.

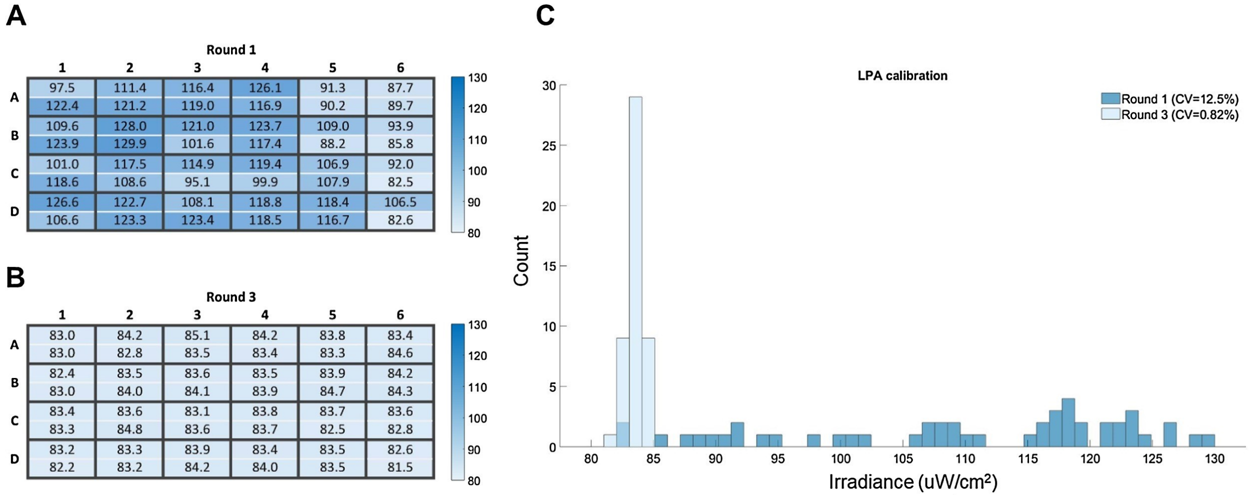

Round 1

	1	2	3	4	5	6
A	97.5	111.4	116.4	126.1	91.3	87.7
	122.4	121.2	119.0	116.9	90.2	89.7
B	109.6	128.0	121.0	123.7	109.0	93.9
	123.9	129.9	101.6	117.4	88.2	85.8
C	101.0	117.5	114.9	119.4	106.9	92.0
	118.6	108.6	95.1	99.9	107.9	82.5
D	126.6	122.7	108.1	118.8	118.4	106.5
	106.6	123.3	123.4	118.5	116.7	82.6

Round 3

	1	2	3	4	5	6
A	83.0	84.2	85.1	84.2	83.8	83.4
	83.0	82.8	83.5	83.4	83.3	84.6
B	82.4	83.5	83.6	83.5	83.9	84.2
	83.0	84.0	84.1	83.9	84.7	84.3
C	83.4	83.6	83.1	83.8	83.7	83.6
	83.3	84.8	83.6	83.7	82.5	82.8
D	83.2	83.3	83.9	83.4	83.5	82.6
	82.2	83.2	84.2	84.0	83.5	81.5

Figure 3.2 Results of LPA calibration. (**A**) Heatmap of the irradiance measurements for each LED prior to round one of calibration showing the uneven distributions of LED irradiances in an uncalibrated LPA. The CV of the LED irradiances is 12.5% before calibration. Each well has two blue LEDs. (**B**) Heatmap of the irradiance measurements for each LED on the same LPA after three rounds of calibration. The CV of the LED irradiances is 0.82% after calibration (**C**). Histogram depicting the data represented in the heatmaps of this figure. The values across the calibrated LPA have converged to the dimmest LED.

We next generated a standard curve relating Iris value to LED irradiance for the calibrated LPA by measuring the light output of the LPA over a range of Iris values and using the "LPA_standardCurve.m" script as described previously (Figure 3.3A). The script generates an equation for the line that best fits the measurements (blue triangles). The equation takes the form:

$$Intensity \; = \; a \; x \; Iris$$

(where *a* is the fitted parameter) and represents the relationship between Iris value and irradiance and can be used to estimate the Iris value for both the top and bottom LEDs in a given well needed to achieve a specified light dose. We predicted the Iris values needed to achieve irradiances of 25, 50, 100, 200, and 300 μW/cm^2 and measured the light output of the LPA using these predicted Iris values. In all cases, the measured values (blue circles) were within 4% of the target value. The utility of the standard curve is contingent upon having a well-calibrated LPA.

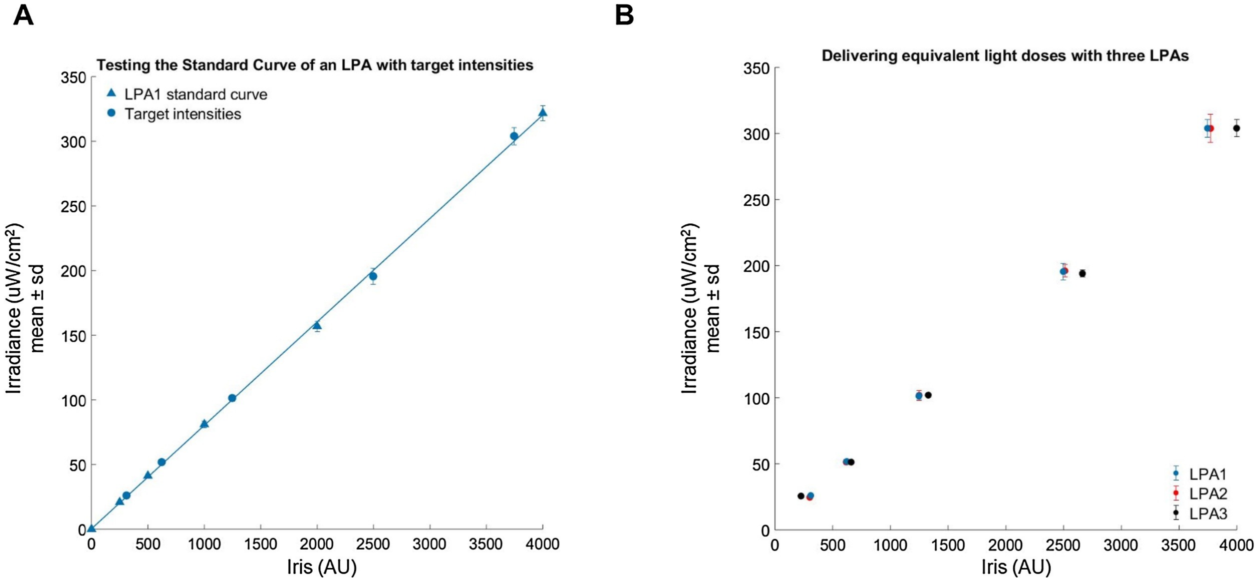

Figure 3.3 LPA standard curve. All plot markers represent the mean and standard deviation of a set of eight measurements. (**A**) A standard curve generated from a set of measurements across the programmable range of Iris values (triangular markers). Predicted Iris values for specific target irradiances were then programmed and the actual irradiance measured (circular markers). (**B**) Target irradiances for three different LPAs are shown (circular markers). The measurements between LPAs at the target irradiances all cluster closely and are within 3% of their respective targets.

One LPA provides 24 wells in which to culture cells and expose them to appropriate light doses. Increasing throughput requires multiple LPAs calibrated such that they can administer the same light doses. By calibrating our LPAs and relating Iris values to light dose using an absolute irradiance measurement, we can easily configure multiple LPAs to produce the same light output (Figure 3.3B). We predicted Iris values needed to produce light outputs of 25, 50, 100, 200, and 300 μW/cm^2 for three LPAs. Though the LPAs had different standard curves, and thus require different Iris values to generate a given light dose, we were able to achieve irradiances within 3% of the targeted irradiance for all LPAs. This enables us to consistently and quantitatively use multiple LPAs simultaneously for higher throughput experiments. To further demonstrate reduced light dose variation following calibration we set all the LEDs of an uncalibrated LPA to a constant Iris value and measured the irradiance of each well. We then calibrated the LPA, and assigned all wells a constant Iris value such that the mean irradiance output by the calibrated LPA approximately matched that of the uncalibrated LPA (Figure 3.4). We did this at three light doses and each time observed significantly reduced irradiance variation.

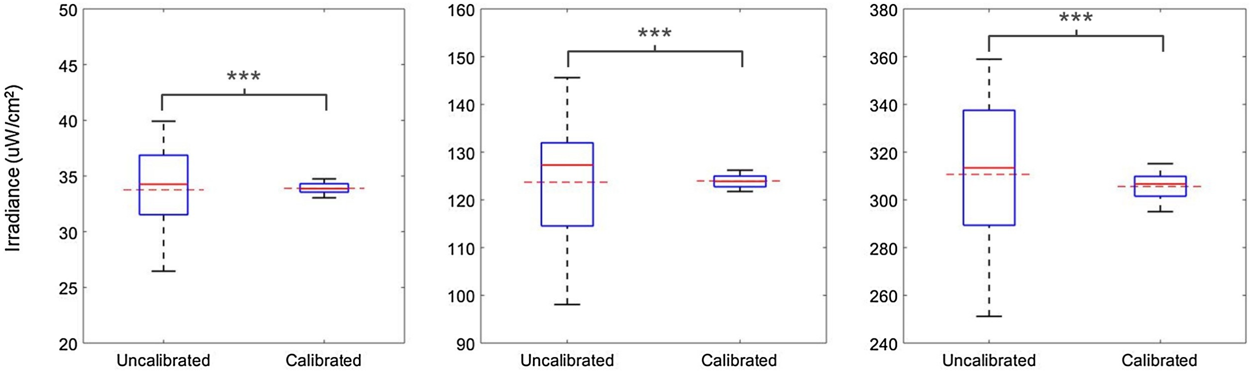

Figure 3.4 Irradiance before and after calibration. We set all the LEDs of an uncalibrated LPA to a constant Iris value and measured the irradiance of each well. We then calibrated the LPA and assigned all wells a constant Iris value such that the mean irradiance output by the calibrated LPA approximately matched that of the uncalibrated LPA and measured the irradiance of each well. We did this at three light doses and each time observed significantly reduced irradiance variability (asterisks indicate $p < 0.001$ as calculated by Levene's test for equality of variances). The dashed red lines depict the average irradiance across the whole LPA for each condition.

To determine how LPA calibration effects an optogenetic system, we measured the light-induced expression of the red fluorescent protein mRuby in the yeast *Saccharomyces cerevisiae.* The expression of mRuby is driven by a CRY2-CIB1 split transcription factor gene induction system [63], [64] that is activated by blue light (470 nm). We aliquoted yeast grown in low fluorescence media [65] to mid-log phase into 24-well plates over a calibrated and uncalibrated LPA mounted in a shaking incubator and set to output a range of blue light doses. The calibrated LPA was configured as described in the *Calibration Procedure* and set to deliver target light doses of 0, 10, 25, 50, 75, and 100 μW/cm^2, in order, to columns 1 – 6 of the 24-well plates (resulting in four replicates per light dose). We assigned the same Iris values to the uncalibrated LPA, which showed more variation in irradiance between wells and consistently exceeded the target light doses (Figure 3.5A). We incubated the yeast at 30 °C under these light conditions for four hours and measured the resulting mRuby expression by flow cytometry (Figure 3.5B). Though biological variability dominates the effect of light dose variability in this case, mRuby expression is consistently higher for the uncalibrated LPA, which is expected due to its higher light doses.

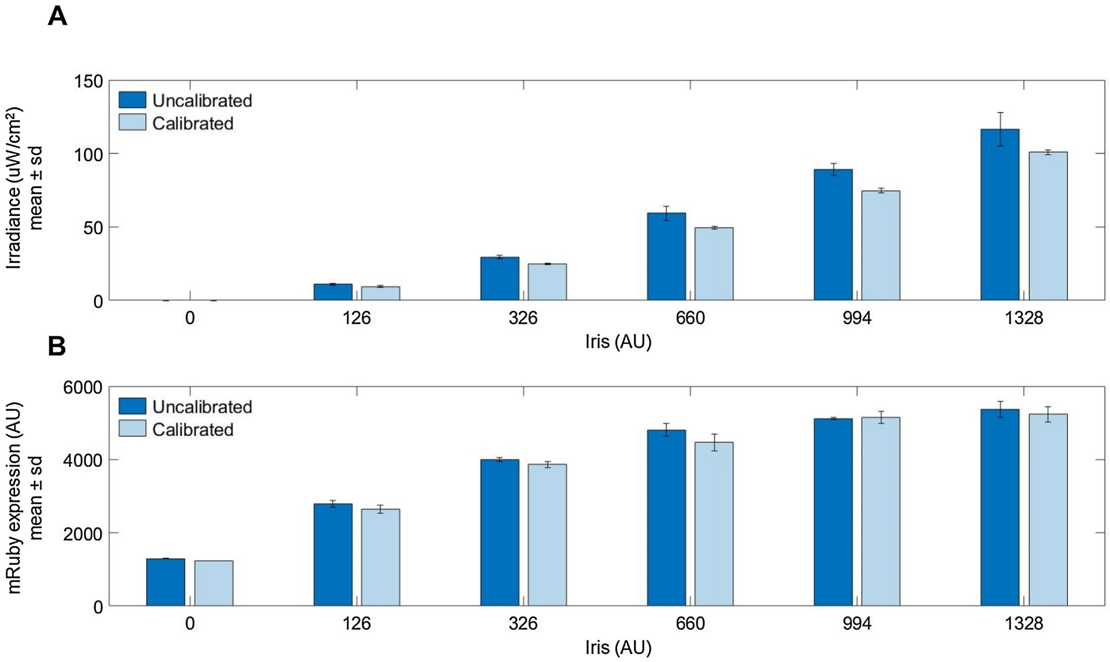

Figure 3.5 Testing LPA calibration with an optogenetic system. Light-induced mRuby expression in yeast grown on a calibrated and uncalibrated LPA set to deliver a range of light doses. Each bar represents the mean of four replicates. The Iris values listed denote the Iris value used for both the top and bottom LED of each well for each plate column. (**A**) Mean irradiance for each column of the uncalibrated and calibrated LPA plates. Irradiance is consistently higher and more variable for the uncalibrated LPA (**B**) Reporter gene expression is consistently higher on the uncalibrated LPA.

3.5 Conclusion

Our method allows the quick calibration of an LPA using an optical power meter and the creation of a standard curve relating light dose to Iris value. Our method makes it easy to administer controlled and consistent light doses across the wells of a single LPA and between multiple LPAs.

Chapter 4: Calibrating and characterizing the light output of an optoPlate

4.1 Introduction

The availability and capability of optogenetic systems—genetically encoded, light sensitive proteins that can control cellular events such as gene expression or protein localization—are ever expanding. It is important to control these optogenetic systems with precise, quantifiable, and reproducible light doses as their response is often light dose dependent and excess light can be harmful to cells. The optoPlate [66], a programmable array of 192 LEDs configured to deliver a custom, time-varying light dose to each well of a 96-well plate, was developed to meet this need. However, without calibration there are substantial brightness differences between LEDs on an optoPlate, even when each LED receives the same electrical current. With all LEDs of an optoPlate receiving a pulse width modulated (PWM) 1.9 mA current at 50% duty cycle, we observed maximum and minimum LED irradiances of 113.7 and 80.1 μW/cm^2, respectively.

This is a known problem with LEDs, the solution to which is to tune the PWM of the current supplied to each LED such that the brightest LEDs are dimmed to match the dimmest LED [59], [67]. This process can involve multiple rounds of brightness measurements and tuning to get right. Here we present a fast method for calibrating an optoPlate in which an optical power sensor is automatically passed over the LEDs in a set order to acquire irradiance measurements from which we calculate a tuning value per LED. We use a programmable microscope stage to automatically move the optical power sensor, though this method could be implemented using other devices whose movement can be programmed, such as a 3D printer. We assembled the optoPlate as described by Bugaj and Lim, but replaced its firmware to allow calibration such that the brightness of each LED is controlled by both a calibration value and an input value as follows:

$$LED\ intensity \propto \frac{input\ values}{255} * \frac{calibration\ values}{255}$$

The input value is supplied by a user to control LED brightness over the course of an experiment. The calibration value must be set only once and accounts for brightness differences between LEDs, such that two LEDs set to the same input value will have the same brightness after calibration. Our optoPlate firmware was built with PlatformIO and allows users to design LED light programs and flash them to the optoPlate using MATLAB. Supplementary materials including custom software and hardware components are available online, along with step-by-step protocols and all experimental data presented here [68].

4.2 Automated measurement of optoPlate LEDs

To calibrate an optoPlate, we first mount it and an optical power sensor to a microscope using 3D-printed adaptors (available online). We initially set all optoPlate LEDs to the maximum possible calibration value (255) and the same, constant input value. We first turn the focus knob to move the optical power sensor to a set level close to the mounted optoPlate (we use a z-position of 4000 μm) then use the microscope's programmable stage to automatically move the optical power sensor over each optoPlate LED in a set order (Figure 4.1A) to acquire a timeseries of irradiance measurements from which the brightness of each LED can be determined (Figure 4.1B) and used to calculate calibration values. To ensure that each LED creates a distinct peak in the irradiance signal, we do not measure all 192 LEDs in one pass. Instead, we measure the LEDs over the course of four passes in which we raster the optical power meter across the optoPlate such that every other LED encountered is inactive, leading to an irradiance signal in which measurements of inactive LEDs create clear troughs between measurements of bright LEDs. We achieve this by setting the optoPlate to deliver a checkerboard illumination pattern, such that no two illuminated wells are directly above, below, or beside each other in a given pass. We measure the remaining wells by setting the optoPlate to deliver the inverse checkerboard illumination pattern. Because the optoPlate has two LEDs per well of a 96 well plate, we repeat this process twice, once for the left LED and once for the right LED.

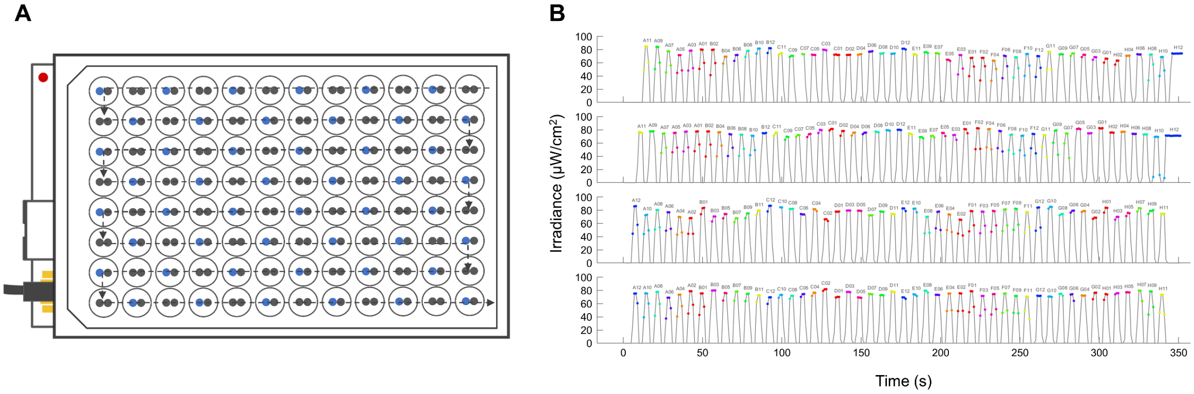

Figure 4.1 Automated measurement of optoPlate LEDs. (**A**) Our optoPlate calibration method involves a measurement process in which an optical power meter is rastered across the optoPlate over a series of four passes in which one LED is active in alternating wells. (**B**) This generates irradiance measurements from which it is easy to identify each LED and measure its brightness.

4.3 Calibrating optoPlate LEDs

Once all optoPlate LEDs are measured, we analyze the irradiance measurements using a MATLAB script that determines the brightness of each LED based on the known order in which they were measured (Figure 4.2) and calculates calibration values such that the brightest LEDs are dimmed to match the dimmest LED. We flash these calibration values to the optoPlate and repeat the whole process until the coefficient of variation of the LED irradiance measurements falls below a set threshold (we use 1%). Because the optoPlate calibration script calculates calibration values using a proportional controller, they are guaranteed to converge to the correct value over successive rounds of calibration. It should be noted that this is how one calibrates an optoPlate with two LEDs of the same color per well. Additional considerations for calibrating an optoPlate with up to three different colored LEDs per well are provided online.

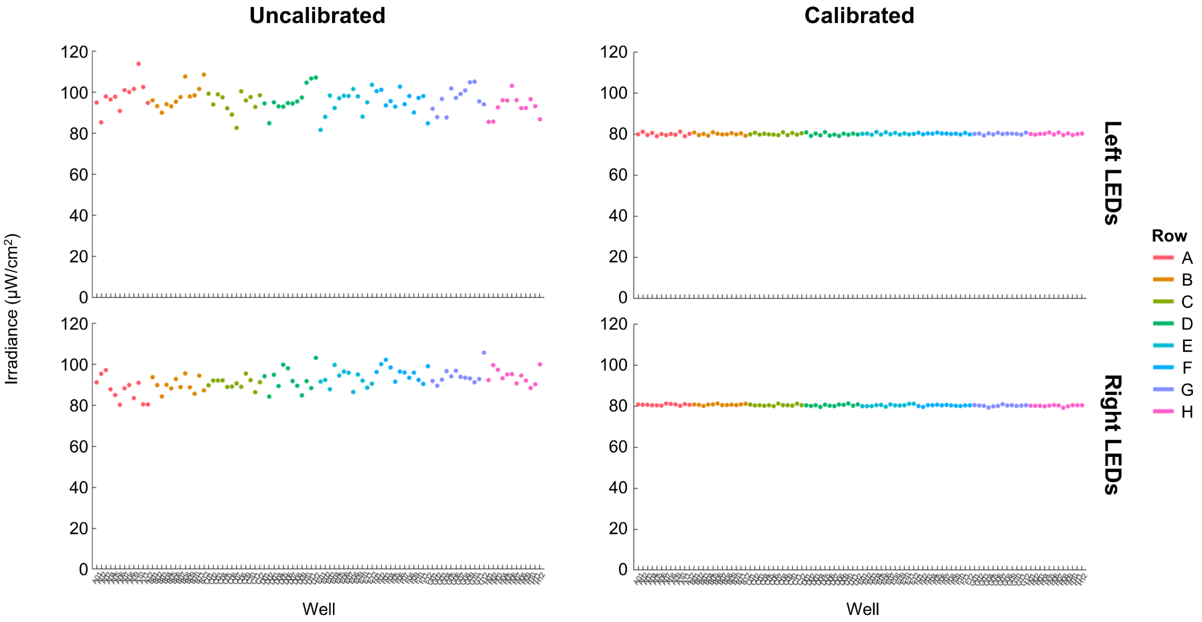

Figure 4.2 Calibrating optoPlate LEDs. Measurements of LED irradiances before and after calibration show that calibration greatly reduces LED brightness variation.

4.4 Validating optoPlate calibration

To demonstrate that it works, we used this method to calibrate one of our lab's optoPlates (Figure 4.3A). Before calibration, the mean irradiance of all LEDs was 94.0 μW/cm^2 with a coefficient of variation (CV) of 6.0%. Notably, the brightest LED was 1.40 times brighter than the dimmest LED. Such a large variation in light dose could easily obscure relevant biological phenotypes in optogenetic experiments [69]. Following just one round of calibration, this variation was substantially reduced: the brightest LEDs were dimmed to match the irradiance of the dimmest LED before calibration (80.1 μW/cm^2), such that the mean irradiance of all LEDs was 80.2 μW/cm^2 with a CV of 0.6%. After calibration, the brightest LED was just 1.01 times brighter than the dimmest LED (Figure 4.3B).

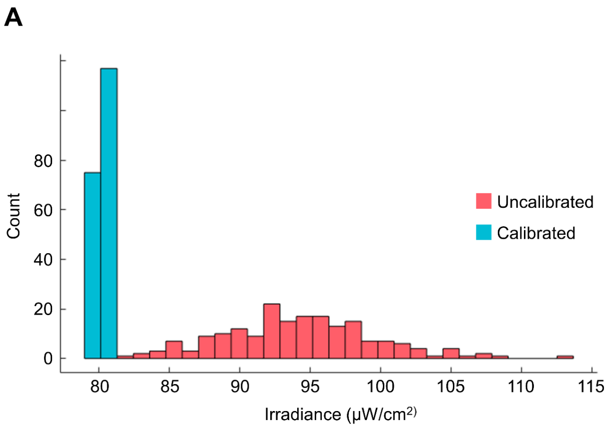

B

	Irradiance (μW/cm^2)				
Condition	**Mean**	**SD**	**Max**	**Min**	**CV (%)**
Uncalibrated	94.0	5.7	113.7	80.1	6.0
Calibrated	80.2	0.5	81.2	79.0	0.6

Figure 4.3 Validating optoPlate calibration. (**A**) A histogram showing that calibration reduces LED variation by dimming the brightest LEDs to match the irradiance of the dimmest LEDs. (**B**) Experimental light doses can vary strongly for an uncalibrated optoPlate; these differences almost disappear following calibration.

4.5 Measuring the optoPlate dose-response relationship

Once an optoPlate is calibrated, it's useful to characterize the dose-response relationship between the input values and irradiance so that it's possible to 1) set experimental light doses per well in absolute units (rather than by input value, which is arbitrary) and 2) consistently achieve equivalent light doses with different optoPlates. This is done by measuring irradiance for a given input value and solving the following linear equation for the slope *m*:

$$Irradiance = m * input\ value$$

While this can be done with a single measurement, to demonstrate that this relationship is reliably linear we set both LEDs of a given well to the same input value and measured well irradiance for input values ranging from 10 to 240 (Figure 4.4A). We acquired these measurements quickly using the automated measurement process described for calibration and then fit these measurements to the linear equation to determine that *m* = 1.59 for our optoPlate.

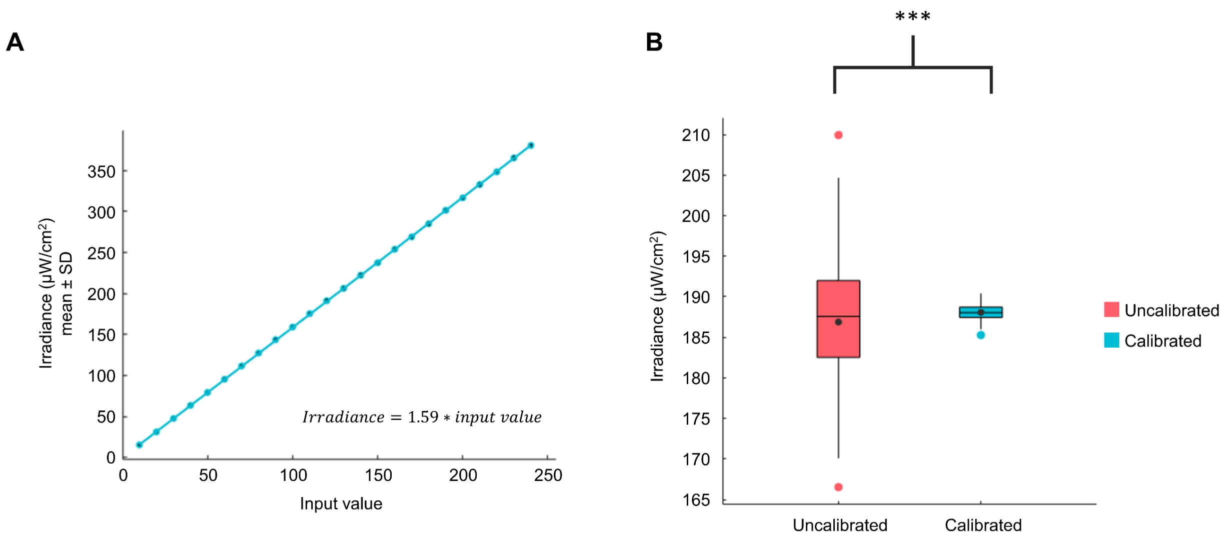

Figure 4.4 Measuring optoPlate dose-response relationship. (**A**) The dose-response relationship between input value and light dose for a calibrated optoPlate. Four measurements were made per input value. Standard deviation of the measured irradiances is small and obscured by the markers. (**B**) Brightness variation for an optoPlate at a fixed brightness level before and after calibration. All optoPlate wells were measured for each condition. Asterisks indicate p<0.001 as calculated by Levene's test for equality of variances.

Knowing the relationship between input value and well irradiance, we next showed that the reduction in LED brightness variation achieved by calibration is not simply an artifact arising from the overall reduction in LED brightness (Figure 4.4B). We set all input values of an uncalibrated optoPlate to 100 and measured the irradiance of each well. We then calibrated the optoPlate and determined that an input value of 118 was necessary to achieve the same mean irradiance as the uncalibrated optoPlate. Measurements acquired before and after calibration show that the mean irradiance per well of the calibrated optoPlate matches that of the uncalibrated optoPlate (with an approximation error of 0.64%), but with significantly reduced variation.

4.6 Conclusion

An uncalibrated optoPlate is potentially a large source of unwanted variation in optogenetic experiments. Manually calibrating all 192 optoPlate LEDs would be laborious. By comparison, our method enables the quick and easy calibration of an optoPlate using standard equipment that most labs performing quantitative optogenetic experiments should have at hand. Because an optical power meter can be set to measure different wavelengths of light, our method can be used to calibrate different colored LEDs. As more instruments for optogenetic stimulation of cells are introduced, the general approach outlined here could be adapted to speedily quantify and calibrate their light output.

Chapter 5: Promoter decoding of TF dynamics and DNA binding

5.1 Introduction

Cells survive changes to their environment by regulating the expression of their genes: environmental information is passed through signaling pathways to transcription factors (TFs), which initiate a gene expression response. Signaling pathways often exhibit a bowtie topology where multiple signals converge on a single TF. In these cases, how does the TF activate the appropriate set of genes needed for a stimulus-specific response? It has been proposed that cells overcome this challenge by encoding environmental information in the dynamics of TF activity. A well-studied example of this is Crz1, which coordinates the response to calcium in *Saccharomyces cerevisiae*. Extracellular calcium causes Crz1 to translocate to the nucleus in one of two modes, continuous or pulsatile, and recent work has shown that Crz1 target genes can decode its localization dynamics by preferentially activating in response to one mode over the other [14], [15]. At least 10 yeast TFs and a variety of mammalian TFs exhibit similar pulsatile dynamics [19]–[22].

However, cells possess a wide variety of mechanisms for controlling TF activity, each offering the opportunity to encode extra information. The mammalian TF NF-κB, which is involved in the inflammation response, pulses in and out of the nucleus in response to tumor necrosis factor-α (TNFα), but undergoes sustained nuclear localization in response to bacterial lipopolysaccharides (LPS) [2]. In murine macrophages, both continuous and pulsatile doses of nuclear NF-κB can activate gene expression, but only continuous nuclear localization of NF-κB causes epigenetic reprogramming by sustained disruption of histone-DNA interactions [25]. Cells also control the activity of NF-κB via post-translational modifications (PTMs) that regulate its ability to bind DNA [46]–[48], [50]. Similarly, gamma irradiation causes short bursts of the tumor suppressor p53 that are sufficient to activate DNA repair genes, while activation of apoptotic genes may involve sustained p53 and PTMs that improve its ability to bind DNA [4], [22], [42], [51]–[53].

A prime example of bowtie topology is the yeast general stress response TF Msn2, a C2H2 zinc finger protein—the largest structural class of TF in eukaryotes—that regulates over 200 genes. Multiple signaling pathways (PKA, TOR, SNF) converge on Msn2, which in turn plays a key role in regulating the cellular response to a variety of environmental stresses [16], [17]. Under normal growth conditions, Msn2 is phosphorylated by protein kinase A (PKA) and resides primarily in the cytoplasm, but in response to environmental stress, Msn2 is dephosphorylated and translocates to the nucleus where it regulates its target genes by binding stress response elements (STREs) in their promoters [18]. Information describing the environmental stresses is encoded in the nuclear localization dynamics of Msn2: hyperosmotic shock causes an early, continuous pulse of Msn2 nuclear localization whose duration is dose-dependent, while glucose starvation causes a similar early pulse that’s followed by short, sporadic bursts of nuclear localization whose frequency is dose-dependent [6]. These stresses elicit distinct transcriptional responses and previous work using chemical inhibition of PKA showed that Msn2 target genes decode Msn2 dynamics by exhibiting differential responses to the amplitude, duration, and frequency of Msn2 nuclear localization [7], [8], [17]. While the graded activation of Msn2 target genes over a range of Msn2 concentrations has been linked to the low affinity of Msn2 for STREs, there is no conclusive evidence that the DNA binding ability of Msn2 itself is regulated via PTMs [54].

We therefore used Msn2 as a model system to investigate the interplay of TF localization dynamics and binding affinity in gene induction. Combining high-throughput microscopy and optogenetic control of Msn2, we probed the relationship between Msn2 nuclear localization dynamics and the expression of its target genes, which exhibited a range of signal decoding behaviors. Computational modeling suggested that these decoding behaviors were related to the affinity between the promoters and Msn2 and that the effect of changes to the DNA binding affinity of Msn2 would be highly promoter dependent. We therefore constructed high and low affinity light controlled Msn2 mutants and performed additional experiments to explore how such changes affected promoter decoding of Msn2 localization dynamics. Increasing Msn2 affinity generally increased the expression of its target genes—making them more response to shorter and weaker doses of nuclear Msn2—and decreased expression noise. These effects were highly promoter dependent and most strongly affected genes with a low affinity to Msn2.

5.2 Methods

5.2.1 Strain construction

The *Saccharomyces cerevisiae* strains used in this study (see Section A.5) were constructed from a base strain in the S288C background (MAT alpha his3D1 leu2D0 lys2D0 MET15 ura3D0). To identify the nucleus, the nuclear protein Nhp6a was tagged with the infrared fluorescent protein iRFP via URA3 pop-out. Briefly, this entailed tagging the C-terminal of Nhp6a using a caURA3 selective marker that was subsequently “popped out” by counterselection with 5-Fluoroorotic acid (5FOA) and a repair DNA template with homology to the genomic DNA regions immediately upstream and downstream of the caURA3 marker. To avoid interference with the Msn2-CLASP mutants, the native copy of Msn2 and its paralog Msn4 were deleted in the base strain, also by URA3 pop-out.

Reporters strains were then constructed from the base strain. Reporters were selected as follows: HXK1, DCS2, SIP18, SIP18 A4, SIP18 D6, DDR2, TKL2, ALD3, and RTN2 were selected based on previous studies of the relationship between Msn2 nuclear localization and gene expression [7], [8]; CTT1 was selected because it was used to study Msn2(S686A) activity [55]; and HSP12 was selected because it was used to test Msn2-CLASP performance [14]. A no reporter control strain featured GFP expressed under a bacterial promoter (glpT), which is silent in yeast. To create each reporter strain, the region 1000 bp upstream of the open reading frame of each reporter gene was amplified by PCR and inserted by Gibson assembly into an integrating plasmid such that it drove the expression of mCitrine. The reporter plasmids were screened by sequencing and integrated into the LEU2 locus of the base strain as previously described [70].

The Msn2 mutants were made using overlap PCR to mix and match, in a modular fashion, Msn2 domains with phosphomimetic mutations that were generated by PCR or purchased as gBlocks from IDT. The Msn2 mutants were then added by Gibson assembly to a CLASP plasmid without a cargo protein (pLO405), which was generously provided by Lindsey Osimiri and Hana El-Samad. Similarly, an equivalent dCLASP plasmid, lacking Zdk1 and yeLANS, was created for each Msn2 mutant by Gibson assembly. The Msn2-CLASP and Msn2-dCLASP plasmids were screened by sequencing and integrated into the URA3 locus of the reporter strains as previously described [14]. The resulting transformants had inconsistent levels of mScarlet, suggesting that the Msn2-CLASP mutants sometimes integrated more than once, likely because regions of self-homology in the Msn2-CLASP plasmids were undergoing homologous recombination when transformed into yeast. Accordingly, we screened all transformants by flow cytometry for consistent, low mScarlet levels prior to use in the light sweep experiments.

Plasmid construction was done using DH5alpa competent cells. Yeast transformations were done using SC agar plates with appropriate auxotrophic or drug selection. After screening, yeast strains were frozen down and grown out on YPD plates for subsequent use in experiments (see Section A.2.5 for a list of all strains used). For all flow cytometry and microscopy experiments, yeast were grown in LFM [65]. For practical reasons, strain construction was done under room lights, but all strains were incubated and stored in the dark.

5.2.2 Blue light delivery

Blue light stimulation was done using an optoPlate [58] modified and calibrated as described previously [71]. Briefly, custom adaptors were designed in 3DS Max and 3D printed to mount the optoPlate upside-down over a 96 well plate on an inverted fluorescence microscope and the optoPlate software was modified to allow 1) communication with a microscope, 2) programming of the optoPlate with a plate map—an Excel spreadsheet recording the light pattern for each well—and 3) calibration of the LEDs (see Section A.2 for more details). After calibration, the relationship between LED amplitude (0 – 255 AU) and irradiance was quantified (see Figure 4.4).

5.2.3 Light sweep experiments

Overview

In each light sweep experiment, reporter induction was measured for two Msn2-CLASP mutants, each subjected to 14 light programs with blue light pulses spanning a range of amplitudes, durations, and oscillatory patterns (Figure 5.25A). As a control, reporter induction was measured for equivalent Msn2-dCLASP mutants subjected to 50 min of 100% light. As a batch control, HXK1 expression was measured for Msn2*-CLASP subjected to both 50 min 100% light and no light. In total, this entailed imaging 32 wells per light sweep experiment. For a given reporter strain and pair of Msn2-CLASP mutants, three light sweep experiments were performed, one for each of three biological replicates.

Growth conditions

The cultures used for each light sweep experiment were grown over multiple days so that they reached mid-log phase by the morning of each experiment (day 0). On the evening of day -2, single colonies were picked into 100 uL LFM in 96 well plate and grown at 30 C overnight. On the evening of day -1, the resulting saturated cultures were serial diluted 1:7000 into 3 mL LFM and grown at 30 C for 15 hours. By morning of day 0, the diluted cultures reached mid-log phase and were used for one of three rounds of light sweep experiments throughout the day. Cultures for the first round of experiments were used immediately, while those for the second and third rounds were, respectively, diluted back 1:30 into 3 mL LFM and grown at 30 C for 3 – 4 hours or diluted 1:5 into 3 mL LFM and grown for 7 – 8 hours. All day 0 steps were done with 30 C LFM and in dark.

Microscopy

Light sweep experiments were done in optical 96 well plates (CellVis P96-1.5H-N) that were pretreated with concanavalin A (MP Biomedicals) to allow cells to adhere to the plate bottom and immersion oil to facilitate the use of an oil immersion microscope objective. Briefly, 30 uL of 2 mg/mL concanavalin A was added to each well being used, incubated at room temperature for 15 min, and removed, then the bottom of the 96 well plate was coated with immersion oi (Olympus, Type F). Cultures to be imaged were diluted to OD600 = 0.125 – 0.150 in LFM and plated in an optical 96 well plate, which was then loaded onto the stage of an inverted fluorescence microscope (Nikon TiE) that was kept dark and at 30 C by an incubating enclosure. The cells were allowed to settle and adhere to the plate bottom for 15 min, at which point the media was removed, the cells were washed three times with LFM, and fresh LFM was added. The cells were then allowed to equilibrate for at least 10 min, during which time the optoPlate was mounted on top of the 96 well plate, connected to the microscope computer via USB, and configured to deliver the appropriate light dose to each well.

For each light sweep experiment, each culture was imaged every 2.5 min for 160 min using a Nikon TiE inverted microscope equipped with a 60x oil immersion objective, an automated stage, and CCD camera. The microscope was controlled by NIS-Elements and acquired 3 images for each of 32 wells per timepoint: an iRFP image of the nuclear marker (400 ms, Nikon Intensilight lamp with 540/45x 720/60m Cy5.5 filter cube, 1.5x gain, ND8, extended NIR mode), an mScarlet image of the Msn2-CLASP mutant (400 ms, Nikon Intensilight lamp with 560/40x 630/75m mCherry filter, ND8, 1.5x gain), and a YFP image of the mCitrine reporter (75 ms, Nikon Intensilight lamp with 510/20x 545/30m rsYFP filter cube, ND8, 1.5x gain). Focus was maintained using the Nikon Perfect Focus System (PFS). The rsYFP (red-shifted YFP) cube and 75 ms exposure at ND8 were selected to prevent light-induced localization of Msn2-CLASP when imaging. Occasionally, the PFS lost focus due to changes in height over the large plate area being imaged or the optoPlate shifting slightly; in these cases, focus was re-established using custom NIS-Elements scripts. When imaging commenced, NIS-Elements instructed the optoPlate to initiate, allowing the timelapse microscopy and light program to operate in sync. Each light program included a 10 min delay before the blue LEDs were activated, such that basal fluorescence could be measured. This corresponded to the 0 min timepoint. The microscope instructed the optoPlate to turn off the LEDs in each well as it was imaged.

Over the course of the light sweep experiments, more than 2300 .ND2 timelapse images were acquired, one for each of 32 wells per experiment. To automate the handling of this large amount of image data, the strain loaded in each well and the light program to which it was subjected were recorded in a spreadsheet (a “plate map”) that was saved with each set of images. Using custom MATLAB scripts, the plate map was subsequently used to automatically label the ND2 images and the single cell fluorescence measurements extracted from them.

Image analysis

Each light sweep experiment produced 32 .ND2 timelapse images with 65 frames and 3 channels per frame: iRFP, mScarlet, and mCitrine. Because the optoPlate was mounted on top of the optical 96 well plate, we did not acquire images with transmitted light such as phase contrast or DIC images from which to segment cells. Likewise, because the mCitrine and mScarlet signals varied substantially over the course of an experiment—mCitrine was induced and mScarlet moved in and out of the nucleus—we segmented the cells from the iRFP images of the nuclear marker. This was done using custom image processing code written in MATLAB. Images were loaded using the Bio-Formats MATLAB toolbox, a Laplacian-of-Gaussian filter was applied to the iRFP images for blob enhancement, and a region of interest (ROI) representing each nucleus was segmented from the resulting high-contrast images using MATLAB's circle finder. This process largely excluded cells whose nuclei were out of focus. The circles were then enlarged by a factor of two to define a region of interest representing each cell, while the cytoplasm was defined as the region within each cell but outside the nucleus. If highly overlapping cells were identified, the cell with the lower "metric" value from MATLAB's circle finder was removed.

Using the ROIs defined during segmentation, the nuclear, cytoplasmic, and cellular fluorescence of each cell was quantified as the median pixel value of these regions in the raw iRFP, mScarlet, and mCitrine images. The background fluorescence in each channel was measured as the mode pixel value outside all cell ROIs. The resulting single cell measurements were labeled with strain and light program information from the plate map associated with each experiment, as well as time information extracted from the .ND2 metadata. Measurements associated with aberrant frames in each timelapse, for example, due to shutter timing mismatches or temporary loss of focus, were identified as outliers in the plot the median iRFP of all cells versus frame and removed. Fluorescence differences due to long-term fluctuations in the Intensilight lamp intensity were corrected based on weekly lamp irradiance measurements. Photobleach correction was applied to the mCitrine measurements, but not mScarlet as the dynamic Msn2 localization time-courses were not amenable to this approach. The median background mScarlet and mCitrine level per experiment was subtracted from the single cell mScarlet and mCitrine measurements, respectively. Msn2 nuclear localization was quantified as nuclear mScarlet divided by cytoplasmic mScarlet. Basal Msn2 localization, quantified as the median Msn2 localization before the 0 min timepoint, was subtracted from the single cell Msn2 nuclear localization measurements. The Msn2 localization measurements were then normalized to the maximum observed level of nuclear localization.

The Msn2 localization and mCitrine induction time-courses for each combination of Msn2-CLASP mutant and reporter were captured for three biological replicates across three separate experiments. As a result, the precise time at which each frame was captured varied by experiment. This was exacerbated in cases where refocusing was needed and led to issues when averaging fluorescence measurements across the three experiments, especially when a frame for one of the replicates was dropped. To account for these issues, the population level Msn2-CLASP localization and mCitrine induction time-courses per condition were calculated by 1) taking the median localization or fluorescence measurement of all cells per frame, 2) assigning these values to bins representing 2.5 min segments of time, and 3) filling in any missing values by linear interpolation. The mCitrine measurements for each replicate were smoothed using a 5-point moving average filter. Because Msn2(A)*-CLASP, Msn2*-CLASP, and Msn2(T)*-CLASP localize similarly in response to light, the area under curve of Msn2 localization per condition was calculated from the mean localization of all three Msn2 mutants across all experiments. Measurements were plotted using the Gramm data visualization toolbox [72].

5.2.4 Flow cytometry experiments with natural stress

As with the light sweep experiments, stains used for flow cytometry experiments were grown over the course of three days. On the evening of day -2, four colonies of each strain were picked into 100 uL of LFM in a 96 well plate and incubated at 30 C overnight. On the evening of day -1, the resulting saturated cultures were diluted 1:1600 into 200 uL LFM in a new 96 well plate and incubated at 30 C for 14 hours. On the morning of day 0, 20 uL of each culture was aliquoted into 8 plates containing 140 uL 30 C LFM and incubated 4 hours at 30 C. The cultures were pelleted by centrifuging for 5 min at 3200 rpm and then forcefully tipping out the supernatant. The pellets were resuspended in control media (30 C LFM), hyperosmotic shock media (30 C LFM with 0.5, 0,25,0.125, or 0.0625 M NaCl), or glucose deficient media (30 C LFM with 0.5, 0.1, or 0.01% glucose) and grown for 2 hours at 30 C. To arrest translation, 40 uL of 0.5 mg/mL cycloheximide was added to each culture and allowed to incubate at 30 C for 30 min, at which point 20 uL of each arrested culture was added to 140 uL 4 C PBS 0.1% tween in a 384 well plate.

The cells were then measured with an Attune NxT flow cytometer equipped with an autosampler: mScarlet was measured with 561 nm excitation light and a 585/16 nm filter and mCitrine was measured with a 488 nm excitation light and 590/40 nm filter. Rainbow beads were used to ensure day-to-day consistency in intensity measurements. The flow cytometry measurements were processed and analyzed using custom MATLAB scripts (see Section A.3). Measurements were imported from .FCS files using the fca_fcsread loader [73] and automatically labeled from a plate map, an Excel spreadsheet file containing the strain and condition information for each well of the 384 well plate. The measurements were gated to remove debris and doublets and the median fluorescence intensity (MFI) was calculated for mScarlet and mCitrine per well. Measurement were plotted using the Gramm data visualization toolbox [72].

5.2.5 Gene expression model

The gene expression model (Figure 5.6) features three promoter states and represents the production of mature YFP (mYFP) as a function of Msn2 with the following ordinary differential equations:

$$\frac{dP_{unbound}}{dt} = d_1 P_{bound} - \frac{k_1 Msn2(t)^n}{K^n + Msn2(t)^n} P_{unbound}$$

$$\frac{dP_{bound}}{dt} = \frac{k_1 Msn2(t)^n}{K^n + Msn2(t)^n} P_{unbound} + d_2 P_{active} - d_1 P_{bound} - k_2 Msn2(t) P_{bound}$$

$$\frac{dP_{active}}{dt} = k_2 Msn2(t) P_{bound} - d_2 P_{active}$$

$$\frac{dmRNA}{dt} = k_3 P_{active} - d_3 mRNA$$

$$\frac{dYFP}{dt} = k_4 mRNA - d_4 YFP - k_5 YFP$$

$$\frac{dmYFP}{dt} = k_5 YFP - d_4 mYFP$$

Pooled Msn2 localization measurements (Figure 5.9) were interpolated and used as in input to the model, which was fit to the time-resolved localization measurements for each combination of reporter and Msn2 DBD mutant as follows. We solved the model to calculate the predicted expression (mYFP) for each light program for 100,000 parameter sets obtained by Latin hypercube sampling in which the promoter-specific parameters were allowed to vary over the following ranges: k_1, d_1, k_2, and k_3 from 10^{-3} – 10^2, K from 1 – 10^4, n from 0.5 – 4, and d_2 from 10^{-4} – 10^2. Global parameter values $d_4 = 0.08$, $k_4 = 15$, $d_4 = 0.001$, and $k_5 = 0.06$ were taken from the literature [7]. We then ranked the parameter sets by how well they minimized the residual sum of squares error between the predicted and measured expression across all light programs.

5.3 Results

5.3.1 Construction and optimization of a light-controlled Msn2

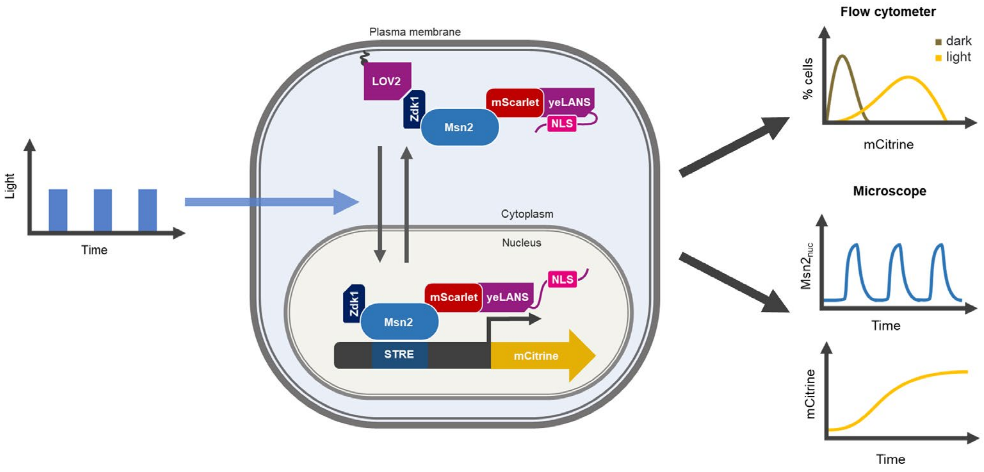

Figure 5.1 Controlling Msn2 localization with CLASP. A schematic of the Msn2-CLASP system and experiments in which time varying light doses drove corresponding patterns of Msn2-CLASP nuclear localization and gene expression that were measured either by flow cytometry or fluorescence microscopy.

To control Msn2 without perturbing its upstream regulators, we used CLASP [14] to directly control the nuclear translocation of Msn2 with light (Figure 5.1). In this optogenetic system, Msn2 is fused at the N-terminus to Zdk1, a peptide that preferentially binds a plasma membrane anchor in the dark, and at the C-terminus to mScarlet and yeLANS, which features a light activated nuclear localization signal (NLS) that is largely inaccessible to the nuclear import machinery in the dark. When excited by blue light, Zdk1 undocks from its plasma membrane anchor and yeLANS undergoes a conformational change that exposes its NLS to the nuclear import machinery, causing Msn2-CLASP to be imported into the nucleus where it can activate target genes. When the blue light is turned off, Msn2-CLASP is rapidly exported from the nucleus due a constitutive nuclear export signal (NES) included within yeLANS. Since strong blue light doses have been reported to induce a stress response in yeast involving Msn2 [74], we also created Msn2-dCLASP (deactivated CLASP) controls lacking Zdk1 and yeLANS to verify that any nuclear localization events were strictly due to optogenetic control. Using fluorescence microscopy, we measured the ability of Msn2-CLASP to localize to the nucleus in response to light and activate a reporter (Figure 5.2A). Msn2-CLASP underwent strong, coherent nuclear localization when excited by blue light and these localization events were rapid and reversible. However, Msn2 can stochastically pulse in and out of the nucleus in the absence of stress [33], which caused it to weakly activate some target genes in the dark, even when tagged with CLASP.

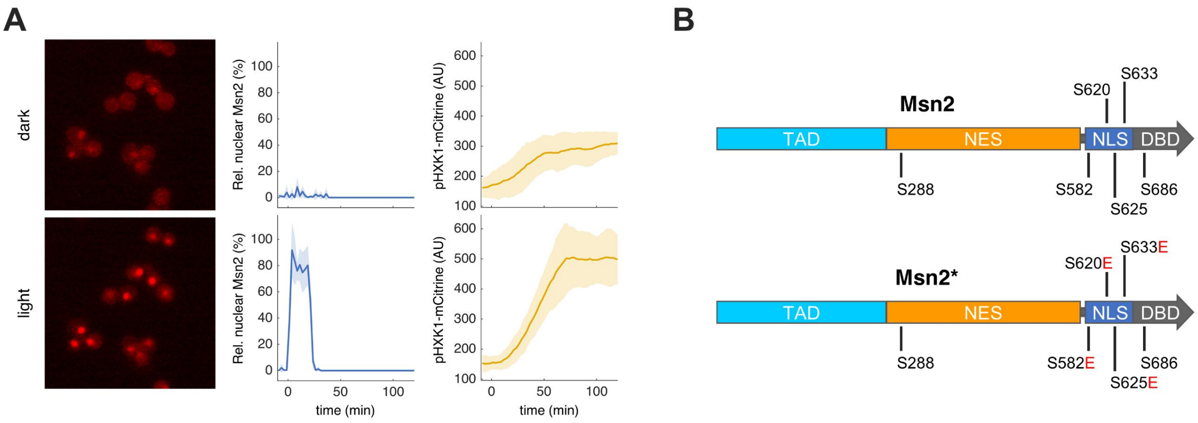

Figure 5.2 Optimizing Msn2 for optogenetic control. (**A**) Fluorescence microscopy images (left panels) showing Msn2-CLASP localizing to the nucleus in response to 255 AU blue light. In the dark, Msn2-CLASP was primarily localized to the cytoplasm, but could stochastically pulse into the nucleus. Msn2-CLASP localization (middle panels) and expression of a pHXK1-mCitrine reporter (right panels) in the dark and in response to a 10 min pulse of 128 AU blue light (indicated by blue shading). Solid lines and shaded regions respectively represent the mean and standard deviation of Msn2-CLASP localization or reporter expression for three biological replicates, each with at least 47 cells. (**B**) Schematic showing relevant functional domains of Msn2—the transactivation domain (TAD), nuclear export signal (NES), nuclear localization signal (NLS), and zinc finger DNA binding domain (DBD)—and residues that were mutated to identify Msn2 mutants more suitable for optogenetic control. Msn2* has a WT TAD, NES, and DBD but features four serine to glutamic acid mutations in its NLS that inhibit stress-regulated nuclear localization.

To disconnect Msn2 from its native localization regulation and identify a mutant more suitable for optogenetic control, we made phosphomimetic mutations to key PKA-regulated phosphosites (Figure 5.2B) in the NLS and NES of Msn2 that control the activity of these domains and thus the ability of Msn2 to move in and out of the nucleus [75]. We mixed the mutated domains in a modular fashion, tagged the resulting Msn2 mutants with CLASP, and screened them for low basal nuclear localization, reduced stochastic pulsing, and the ability to localize to the nucleus and activate target genes in light (Figure 5.3). Based on the screen, we selected for further study a mutant (Msn2*) with four inhibitory serine to glutamic acid mutations in its NLS domain.

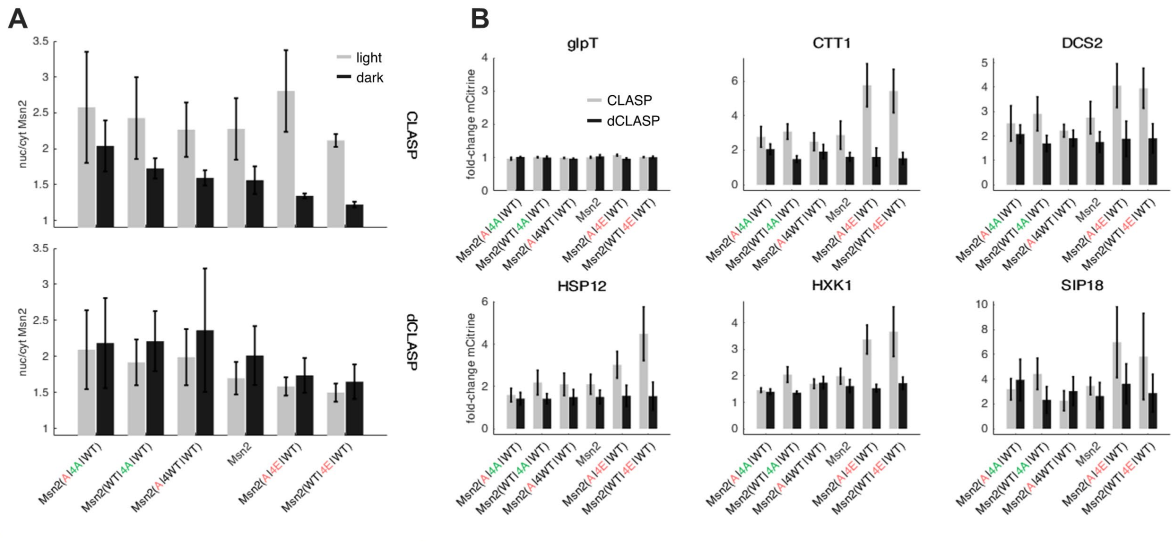

Figure 5.3 Screening Msn2 mutants. (**A**) Msn2 mutants were screened by their ability to localize in response to light. Using an optoPlate mounted on an inverted fluorescence microscope, cells were exposed to at least 5 min of 128 AU blue light and imaged. Bars and error bars represent mean and standard deviation nuclear/cytoplasmic Msn2 for two biological replicates. Msn2 mutants are named following the convention Msn2(NES|NLS|DBD) in which the residues highlighted in Figure 5.2B are mutated to either alanine (A) or glutamic acid (E) or left as WT. Mutations are color-coded red if they inhibit their respective domains. For example, Msn2(A|4E|WT) denotes a mutant with an inhibitory S288A mutation in its NES, inhibitory S582E, S620E, S625E, and S633E mutations (4E) in the NLS and a WT DBD. Msn2(WT|4E|WT) was selected from the screen and renamed Msn2* for convenience. (**B**) Screening Msn2-CLASP mutants by their ability to induce fluorescent reporters expressed under Msn2 target promoters. Reporter strains with Msn2-CLASP or Msn2-dCLASP mutants were exposed to 2 hours of continuous blue light (255 AU) and reporter fluorescence was measured by flow cytometry. Fold-change reporter induction was calculated relative to a dark treatment of each replicate. Bars and error bars represent the mean and standard deviation of 4 biological replicates.

Both Msn2-CLASP and Msn2*-CLASP exhibited a graded response to light doses ranging from 0 – 255 AU and their nuclear concentration plateaued by 128 AU (Figure 5.4A, top panel). These light doses correspond to irradiances of 0 – 405 μW/cm^2 when measured as previously described [71] (see Figure 4.4A). Neither Msn2-dCLASP nor Msn2*-dCLASP localized to the nucleus in response to light and stochastic pulsing into the nucleus was reduced by the inhibitory NLS mutations of Msn2* (Figure 5.4B and Figure 5.4C). As it is sometimes possible to efficiently activate an optogenetic system with a reduced light dose using pulse width modulation (PWM) [76], we also measured nuclear localization for a fixed amplitude (128 AU) light dose pulsed on and off for varying durations (Figure 5.4A, bottom panel). Pulsing the light on for 2 s and off for 1 s caused only a modest decrease (5 – 10%) in nuclear localization compared to continuous illumination, despite a 33% reduction in overall light dose. We therefore selected a maximum working light dose of 128 AU with 2s on, 1 s off PWM for our optogenetic experiments.

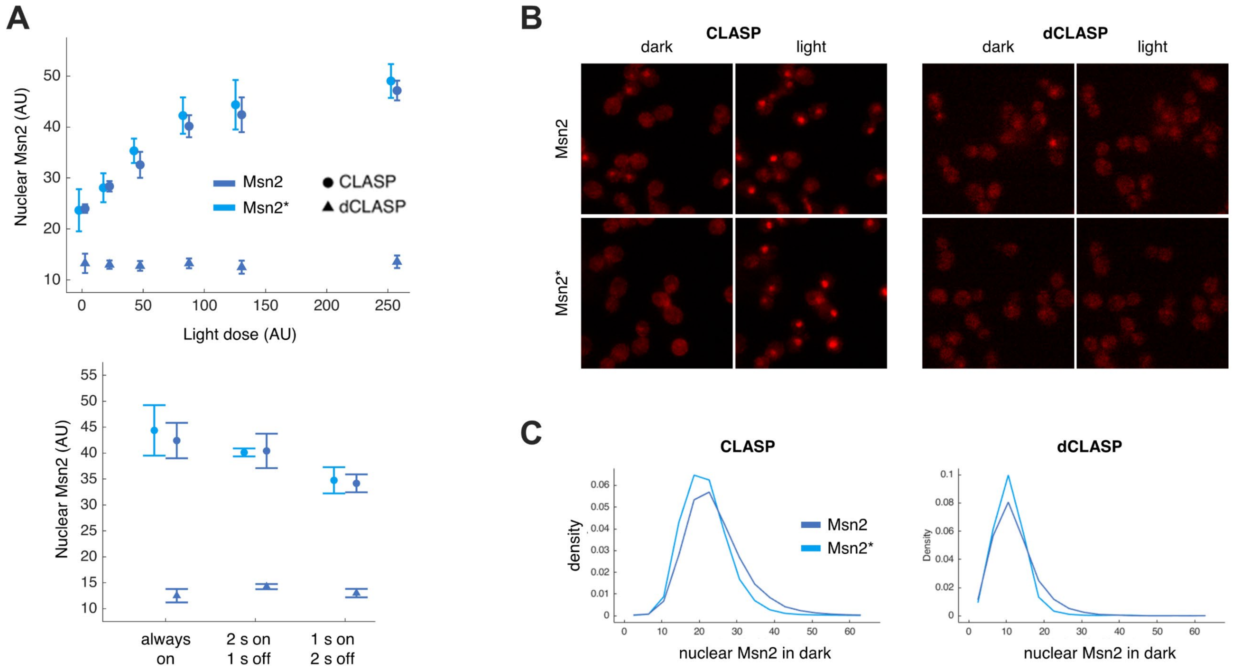

Figure 5.4 Dose-response of Msn2 ± CLASP mutants. (**A**) Absolute nuclear levels of Msn2-CLASP, Msn2*-CLASP, and Msn2-dCLASP were measured in response to 15 min of constant blue light with intensities ranging from 0 – 255 AU (top panel). Nuclear Msn2-CLASP and Msn2*-CLASP in response to 128 AU blue light with varying degrees of PWM (bottom panel). Points and error bars represent the mean nuclear Msn2 level of three biological replicates, each with at least 43 cells. All measurements were acquired by fluorescence microscopy. (**B**) Fluorescence microscopy images showing localization of Msn2 and Msn2* with both CLASP and dCLASP in the dark and in response to 128 AU blue light with 2 s on, 1 s off PWM. (**C**) Histograms show nuclear Msn2 levels prior to illumination across at least 36 experiments for constructs with both CLASP and dCLASP: long right tail for Msn2 constructs reflects stochastic pulsing into the nucleus due to active NLS of Msn2. In contrast, Msn2* constructs have an inactivated NLS and undergo less stochastic pulsing into the nucleus. Overall, Msn2 constructs with CLASP are brighter than those with dCLASP, likely because cytoplasmic sequestration of Msn2 by CLASP prevents degradation triggered by localization to nucleus (see Figure 5.9).

5.3.2 Light sweep experiments reveal promoter decoding of Msn2 localization dynamics

We next used optogenetic control of Msn2* to probe how promoters respond to defined patterns of Msn2* nuclear localization. Using an optoPlate [66] mounted over a 96 well plate on an inverted fluorescence microscope, we delivered time-varying light doses to a reporter strain and imaged the corresponding pulses of Msn2* nuclear localization and any subsequent fluorescent reporter induction (Figure 5.1). Over these “light sweep” experiments, we exposed 12 reporters to a set of 14 light programs that drove Msn2* nuclear localization time-courses with a defined amplitude, duration, or pulsing behavior (Figure 5.5 and Figure 5.22 – Figure 5.25). Excluding a negative control, all reporters featured mCitrine expressed under a promoter with at least one STRE (Figure 5.26A). Each light sweep experiment also included a condition in which Msn2*-dCLASP was exposed to the maximum light dose (50 min 100% amplitude), though no reporter was strongly activated by these conditions (Figure 5.26B), indicating that, without CLASP, Msn2* is not activated by the light doses used.

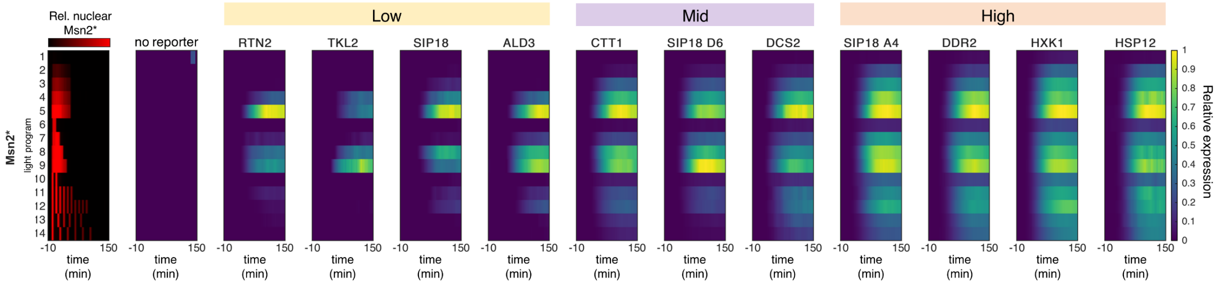

Figure 5.5 Light sweep experiments for Msn2*. Light sweep experiments probe how promoters decode the nuclear localization dynamics of Msn2*. Each row corresponds to a light program, which drove Msn2 localization (left) and subsequent gene expression (right). Msn2* localization measurements were pooled over many experiments and represent thousands of cells per condition. Gene expression measurements were normalized to the maximum expression level per reporter across all conditions. Expression measurements for each condition represent ~100 - 600 cells from at least three biological replicates. See Figure 5.22 – Figure 5.24 for detailed time-courses and Figure 5.25 for detailed description of light programs.

Our light sweep experiments showed that the signal decoding behavior of Msn2 target genes previously reported in response to modulation of PKA activity persists when Msn2 nuclear localization is controlled directly (Figure 5.5). For example, HSP12 and HXK1 were activated by every light program and exhibited a graded response to the area under curve (AUC) of nuclear Msn2*, integrating the Msn2 signal. In contrast, RTN2 and SIP18 were switch-like and filtered out short, low amplitude, and pulsatile pulses of nuclear Msn2*. Having observed these qualitative differences in how promoters respond to Msn2 nuclear localization dynamics, we turned to a mathematical model of gene expression to gain a better understanding of what promoter properties drive this behavior (Figure 5.6 and Section 5.2.5).

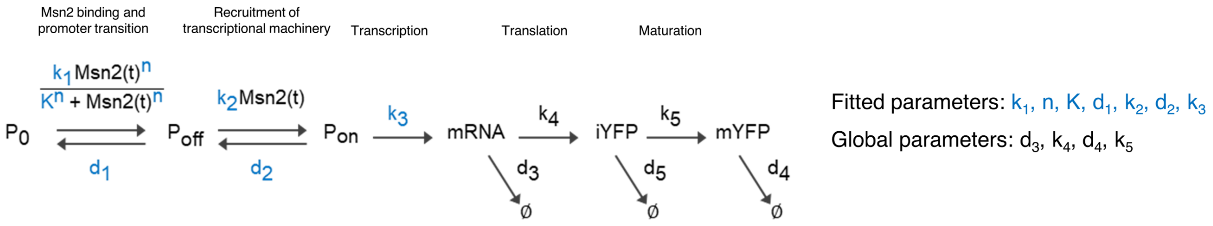

Figure 5.6 Gene expression model. Promoter-specific parameters (blue) were estimated by least squares fitting to the time-resolved mCitrine (YFP) measurements from all light programs. Pooled Msn2 localization measurements were used as the input Msn2(t). Global parameters (black) were the same for all promoters and were taken from the literature. See Section 5.2.5 for corresponding set of ordinary differential equations (ODEs) and Figure 5.22 – Figure 5.24 for plots of model fits over measurements.

We modeled promoter activation as a time-dependent function of nuclear Msn2 that transitions from an initial off state (P_0) to an intermediate off state (P_{off}) to an active, transcribing state (P_{on}). We used this three-state model of promoter activation based on previous reports that a transition between two off states (P_0 and P_{off}) captures the behavior of slow promoters like SIP18 by representing chromatin remodeling steps needed for activation [7], [14], [24]. To capture the switch-like activation of some promoters, we modeled this transition with a Hill function, where K and n capture the half-maximum point and slope of the curve relating nuclear Msn2 concentration to the rate of promoter transition (Figure 5.27). Therefore, K^n represents the sensitivity of a promoter to Msn2 and is related to the binding affinity between the promoter and Msn2, which is determined by the sequence, number, and location of TF binding sites in the promoter as well as other factors like competition and nucleosome occupancy [8], [54], [77], [78]. We pooled Msn2 localization measurements across multiple experiments, then used the resulting composite signal as the model input Msn2(t) and parameterized the model for each promoter by identifying the parameter sets that best fit the gene expression time-courses for all 14 light programs (Figure 5.22 – Figure 5.24). Since a range of parameter sets could predict gene expression with comparable error, we ranked the parameter sets by fit and selected the best performing ones for further analysis (Figure 5.7).

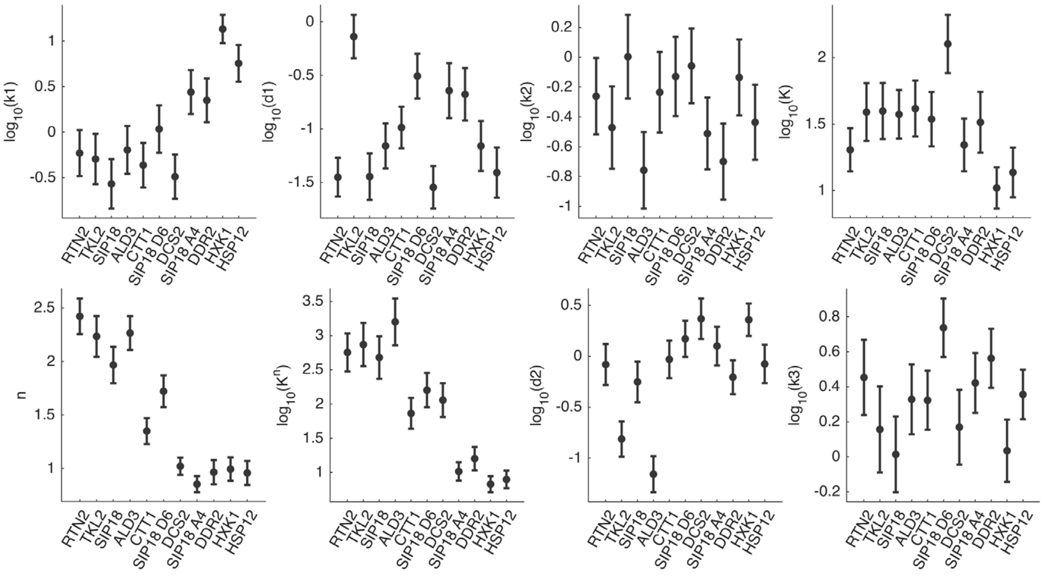

Figure 5.7 Top promoter parameters. Predicted promoter parameters calculated by fitting the light sweep experiment measurements for Msn2* to the gene expression model. Fit results are shown in Figure 5.22 – Figure 5.24. Points and error bars show the mean and 95% confidence interval of each parameter for the top 0.1% of parameter sets (top 100) for each promoter.

5.3.3 Categorizing promoters based on their sensitivity to Msn2

Based on previous studies [7], [8], we used the gene expression model to quantify how the promoters decoded the amplitude and duration of nuclear Msn2*. We simulated gene expression in response to square pulses of nuclear Msn2* that varied in either amplitude or duration and calculated the maximum level of promoter activity (k_3P_{on}) achieved for each pulse. We did this for the top 10 (0.01%) parameter sets for each reporter and identified amplitude thresholds and activation timescales (Figure 5.8A), which respectively describe the amplitude and duration of nuclear Msn2* needed to reach the half-maximum promoter activity, that is, half of the promoter activity attained in response to a 50 min 100% amplitude square pulse of nuclear Msn2* (see Figure 5.28 for details). The amplitude threshold and activation timescale were linearly related (R^2 = 0.69): promoters with low amplitude thresholds (like HXK1, HSP12, SIP18 A4, and DDR2) had short activation timescales, while promoters with high amplitude thresholds (like RNT2, TKL2, SIP18, and ALD3) had long activation timescales.

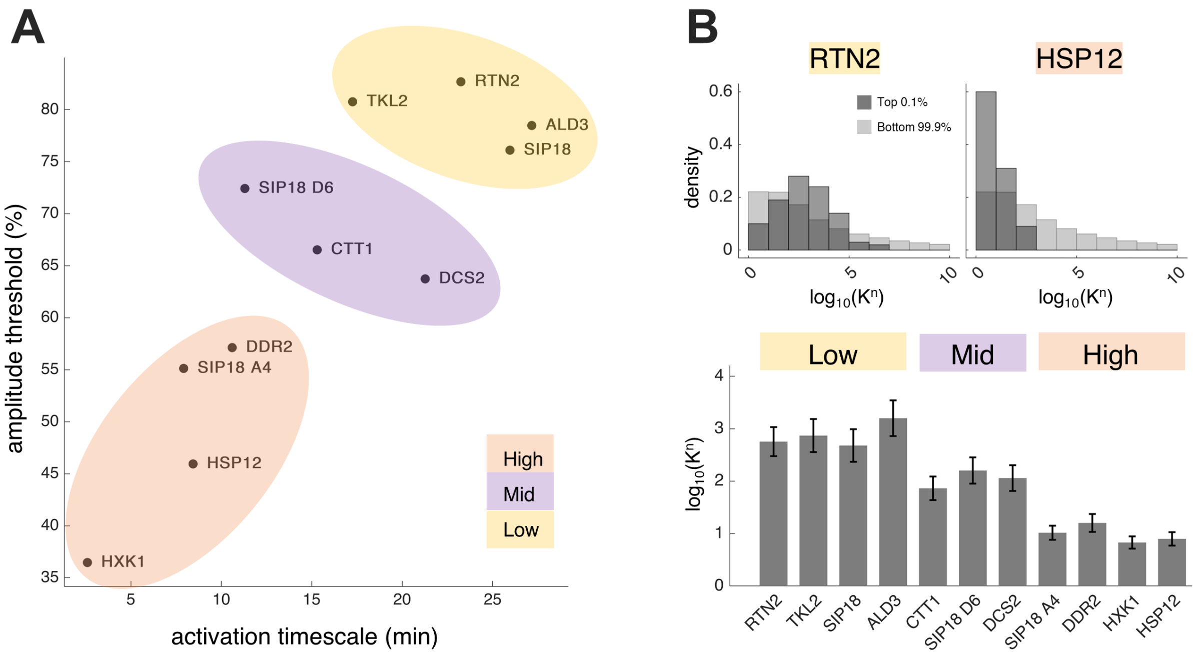

Figure 5.8 Categorizing Msn2 target promoters. (**A**) Categorization of promoters based on how they decoded single pulses of nuclear Msn2*. The amplitude threshold and activation timescale were calculated using the gene expression model and respectively denote the amplitude and duration of nuclear Msn2* needed to reach half the maximum promoter activity (k_3P_{on}) attained by a 50 min 100% amplitude square pulse of nuclear Msn2*. Promoter categories were obtained by k-means clustering of the amplitude thresholds, activation timescales, and predicted values of K^n. (**B**) Predicted values of K^n obtained from the gene expression models of RTN2 and HSP12 expression (top panel). The top 0.1% (top 100) of parameter sets for RTN2 (dark grey) are enriched for high predicted values of K^n versus the bottom 99.9% of parameter

sets (light grey), implying a low affinity for Msn2*. The top parameter sets for HSP12 are enriched for low predicted values of K^n, implying a high affinity for Msn2. Predicted affinity of each promoter for Msn2* where bars and error bars denote the mean and 95% confidence interval of $\log_{10}(K^n)$ for the top 0.1% of parameter sets for each promoter (bottom panel).

Both the amplitude threshold and activation timescale were inversely related to the predicted value of K^n for each promoter. The top parameter sets for promoters with high amplitude thresholds and long activation timescales, like RTN2, were enriched for high values of K^n, implying a low sensitivity for Msn2 (Figure 5.8B, top panel). In contrast, promoters with low amplitude thresholds and short activation timescales, like HSP12, were enriched for low values of K^n, implying a high sensitivity for Msn2. We therefore quantified the sensitivity of each promoter for Msn2 as the mean value of $\log_{10}(K^n)$ for the top 0.1% of parameter sets (Figure 5.8B, bottom panel). Clustering of the amplitude thresholds, activation timescales, and predicted values of K^n revealed three groups of promoters: high, mid, and low sensitivity. The high sensitivity promoters had low predicted values of K^n, low amplitude thresholds, and short activation timescales, reflecting an ability to respond rapidly to small amounts of nuclear Msn2. In contrast, the low sensitivity promoters had high predicted values of K^n, high amplitude thresholds, and long activation timescales, reflecting their tendency to filter out short, low amplitude doses of nuclear Msn2. The mid sensitivity promoters were characterized by intermediate predicted values of K^n and amplitude thresholds but had activation timescales that overlapped both the high and low sensitivity groups.

5.3.4 Nuclear localization triggers Msn2 degradation

Over the course of the light sweep experiments, we observed decay in the Msn2 nuclear localization time-courses (Figure 5.9A) that was consistent with previous reports that nuclear accumulation and binding of DNA causes Msn2 degradation [79]–[81]. The signal decay was not due to photobleaching—it also occurred in light sweep experiments where all images were taken at different positions (Figure 5.29A)—and decreased for an Msn2 mutant incapable of binding DNA (Figure 5.29B). By comparing the measured Msn2 localization time-courses (Figure 5.9A, solid lines) with predicted (or "ideal") time-courses (Figure 5.9A, dotted lines) obtained from a previously published model of Msn2 nuclear localization that does not incorporate degradation [7], we found that degradation began about 14 min after Msn2 first entered the nucleus (Figure 5.9B). Msn2 localization measurements for pulsatile light programs (11, 13, and 14) with different interpulse durations suggested that the degradation process was triggered by nuclear localization of Msn2 but continued outside the nucleus: the first pulses of these light programs were concurrent and had no significant differences in amplitude, but the second pulses were staggered and their amplitudes decreased as the time since the first pulse increased (Figure 5.9C). Degradation did not appear to be thresholded, as there was no obvious pulse amplitude or duration below which degradation did not occur.

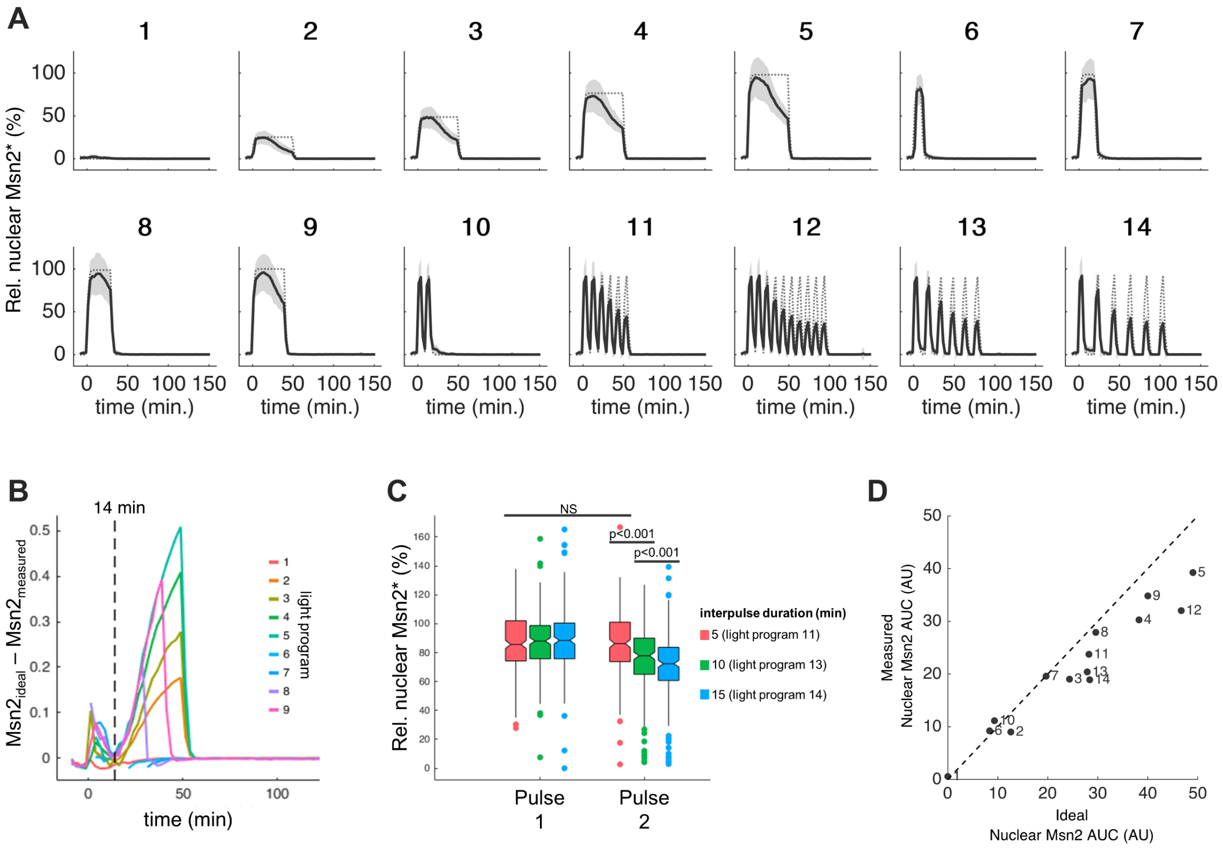

Figure 5.9 Localization triggered degradation of Msn2. (**A**) Measured versus ideal Msn2 localization timecourses showing degradation of Msn2. Solid lines and shaded grey areas represent the mean and standard deviation of Msn2* localization measurements pooled from 79 experiments. Dashed lines represent ideal Msn2 localization (absent degradation) calculated from a computational model of Msn2 localization. (**B**) The difference between measured and ideal Msn2* localization timecourses (Figure 5.9A) shows degradation of Msn2* begins about 14 min after it first enters the nucleus (at t = 0 min). Peaks before 14 min are due to slight (single frame) timing mismatches between the measured and ideal timecourses; larger peaks of this nature were manually excluded from the plot for clarity. (**C**) Msn2 localization measurements for the first and second pulses of light programs 11, 13, and 14, which feature six 5 min pulses of nuclear Msn2 separated by interpulse durations of 5, 10, and 15 min, respectively. Boxplots show localization measurements for each pulse pooled from 79 separate measurements of Msn2(A)*, Msn2*, and Msn2(T)*. Significance was calculated by performing two-sample t-tests between each pair of pulses. (**D**) Measured nuclear Msn2 AUC versus ideal nuclear Msn2 AUC per light program. Measured Msn2 AUC deviated from ideal Msn2 AUC most strongly for long duration light programs.

Msn2 degradation cofounds simple comparisons between light programs, as there was a mismatch between the AUC of the measured nuclear Msn2 signal and the AUC of the ideal of nuclear Msn2 signal (Figure 5.9D). The mismatch was pronounced for long duration light programs with the same overall light dose but different pulsing behavior: for 30 min of continuous illumination (light program 8), the measured and ideal AUC were roughly equal, while six 5 min pulses of illumination separated by 15 min (light program 14) had a similar ideal AUC but a much lower measured AUC, as degradation caused the maximum attainable pulse amplitude to decrease with time. Consequently, Msn2 degradation may act as a timer on gene expression, particularly for low sensitivity promoters, which are poorly expressed when Msn2 levels drop below their high amplitude thresholds.

5.3.5 Changing DNA-binding ability of Msn2 has strongest effect on low sensitivity genes

TFs have a range of DNA binding affinities, but are often tuned for function and exhibit sub-maximal binding affinity for their target sites [82]. Previous work showed that increasing or decreasing the DNA binding affinity of Msn2 respectively increases or decreases the expression of a target gene at steady-state [54]. However, our gene expression model predicted that the effects of such changes are highly promoter dependent (Figure 5.10A): they had a stronger effect on the predicted expression of low sensitivity genes like RTN2 than on high sensitivity genes like HSP12. Moreover, it was unclear how changing the DNA binding affinity of a TF would affect the ability of its target promoters to decode its nuclear localization dynamics.

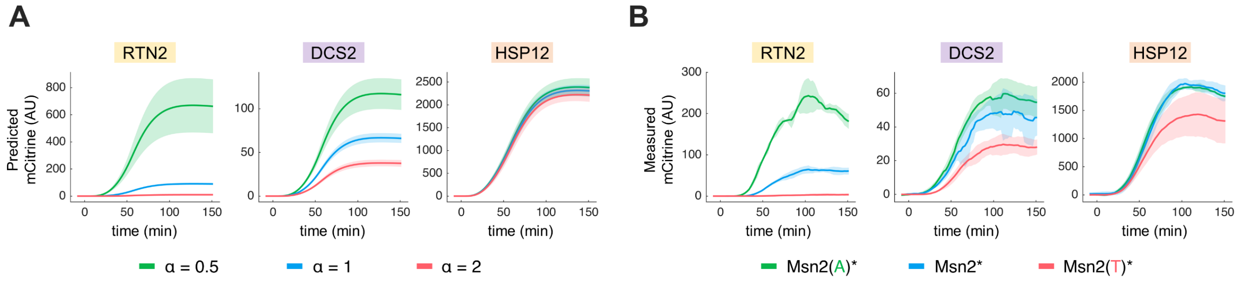

Figure 5.10 Predicted versus measured expression of Msn2 affinity mutants. (**A**) Predicted gene expression for low (RTN2), mid (DCS2), and high (HSP12) sensitivity promoters was calculated by simulating the response of each promoter to a 50 min 100% amplitude pulse of nuclear Msn2* while scaling the K term in the gene expression model (see Figure 5.6) by a factor α, equaling either 2, 1, or 0.5. Lines

and shaded regions represent the mean and 95% confidence interval of the predicted expression for the top 10 parameter sets. (**B**) Measured expression of high and low sensitivity genes following a 50 min 100% amplitude pulse of Msn2(A)*, Msn2*, and Msn2(T)*. Lines and shaded regions represent the mean and standard deviation of expression for three biological replicates.

To experimentally investigate the interaction of Msn2 localization dynamics and DNA binding ability, we introduced additional mutations into Msn2* to alter its ability to bind DNA. The DBD of Msn2 features two zinc fingers connected by a short linker sequence that together target Msn2 to bind STREs (Figure 5.11). We created a high activity DBD mutant, Msn2(A)*, by making a serine to alanine mutation at the S686 site within the second zinc finger based on studies showing that it causes Msn2 hyperactivity [55], [83]. We made a low activity DBD mutant, Msn2(T)*, by introducing three mutations (S671T, N672G, R674K) to the linker sequence based on a previous study showing that it decreased Msn2 activity [54]. Both Msn2(A)* and Msn2(T)* localized similarly to Msn2* (Figure 5.25B).

Figure 5.11 Msn2 DBD mutants. Schematic depiction of the DNA binding domains (residues 645 – 704) of Msn2*, Msn2(A)* and Msn2(T)*. Canonical recognition residues that contact DNA are highlighted in grey. Msn2* has a WT DBD, Msn2(A)* features an S686A mutation within the second zinc finger, and Msn2(T)* features three mutations (S671T, N672G, R674K) within the linker region of the Msn2 DBD.

To measure how changes to the DNA binding ability of Msn2 affect promoter decoding of its nuclear localization dynamics we performed additional light sweep experiments with Msn2(A)* and Msn2(T)* (Figure 5.10B and Figure 5.12). In general, increasing the DNA binding ability of Msn2 increased expression and reduced the amplitude threshold and activation timescale of a promoter such that lower pulse amplitudes and durations were needed to achieve a given level of promoter activity (Figure 5.30). In agreement with the model predictions, these changes had a strong effect on the expression of low sensitivity promoters like RTN2 and a comparatively weak effect on the expression of promoters with a high predicted sensitivity for Msn2 like HSP12 (Figure 5.10B).

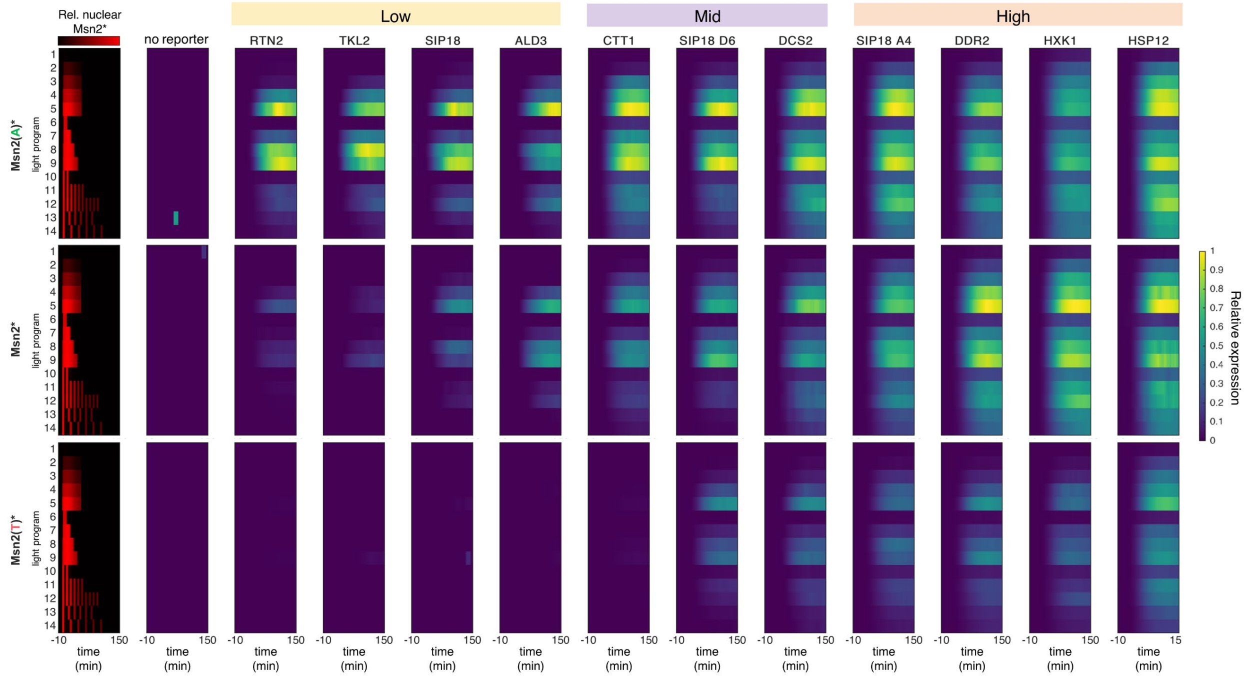

Figure 5.12 Light sweep experiments for all Msn2 DBD mutants. Light sweep experiments probing how promoters decode the nuclear localization dynamics of Msn2(A)*, Msn2*, and Msn2(T)*. Each row corresponds to a light program, which drove Msn2 localization (left) and subsequent gene expression (right). Msn2 localization measurements were pooled over many experiments and represent thousands of cells per condition. Gene expression measurements were normalized to the maximum expression level per reporter across all conditions and Msn2 DBD mutants. Expression measurements for each condition represent ~100 - 600 cells from at least three biological replicates. See also Figure 5.22 – Figure 5.24**.**

Overall, the high sensitivity promoters were strongly induced by all three Msn2 DBD mutants (Figure 5.12) and differences in their expression between mutants were typically small compared to the low sensitivity promoters. For example, there was no significant difference in maximum HSP12 expression between Msn2(A)* and Msn2* and maximum HSP12 expression for Msn2(T)* was 0.7-fold that of Msn2* (Figure 5.13A). Expression of these promoters generally increased linearly with nuclear Msn2 AUC, though in some cases approached saturation at high pulse amplitudes (Figure 5.13A and Figure 5.13B). There was no high sensitivity promoter where expression for Msn2(A)* was significantly higher than for Msn2*, suggesting that there was little benefit to further increases in the DNA-binding ability of Msn2 itself for activating high sensitivity promoters. In fact, doing so may have a cost, as expression of the high sensitivity genes HXK1 and DDR2 was weakly, but consistently lower for Msn2(A)* versus Msn2 (Figure 5.24).

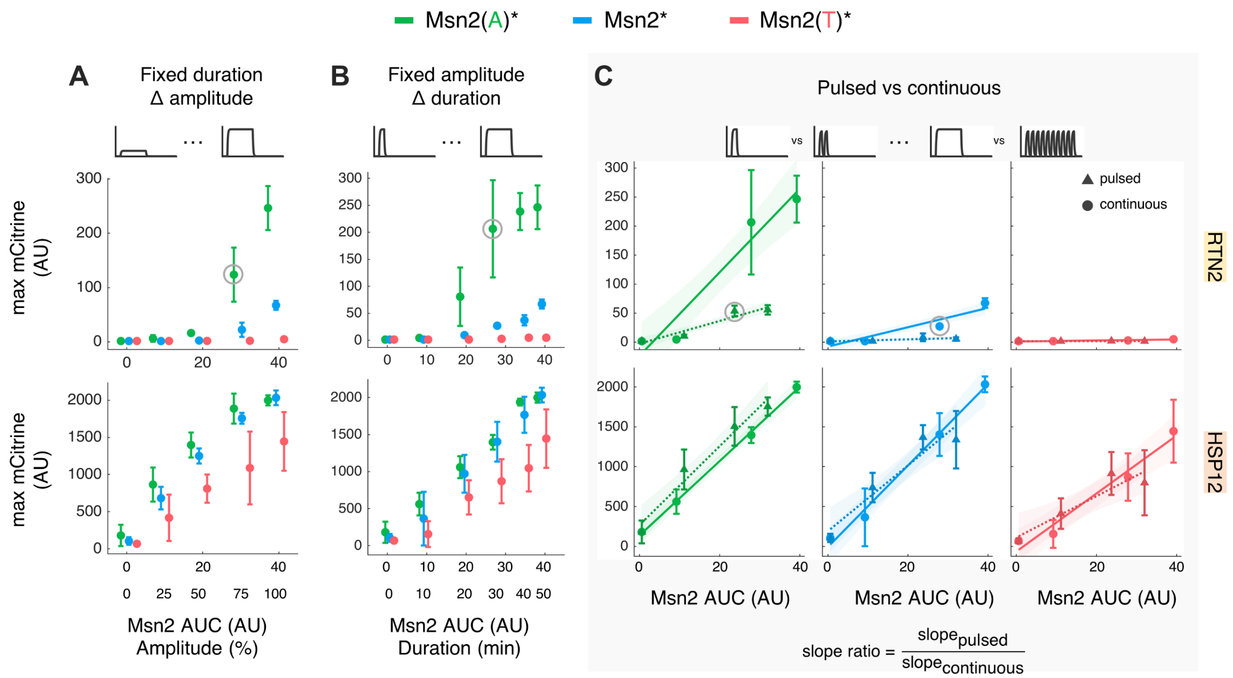

Figure 5.13 Signal decoding behavior of high and low sensitivity promoters. Maximum reporter expression following (**A**) a 50 min pulse of each Msn2 DBD mutant with amplitudes ranging from 0 – 100% or (**B**) a 100% amplitude pulse of nuclear localization with durations ranging from 0 – 50 min. (**C**) Maximum fluorescent reporter expression in response to continuous vs pulsed doses of each Msn2 DBD mutant. Circles represent maximum expression following 0, 10, 30, or 50 min continuous pulses of 100% amplitude nuclear Msn2. Triangles represent maximum expression following 0, 2, 6, or 10 five min pulses of nuclear Msn2 with 100% amplitude and 5 min interpulse durations. In all plots, points and error bars represent mean and standard deviation of expression for three biological replicates. Solid and dashed lines show best fit lines for continuous and pulsed conditions, respectively; shaded regions show 95% confidence interval of the best fit lines. Slope ratios were calculated as the slope of the best fit line for the pulsed conditions divided by the slope of the best fit line for the continuous conditions and are shown in Figure 5.13B. Grey circles denote measurements referenced in text.

In contrast, there were generally large expression differences between Msn2 DBD mutants for the low sensitivity promoters (Figure 5.12). Msn2(T)* failed to activate these promoters in most cells, while Msn2(A)* increased their expression versus Msn2* and effectively enabled their induction in conditions where Msn2* did not. For example, Msn2(A)* increased the maximum expression of RTN2 by 3.7-fold (Figure 5.13A) and allowed its induction for pulsatile doses of nuclear localization—in fact, expression of RTN2 was 1.9-fold higher for six 5 min pulses of Msn2(A)* than a 30 min continuous pulse of Msn2* (circled points, Figure 5.13C). The generally linear relationship between expression and Msn2 AUC observed for high sensitivity promoters did not hold for low sensitivity promoters. Instead, low sensitivity promoters like RTN2 filtered out pulses of nuclear localization with low amplitudes or durations. Activation of these promoters was especially dependent on the nuclear concentration of Msn2: maximum RTN2 expression (circled points of Figure 5.13A and Figure 5.13B) for a 30 min 100% amplitude pulse of Msn2(A)* (AUC = 26.8) was 1.7-fold higher than for a 50 min 75% amplitude pulse (AUC = 28.2) and the other low sensitivity promoters behaved similarly. Notably, the expression of low sensitivity genes like SIP18 and TKL2 plateaued for pulses of nuclear Msn2 longer than 30 min (Figure 5.14). This is consistent with Msn2 degradation acting as a timer on the expression of genes with high amplitude thresholds, as the predicted expression of these promoters plateaued when the measured Msn2 localization time-courses (with decay) were used as an input to our gene expression model, but continued increasing with pulse duration when the ideal Msn2 localization time-courses (without decay) were used.

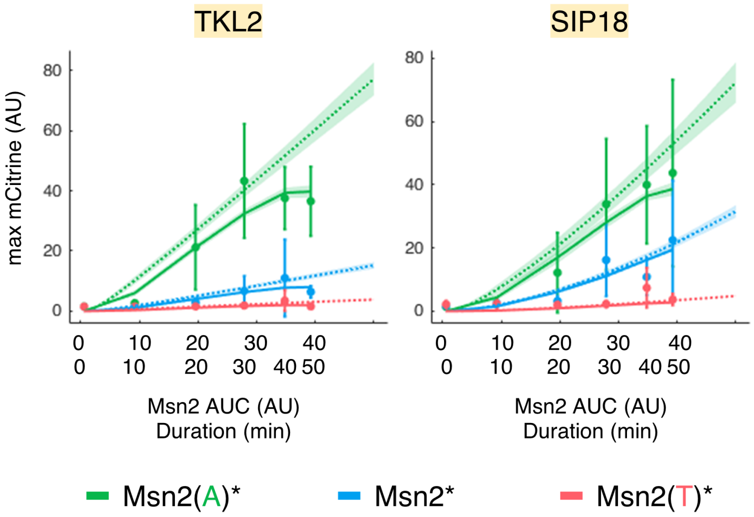

Figure 5.14 Degradation causes expression of low sensitivity promoters to plateau. Comparison of measured and predicted expression of TKL2 and SIP18 using the top 10 parameter sets for each reporter and Msn2 DBD mutant. Points and error bars show mean and standard deviation of measured expression for three biological replicates. Solid lines and shaded regions show the mean and 95% confidence interval of predicted expression for the measured pulses of Msn2 nuclear localization, which like the expression measurements, plateau for pulses longer than 30 min. In contrast, dashed lines and shaded regions show the mean and 95% confidence interval of predicted expression for 100% amplitude ideal pulses of each Msn2 DBD mutant with durations ranging from 0 – 50 min, which do not plateau—suggesting that degradation of Msn2 beyond 30 min reduces its ability to activate promoters with high amplitude thresholds.

5.3.6 Relative ability to respond to pulsed versus continuous doses of nuclear Msn2 is primarily set by the promoter

We next investigated how promoters decoded pulsatile doses of Msn2 nuclear localization. We calculated slope ratios [14] that quantified the relative ability of each promoter to respond to similar pulsatile versus continuous doses of each Msn2 DBD mutant (Figure 5.13C) by fitting lines the measurements and dividing the pulsed slopes by the continuous slopes (**Figure 4B**). A slope ratio greater than one indicates stronger promoter induction by a pulsatile dose of nuclear Msn2 than a continuous dose, while a slope ratio less than one indicates the opposite.

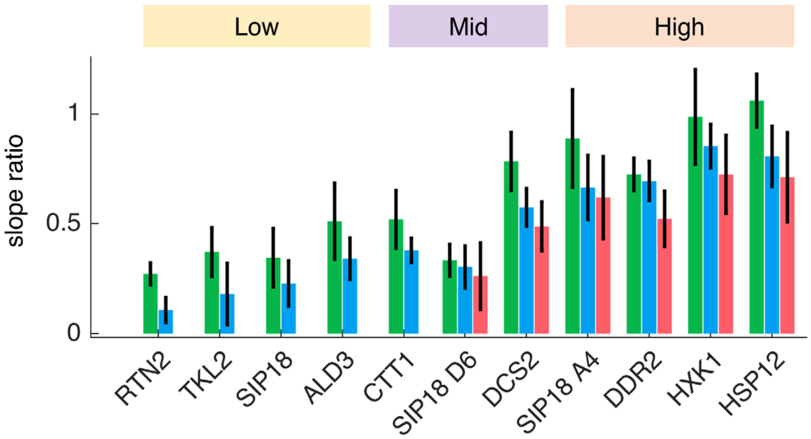

Figure 5.15 Promoter response to continuous versus pulsed Msn2. Slope ratios were calculated as described for Figure 5.13C. Bars and error bars represent the mean and standard deviation of the slope ratio for each promoter and Msn2 DBD mutant.

The high sensitivity promoters responded strongly to pulsatile doses of nuclear Msn2 and, as with continuous doses, there was a generally linear relationship between their expression and nuclear Msn2 AUC. Accordingly, the high sensitivity promoters had high slope ratios (Figure 5.15), though only HSP12 had a slope ratio above one, for Msn2(A)*. On the other hand, low sensitivity promoters like RTN2 were poorly activated by pulsatile doses of nuclear Msn2 (Figure 5.13C) and consequently had low slope ratios (Figure 5.15). While there were clear differences in slope ratio between promoters, changing the DNA binding ability of Msn2 had a relatively weak effect on a promoter's ability to respond to pulsed versus continuous doses of nuclear Msn2. The slope ratio of each promoter was always highest for Msn2(A)* and lowest for Msn2(T)*, though this may be a consequence of degradation, which disproportionally affected the pulsatile light doses (Figure 5.9D) and can cause nuclear Msn2 levels to drop below the elevated amplitude thresholds associated with a decrease in DNA binding ability. This suggests that that the relative ability to respond to pulsed versus continuous doses of nuclear Msn2 is primarily set by the promoter. However, in a practical sense, changing the DNA-binding ability of Msn2 changed its absolute ability to activate genes in pulsatile conditions: low sensitivity promoters like RTN2, TKL2, and

SIP18 were activated more strongly and in a wider range of pulsatile conditions by Msn2(A)* than Msn2* (Figure 5.12).

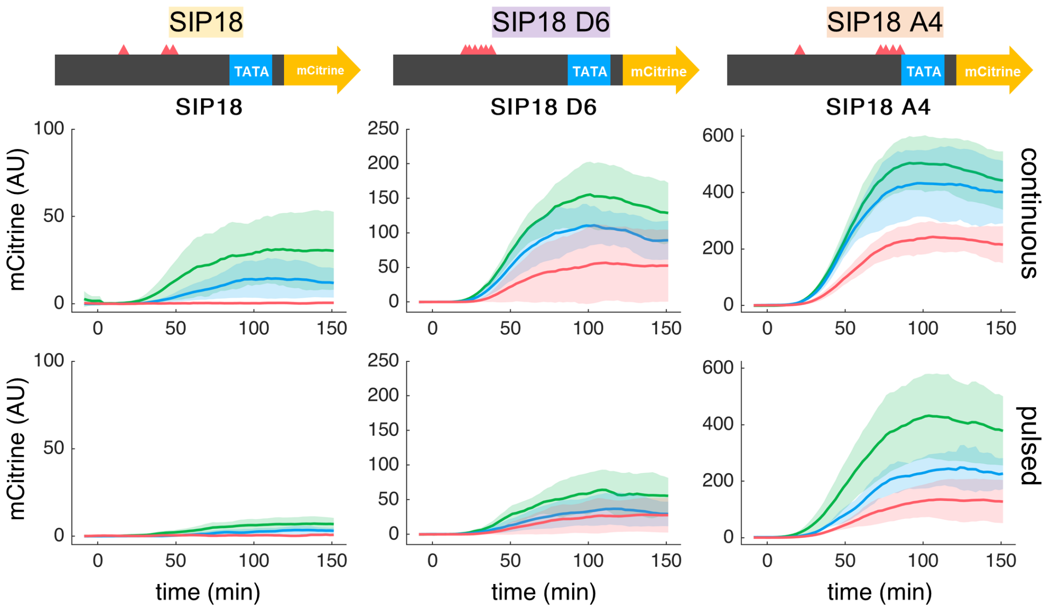

Figure 5.16 Mutating Msn2 DBD versus mutating promoter. Expression of SIP18-based promoters following a 30 min 100% amplitude pulse of nuclear Msn2 (continuous) or six 5 min 100% amplitude pulses with 5 min interpulse durations (pulsed). Lines and shaded regions represent the mean and standard deviation of expression for three biological replicates. Schematic depictions of each promoter (top) show location of TATA box and STREs within region 750 bp upstream of mCitrine.

In contrast, changing the structure of a promoter can change its relative ability to respond to pulsed versus continuous doses of nuclear Msn2, as can be seen by comparing the expression of SIP18 and the synthetic promoters SIP18 D6 and SIP18 A4 (Figure 5.16). The low sensitivity promoter SIP18 was weakly induced by pulsatile doses of nuclear Msn2* (slope ratio = 0.23). Replacing its native STREs with a cluster of four STREs near the TATA box converted it to the high sensitivity promoter SIP18 A4, which was much more responsive to pulsatile doses of nuclear Msn2* (slope ratio = 0.67). Conversely, replacing the native STREs of SIP18 with six STREs distal to the TATA box converted it to the mid sensitivity promoter SIP18 D6, which remained poorly induced by pulsatile doses of nuclear Msn2* (slope ratio = 0.30). Overall, increasing DNA-binding by either mutating SIP18 or mutating Msn2 generally increased gene expression and reduced the amplitude and duration of nuclear localization needed for activation (Figure 5.16 and Figure 5.30), but only mutating the promoter strongly affected its relative ability to respond to pulsed versus continuous doses of nuclear Msn2.

5.3.7 Expression noise increased for pulsatile dynamics and low Msn2 affinity

We next investigated if there were differences in the cell-to-cell variability of gene expression (noise) between promoters, Msn2 DBD mutants, and different patterns of nuclear localization (Figure 5.17A). There were large differences in noise between promoters: for a 30 min continuous pulse of nuclear Msn2*, noise for the low sensitivity promoters was at least five-fold higher than any high sensitivity promoter. Msn2 nuclear localization dynamics also affected gene expression noise, which was always higher for pulsed doses of nuclear Msn2 than continuous doses. Overall, there was a negative correlation ($R^2 = 0.81$) between the maximum expression of a promoter and its noise (Figure 5.31, such that decreasing the DNA binding ability of Msn2 also increased gene expression noise, particularly for low sensitivity promoters.

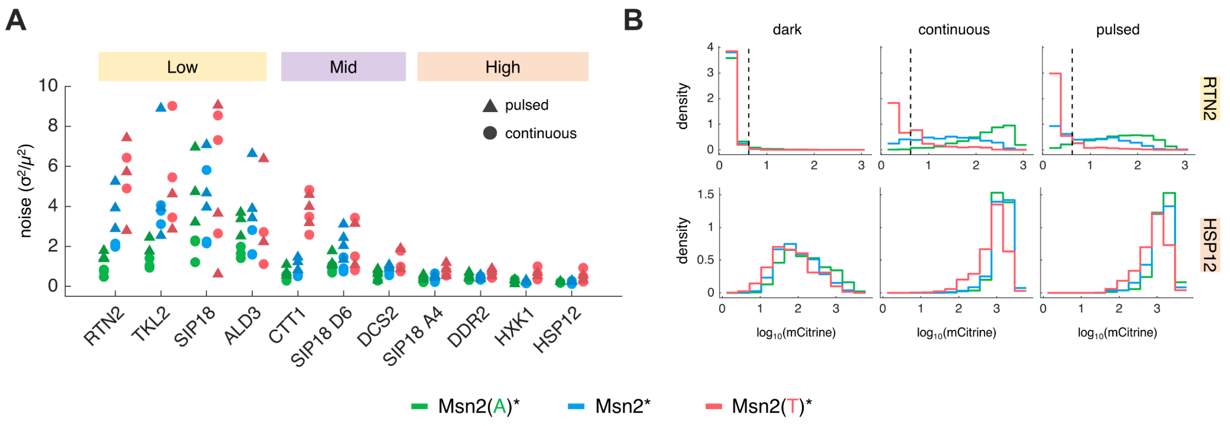

Figure 5.17 Expression noise increased for pulsatile dynamics and decreased Msn2 affinity. (A) Noise levels following a 30 min 100% amplitude pulse of nuclear Msn2 (circles) or six 5 min 100% amplitude pulses with 5 min interpulse durations (triangles). Noise level was calculated per timepoint as σ^2/μ^2 of all single-cell mCitrine measurements. Each point represents the average noise level of a single biological

replicate for all timepoints greater than 120 min. (**B**) Fluorescent reporter expression for cells exposed to no light, a 30 min 100% amplitude pulse of nuclear Msn2 (continuous), or six 5 min 100% amplitude pulses with 5 min interpulse durations (pulsed). Each histogram represents the distribution of single-cell fluorescence measurements of three biological replicates for a 10 min time window centered at 120 min. Dashed line represents threshold above which RTN2 was considered active and was calculated as the 99th percentile RTN2 level for the no light condition.

Looking at single-cell measurements of gene expression (Figure 5.17B) revealed that pulsatile doses of Msn2(T)* robustly activated HSP12 while minimizing the expression of RTN2: just 13.8% of cells (weakly) expressed RTN2 following six 5 min pulses of Msn2(T)* versus 39.0% of cells following 30 min of continuous Msn2(T)*. Reduced activation of RTN2 comes at a cost of increased HSP12 noise. However, mean HSP12 noise following pulsatile Msn2(T)* was still eight-fold less than the minimum noise level for a low sensitivity promoter following pulsatile Msn2* (Figure 5.17A). In contrast, a 30 min continuous pulse of Msn2(A)* strongly activated both HSP12 and RTN2 (Figure 5.17B), but with 67% less noise in RTN2 expression than a 30 min pulse of Msn2*.

5.3.8 Sensitivity analysis reveals that slow activation or fast deactivation kinetics cause the relative expression for the Msn2 DBD mutants to diverge

In previous sections of this work, we focused on how high and low sensitivity promoters responded to the nuclear localization dynamics of each Msn2 DBD mutant because these promoters exhibited consistent behavior. In contrast, the mid sensitivity promoters (intermediate K^n) behaved less consistently. Though they all had intermediate amplitude thresholds, the mid sensitivity promoters had a wide range of activation timescales (Figure 5.8A) and decoding behaviors. DCS2 behaved like a high sensitivity promoter in many respects: it was strongly activated by all three Msn2 DBD mutants even for pulsatile doses of nuclear localization (Figure 5.12), but was weakly expressed and had a relatively long activation timescale (Figure 5.8A). SIP18 D6 was also activated by all three Msn2 DBD mutants, but like the low sensitivity promoters, was poorly induced by pulsatile doses of nuclear localization. CTT1 behaved like a low sensitivity promoter in that it was not induced by Msn2(T)* (Figure 5.12), but had a comparatively low amplitude threshold and short activation timescale (Figure 5.8A). That these promoters had similar predicted sensitivities to Msn2* but different behaviors suggested that other promoter properties also affect the response to changes in TF binding ability.

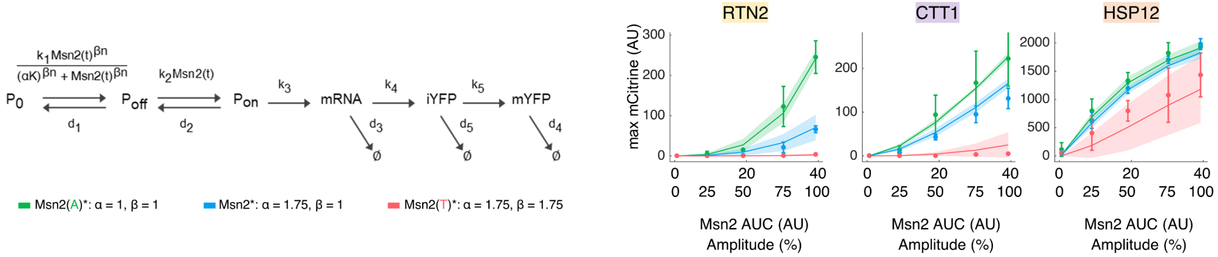

Figure 5.18 Modeling DNA binding differences between Msn2 DBD mutants. (Left) The gene expression model was used to identify scaling factors (α and β) that represent affinity differences between Msn2 DBD mutants. The scaling factors were calculated by repeatedly simulating the expression of each reporter using the top 10 parameter sets for Msn2(A)* while scaling α and β to minimize the difference between the predicted expression and the expression measured for Msn2* or Msn2(T)* across all light programs and reporters. See also Figure 5.32. (Right) Simulated versus measured expression for the chosen scaling factors. Points and error bars show mean and standard deviation of maximum expression measured for three biological replicates of each Msn2 DBD mutant following a 50 min pulse of continuous nuclear localization with amplitudes varying from 0 – 100%. Lines and shaded regions represent mean and 95% confidence interval of expression predicted for each Msn2 DBD mutant over the same set of conditions using the top 10 parameter sets for Msn2(A)* and the indicated values of α and β

To explore which properties of a promoter cause differential responses to the Msn2 DBD mutants, we sought to perform a sensitivity analysis on our gene expression model. We therefore needed to incorporate differences in the DNA-binding ability of the Msn2 DBD mutants into the model. To capture how changes in binding ability may affect both the half-maximum point and shape of the curve relating nuclear Msn2 concentration to promoter activation, we identified factors (α and β) by which we could scale K and n to represent binding differences between the Msn2 DBD mutants (Figure 5.18). Since Msn2(A)* activated the most reporters in the most conditions, we did this by first parameterizing the model with the measurements for Msn2(A)* and then searching for values of α and β that recapitulated the expression measured for Msn2* or Msn2(T)*. We found that scaling K and n by α = 1.75 and β = 1, respectively, best approximated the expression measured for Msn2* (Figure 5.18 and Figure 5.32). Similarly, scaling factors of α = 1.75 and β = 1.75 approximated the expression of Msn2(T)*, though other pairs of scaling factors performed comparably. This approach assumes α = 1 and β = 1 for Msn2(A)*.

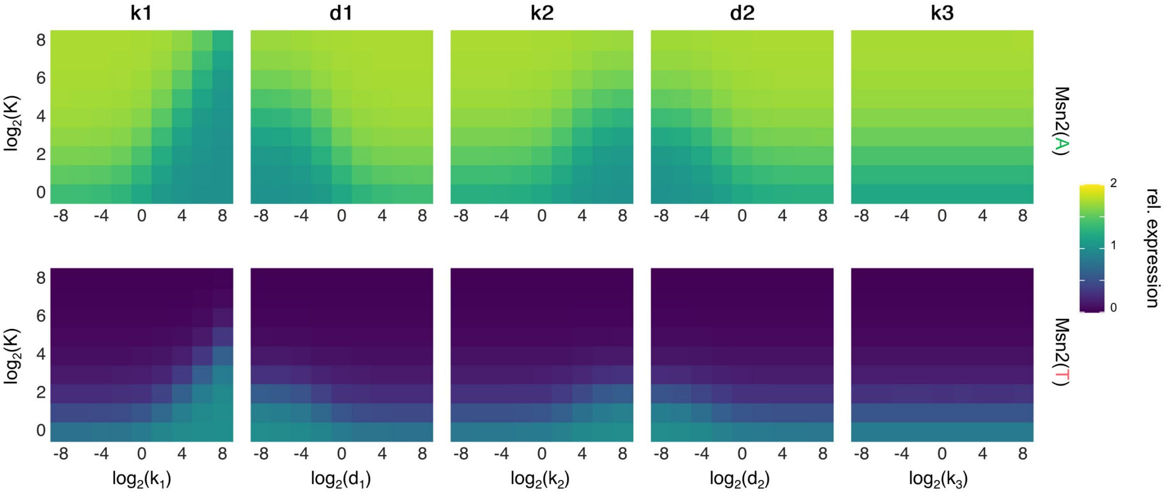

Figure 5.19 Sensitivity analysis of gene expression model. Simulations showing how promoter parameters affect expression for Msn2(A)* and Msn2(T)* relative to Msn2*. Expression of hypothetical promoters was simulated in response to a 50 min 100% amplitude pulse of each Msn2 DBD mutant using the values of α and β identified in Figure 5.18. Over the simulations, each kinetic parameter (k_1, d_1, k_2, d_2, k_3) was allowed to vary along with K (n was fixed to one). For each hypothetical promoter, relative expression was calculated by normalizing the maximum expression in response Msn2(A)* or Msn2(T)* to the maximum expression in response to Msn2*

We then used the identified values of α and β to simulate the expression of hypothetical promoters in response to a 50 min 100% amplitude pulse of each Msn2 DBD mutant. We individually scaled the kinetic parameters k_1, d_1, k_2, d_2, and k_3 over a range of values of K and n and for each hypothetical promoter calculated the maximum expression for each Msn2 DBD mutant (Figure 5.33), as well as the relative expression versus Msn2*, which we calculated by normalizing the maximum expression for each Msn2 DBD mutant to the maximum expression for Msn2* (Figure

5.19). As expected, decreasing promoter sensitivity (by increasing K or n) caused absolute expression to decrease and the relative expression to diverge, while increasing promoter sensitivity (by decreasing K or n) had the opposite effect. Changes to promoter sensitivity were especially consequential for Msn2(T)*, which was effectively nonfunctional over a large range of promoter sensitivities where Msn2* and Msn2(A)* were still potent inducers (Figure 5.33). Except at low promoter sensitivities (high K or n) where expression differences between Msn2 DBD mutants were always large, slow activation kinetics (low k_1 or k_2) or fast deactivation kinetics (high d_1 or d_2) caused the expression for Msn2(A)* and Msn2(T)* to diverge from the expression for Msn2*, while scaling the rate of transcription k_3 had no effect on relative expression (Figure 5.19). Decreasing the promoter transition rate (k_1) caused the relative expression to diverge by increasing the relative contribution of TF DNA-binding ability to the rate of transition from P_0 to P_{off}, while increasing d_1 prevented any gains in P_{off} from accruing. Likewise, decreasing the on rate k_2 or increasing the off rate d_2 prevented gains in P_{off} from being converted to the productive state P_{on}. These simulations show that it is possible for promoters with similar sensitivities but different kinetic parameters to have divergent responses to the Msn2 DBD mutants, as was the case with the mid sensitivity promoters CTT1 and DCS2.

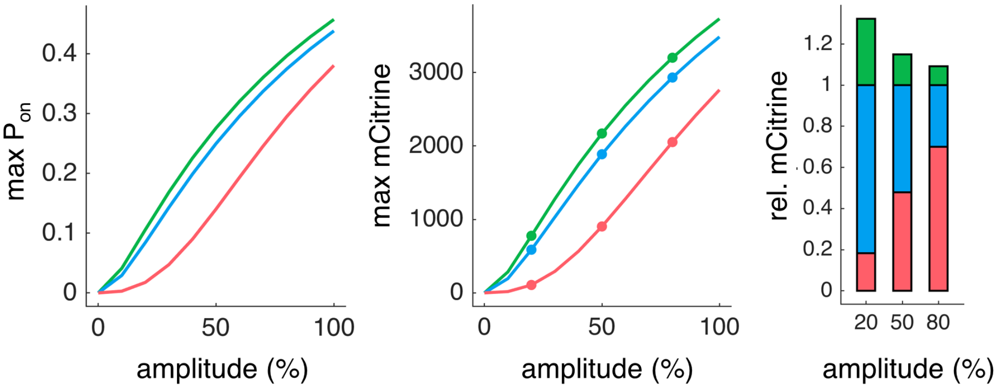

Figure 5.20 Expression for Msn2 DBD mutants diverges at low pulse amplitudes. Maximum P_{on} (left panel), maximum expression (middle panel), and relative expression were calculated for a hypothetical promoter ($k_1 = 1$, $d_1 = 1/16$, $k_2 = 1$, $K = 2$, $n = 1$, $d_2 = 1$, $k_3 = 1$) following 50 min ideal pulses of each Msn2 DBD mutant with amplitudes ranging from 0 – 100%.

We next used the gene expression model to explore how changes in nuclear localization dynamics may cause expression differences between the Msn2 DBD mutants. We repeated the simulations described above, but for ideal pulses of each Msn2 DBD mutant with varying amplitudes, durations, or interpulse durations (Figure 5.34). As with scaling the kinetic parameters, there was little scope to drive changes in the relative expression of low sensitivity promoters by changing the nuclear localization dynamics, though for higher sensitivity promoters, decreasing the amplitude of localization generally caused expression to diverge (Figure 5.20), since decreasing the concentration of nuclear Msn2 increased the relative contribution of DNA-binding ability to the rate of transition from P_0 to P_{off}. Such behavior can be seen in our measurements of RTN2, where expression for the Msn2 DBD mutants diverges with increasing pulse amplitudes, and HSP12, where expression converges (Figure 5.13). In contrast, changing the duration of a single pulse of nuclear localization or the interpulse duration between multiple pulses had little effect on the relative expression of each hypothetical promoter (Figure 5.34B and Figure 5.34C).

5.3.9 Changing Msn2 affinity alters a promoter’s ability to discriminate between stresses

Since the DNA binding ability of Msn2 is not known to be regulated by PTMs, we reasoned that changing the DNA binding ability of Msn2 might disrupt the ability of its target genes to filter the nuclear localization dynamics generated by natural stresses. In particular, because Msn2(A)* was able induce low sensitivity promoters like RTN2 and TKL2 in response to pulsatile doses of nuclear localization where Msn2* and Msn2(T)* could not, we predicted that it may similarly be better at inducing these genes in response to glucose starvation, which is known to cause an initial, coherent burst of Msn2 nuclear localization followed by sporadic pulses of nuclear translocation [6].

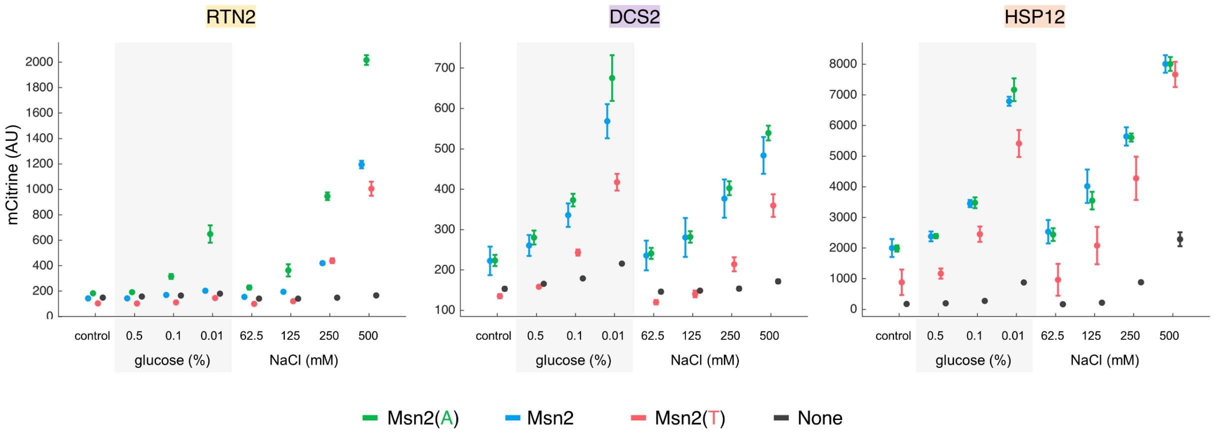

Figure 5.21 Changing Msn2 affinity affects discrimination of stresses by promoters. Fluorescent reporter expression following 2 hours of glucose starvation or hyperosmotic shock. All Msn2 mutants were expressed in the dCLASP system and had no mutations outside the DBD. Points and error bars represent mean and standard deviation of fluorescence for at least three biological replicates. See also Figure **S12A.**

We therefore measured reporter expression for Msn2, Msn2(A), and Msn2(T)—all without CLASP or any mutations outside their DBDs—in response to glucose starvation and hyperosmotic shock (Figure 5.21 and Figure 5.35), which also causes an initial burst of localization, but with fewer subsequent sporadic pulses [6]. Overall, expression of most promoters was highest for Msn2(A) and lowest for Msn2(T). While all three Msn2 DBD mutants activated the low sensitivity genes RTN2 and TKL2 in response to hyperosmotic shock, only Msn2(A) activated them in response to glucose starvation. In essence, these genes lost their ability to discriminate between the stresses when the DNA binding affinity of Msn2 was increased. This was not due to differences in localization behavior, as both Msn2(A) and Msn2 localized similarly in response to either stress (Figure 5.35B). Excluding DDR2, which was most strongly induced by Msn2, there were few significant differences in the expression of the high sensitivity promoters between Msn2(A) and Msn2, which may agree our model's predictions that at a point there is little benefit to further increases in TF binding ability.

5.4 Discussion

Cells may encode environmental information in the temporal dynamics of TF activation. Yet TFs are subject to spurious bursts of activation due to minor fluctuations in their environment or upstream signaling cascades. In the absence of stress, Msn2 can stochastically pulse in and out of the nucleus, yet only a small subset of cells show heightened activation of its target genes [33]. This suggests a need for promoters to decode Msn2 dynamics and filter out noisy signals. Indeed, previous work by Hansen and O'Shea showed that Msn2 target genes exhibit differential responses to different patterns of Msn2 nuclear localization generated by modulating PKA activity. However, other downstream targets of PKA include the TFs Hsf1, Sok2, and Dot6 and components of the RNA polymerase II holoenzyme, which also regulate gene expression [10]–[12], [34]. Our measurements show that the signal decoding behavior of Msn2 target genes persists when Msn2* localization is controlled directly. The promoters acted as filters of Msn2 localization dynamics: low sensitivity genes filtered out low amplitude, short duration, and pulsatile doses of nuclear Msn2, while high sensitivity genes were readily induced by nuclear Msn2, effectively integrating the nuclear Msn2 signal. These results were broadly consistent with those of Hansen and O'Shea, though some promoters behaved differently than expected: DCS2 and RTN2 were less readily activated and SIP18 D6, which was previously reported to have a low amplitude threshold and high activation timescale, had intermediate values of both. Accordingly, we observed no decoupling of amplitude threshold and activation timescale, which were linearly related for all promoters measured. Such differences are possibly due to differences in methodology. Apart from using optogenetic rather chemical control of Msn2, we used fluorescent reporters integrated at the URA3 locus rather than at the open reading frame (ORF) of each reporter gene and there was substantial decay in our nuclear Msn2 signal over time.

Our light sweep experiments systematically probed how changes to the DNA binding affinity of Msn2 affected promoter decoding of its nuclear localization dynamics. Changing Msn2 affinity had a much stronger effect on low sensitivity genes than high sensitivity genes, but in general, increasing Msn2 affinity increased the expression of its target genes, making them more responsive to shorter, weaker, and pulsatile doses of nuclear Msn2. In fact, some promoters lost the ability to discriminate between natural stresses when Msn2 affinity was increased, which is consistent with suggestions that the ability of TFs to bind DNA is tuned for function [82], [84]. Our comparison of the SIP18 mutants showed that, in most respects, increasing the DNA binding affinity of Msn2 had similar effects to increasing the DNA binding affinity of a promoter. However, the ability to respond to pulsed versus continuous doses of nuclear Msn2 was set largely by the promoter, agreeing with a previously proposed mechanism where SIP18 A4 is more responsive to short or pulsed bursts of nuclear Msn2 because it facilitates Msn2 binding and subsequent chromatin remodeling at the TATA box [8].

The increase in gene expression associated with increasing Msn2 affinity was accompanied by a decrease in expression noise. Noisy expression can be beneficial as a source of phenotypic diversity between cells but limits the information transduction capacity of genes [8]. There is a tradeoff between noise and control of Msn2 target genes: low sensitivity promoters can filter out noisy TF activity, but respond to real signals with high levels of gene expression noise, while high sensitivity promoters have low gene expression noise, but are readily induced by noisy bursts of TF activity [7]. Various strategies have been proposed for tuning signal transduction to target genes: integrating the response of multiple genes may allow cells to overcome the noisy expression of individual genes, recruiting chromatin regulators can fine-tune the information capacity of a given gene, and coordinated regulation by multiple TFs can provide additional control of gene expression [33], [85], [86]. Our results point to another potential mechanism for selectively activating genes with a single TF: concerted regulation of TF DNA-binding ability and localization dynamics. A TF capable of switching between high and low affinity binding modes as well as continuous and pulsed nuclear localization could exploit promoter dependent differences in responsiveness to both changes in TF affinity and nuclear localization dynamics. Our measurements for Msn2(T)* suggest that pulsatile doses of such a TF in its low affinity mode could robustly activate high sensitivity genes while minimizing the expression of the low sensitivity genes, while our measurements for Msn2(A)* suggest that continuous doses of the same TF in its high affinity mode could strongly activate all its target genes with decreased expression noise. Future studies are needed to determine if TFs whose localization dynamics and ability to bind DNA are both regulated by PTMs, like p53 and NF-κB, employ such strategies to coordinate stress-specific responses with less spurious activation of terminal or resource intensive genes.

Mechanistically, what drives the different behaviors of the high and low sensitivity promoters? Our gene expression model identified DNA-binding affinity as a key factor. Increasing the number of TF binding sites in a promoter generally increases its affinity for the TF and its maximum expression [77], [78]. Accordingly, no low sensitivity promoter had more than two STREs within 500 bp of its ORF, while no high sensitivity promoter had fewer than four STREs in the same region. Differences in nucleosome occupancy between high and low sensitivity promoters are also likely to drive differences in their behavior and may manifest as differences in DNA-binding affinity by restricting the ability of a TF to access its binding sites. Induction of the low sensitivity promoter SIP18 involves a slow chromatin remodeling step before initiating transcription, as do mammalian genes that require sustained NF-κB activity [7], [8], [24]. Likewise, Crz1 target promoters with low slope ratios are typified by a slow transition from an initial off state (P_0) to an intermediate off state (P_{off}) that is associated with high initial nucleosome occupancy at the promoter [14]. In this work, low sensitivity promoters had both long activation timescales and low slope ratios (Figure 5.8 and Figure 5.15) and were enriched for low predicted values of k_1 and high predicted values of K^n—all consistent with a slow transition step involving chromatin remodeling (Figure 5.7). The general inability of Msn2(T)* to activate these promoters hints that may be poor at initiating chromatin remodeling. Activation of latent enhancers in murine macrophages by NF-κB requires continuous NF-κB activity to disrupt histone-DNA interactions [25] and competition with nucleosomes has also been implicated in the activation of yeast genes by Rap1 [87]. In fact, the affinity of exposed Pho4 binding sites in the promoters of yeast phosphate response genes determines the level of phosphate starvation—and thus nuclear Pho4—needed to nucleate chromatin remodeling and activate gene expression [77]. Further studies are needed to determine if the reduced DNA-binding ability of Msn2(T)* similarly limits its ability to compete with nucleosomes and initiate chromatin remodeling events.

We also observed decay in our Msn2 nuclear localization time-courses consistent with studies showing that nuclear accumulation of Msn2 triggers its degradation in order to overcome the growth defect associated with Msn2 hyperactivity [79], [80]. An Msn2 mutant incapable of binding DNA exhibited less signal decay, agreeing with observations that Msn2 degradation following heat shock involves DNA binding and Ssn3, a component of the mediator complex [81]. Msn2 degradation was greatest for long, pulsatile light programs and the same may be true for natural stresses like glucose starvation that cause a drawn-out series of pulses of nuclear Msn2. Similarly, Msn2 degradation caused the expression of low sensitivity genes to plateau for long duration light programs as nuclear Msn2 levels fell below the amplitude threshold needed for activation. Similar behavior in response to natural stress may cause transient activation of low sensitivity genes and sustained activation of high sensitivity genes. Our measurements revealed that Msn2 degradation began about 14 min after it first entered the nucleus—similar optogenetic approaches could prove useful in future efforts to study the dynamics of such processes.

Lastly, Msn2 has a paralog, Msn4, that arose through whole genome duplication (WGD). Msn2 and Msn4 are both regulated by PKA, exhibit similar pulsatile dynamics, and bind STREs, though Msn2 expression is constitutive, while Msn4 expression is induced by Msn2. Various studies have explored why both TFs been maintained for ~100 million years since the WGD event [30], [35], [88]. It has been proposed that asynchronous nuclear localization of Msn2 and Msn4 in response to natural stresses can enhance the expression of their shared targets [30]. Conversely, a study using chemical modulation of PKA activity found that strong induction of SIP18 and TKL2 requires both Msn2 and Msn4 [35]. While we deleted Msn4 to avoid its confounding effects on gene expression, our results suggest that having both paralogs present in a cell would help overcome the high amplitude thresholds of the SIP18 and TKL2 promoters. The same study found that Msn2 and Msn4 play redundant roles in activating DCS2 and SIP18 A4, but have distinct roles in activating SIP18 and TKL2, though this was contradicted by later work which argued that Msn2 and Msn2 are functionally redundant [88]. While Msn2 and Msn4 exhibit highly similar DNA binding preferences, their DBDs differ by 12 residues [88], [89]: our measurements suggest that any resulting differences in their ability to bind DNA would manifest at low sensitivity targets like SIP18 and TKL2, as was suggested for the human paralogous TFs Elk1 and Ets1 [90]. Future experiments swapping the DNA binding domains of Msn2 and Msn4 may clarify their roles.

5.5 Supplementary figures

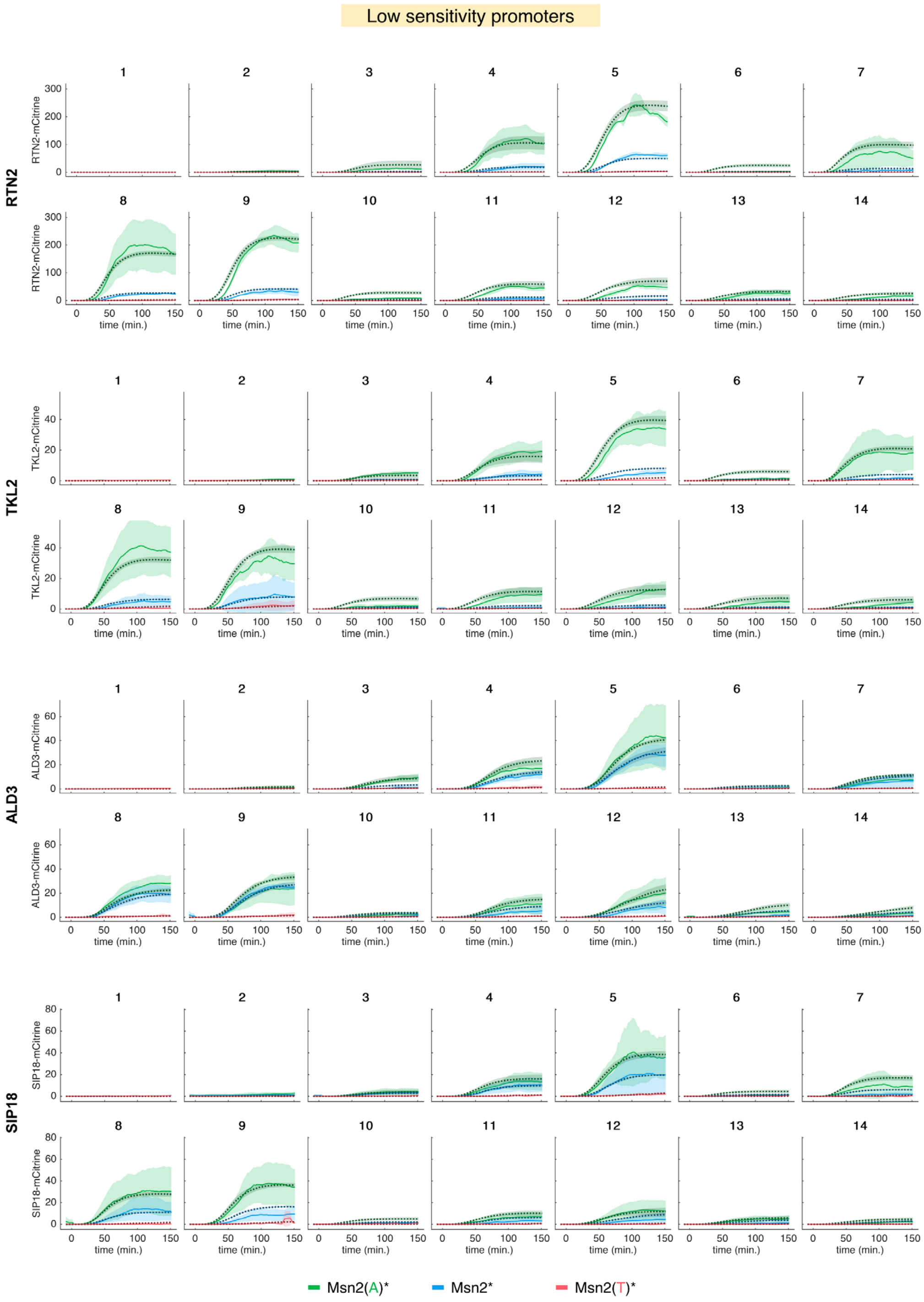

Figure 5.22 Expression measurements and model fits for low sensitivity promoters. Comparison of expression measurements and model fits for RTN2, TKL2, ALD3, and SIP18. Light solid lines and shaded regions show the mean and standard deviation of mCitrine fluorescence (AU) for at least three biological replicates. Dark dashed lines and shaded regions show the mean and 95% confidence interval of predicted mCitrine expression for the top 10 parameter sets for each reporter and Msn2 DBD mutant.

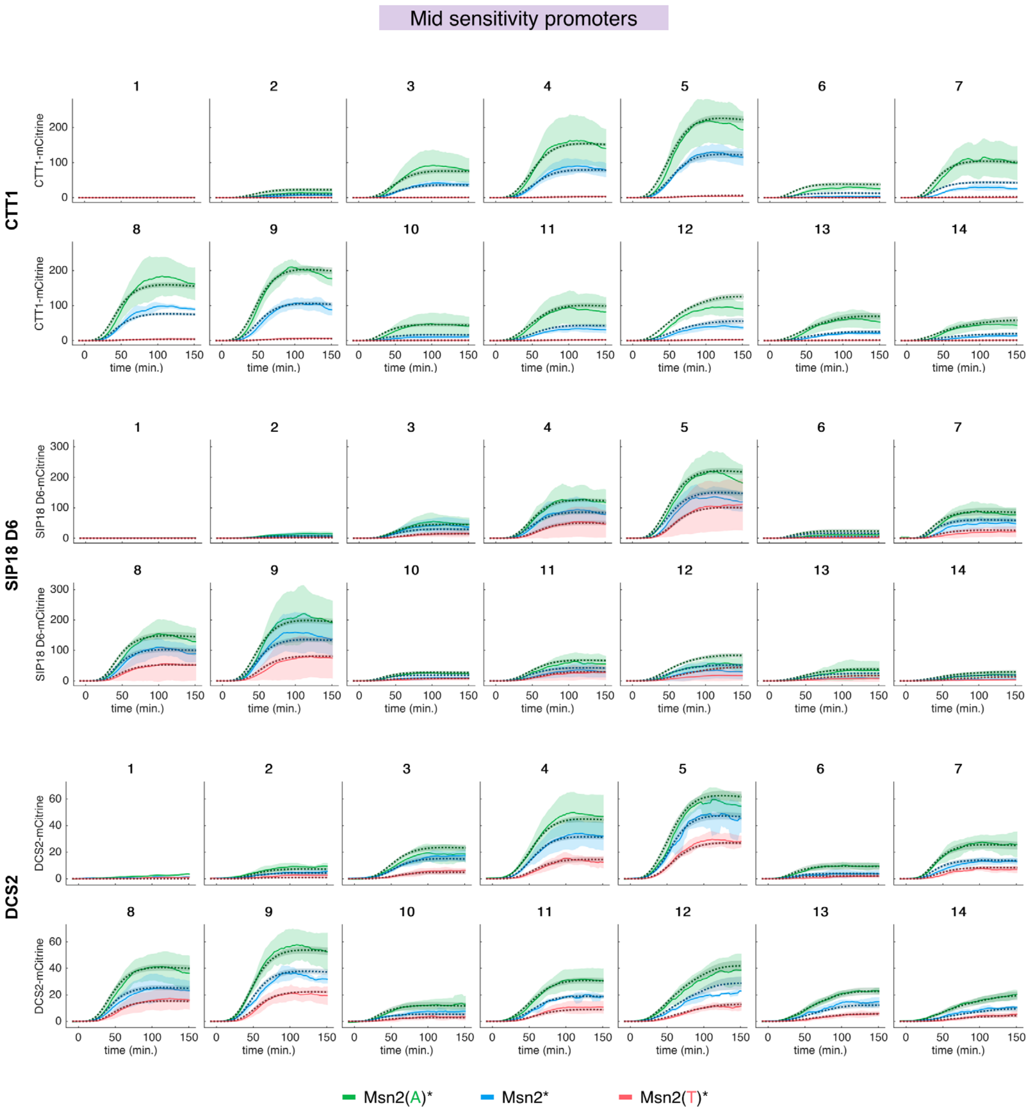

Figure 5.23 Expression measurements and model fits for mid sensitivity promoters. Comparison of expression measurements and model fits for CTT1, SIP18 D6, and DCS2. Light solid lines and shaded regions show the mean and standard deviation of mCitrine fluorescence (AU) for at least three biological replicates. Dark dashed lines and shaded regions show the mean and 95% confidence interval of predicted mCitrine expression for the top 10 parameter sets for each reporter and Msn2 DBD mutant.

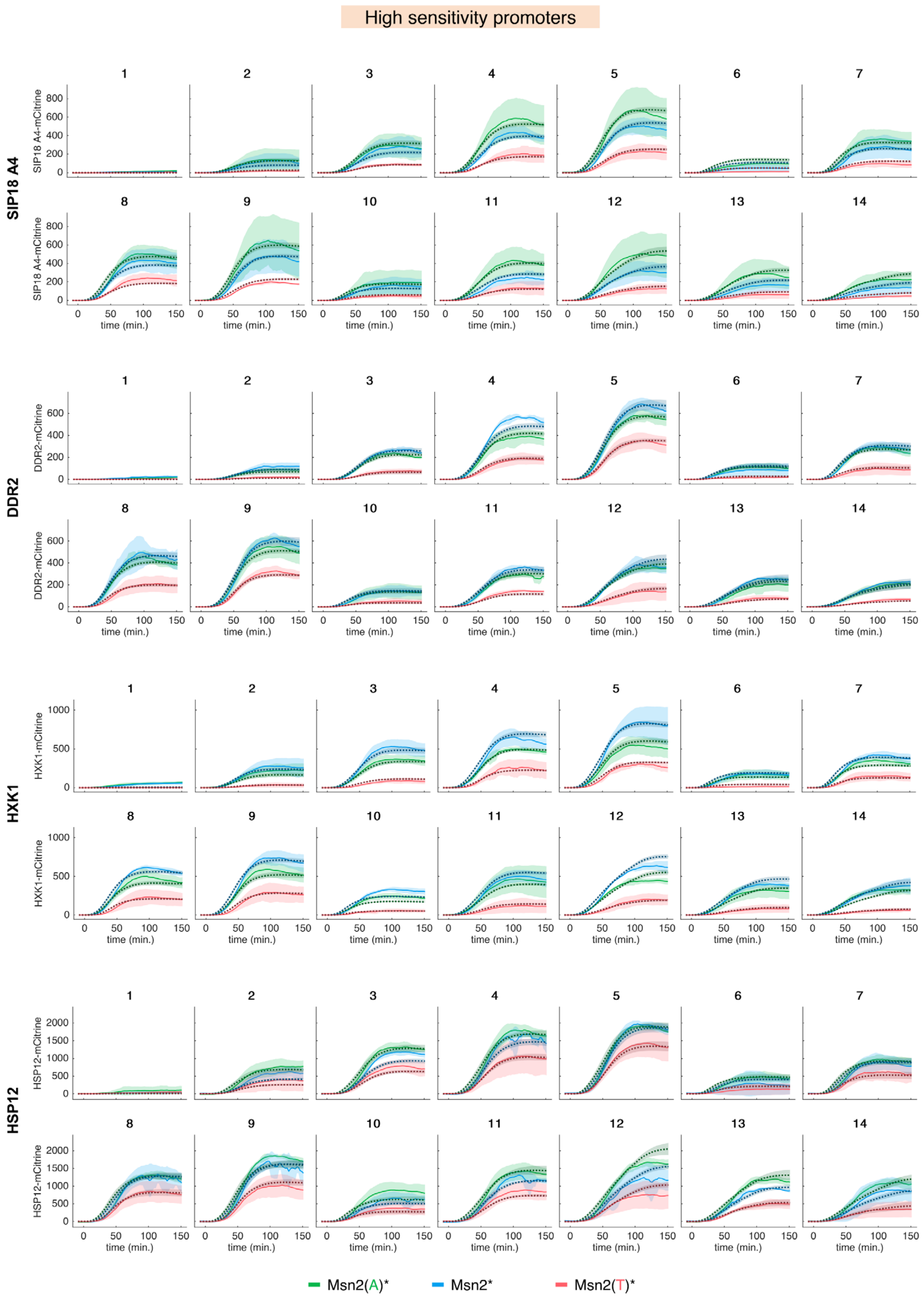

Figure 5.24 Expression measurements and model fits for high sensitivity promoters. Comparison of expression measurements and model fits for SIP18 A4, DDR2, HXK1, and HSP12. Light solid lines and shaded regions show the mean and standard deviation of mCitrine fluorescence (AU) for at least three biological replicates. Dark dashed lines and shaded regions show the mean and 95% confidence interval of predicted mCitrine expression for the top 10 parameter sets for each reporter and Msn2 DBD mutant.

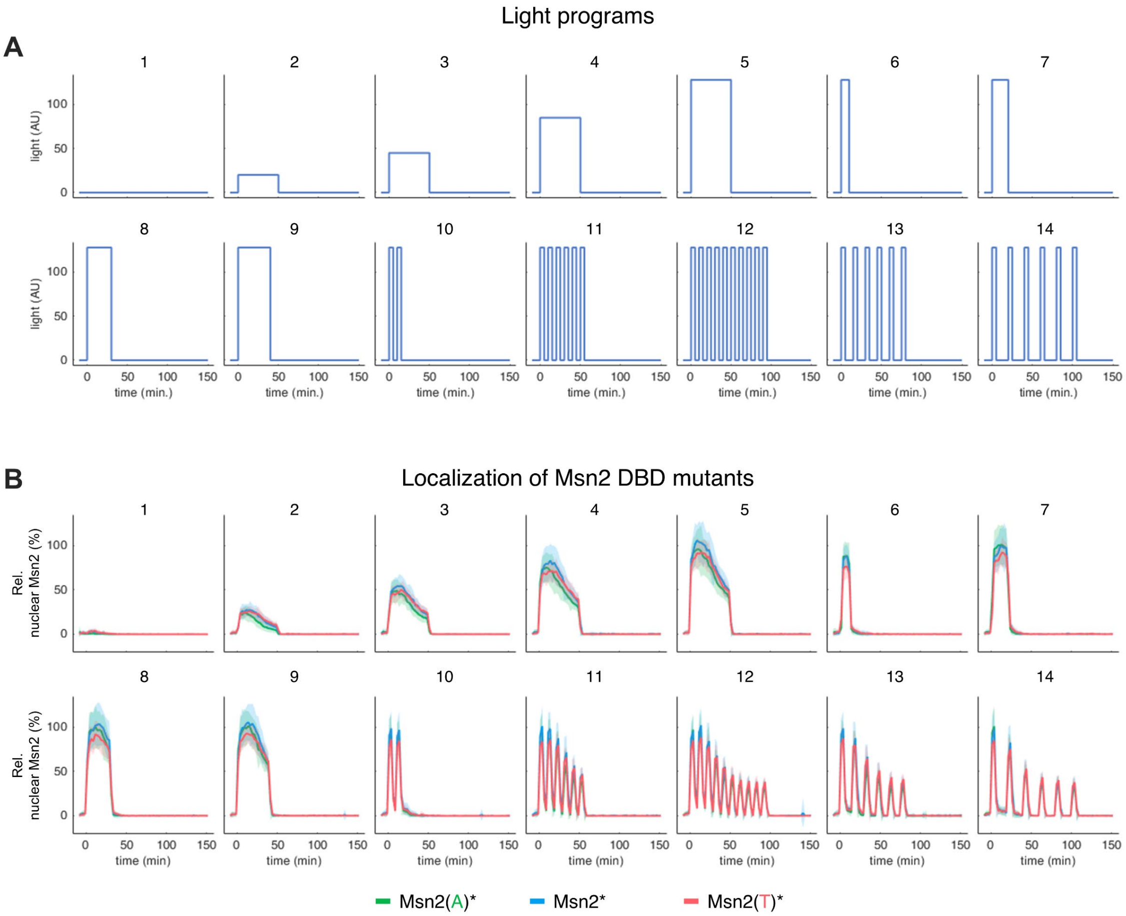

Figure 5.25 Overview of light programs and Msn2 localization timecourses. (**A**) Each light sweep experiment involved 16 light programs. Light programs 1 – 5 featured 50 min pulses of blue light with amplitudes of 0, 20, 45, 85, and 128 AU. Light programs 6 – 9 featured pulses of 128 AU blue light with durations of 10, 20, 30, and 40 min. Light programs 10 – 12 featured 2, 6, and 10 five min pulses of 128 AU blue light with interpulse durations of 5 min. Light programs 13 and 14 featured 6 five min pulses of 128 AU blue light separated by 10 and 15 min, respectively. Light programs 15 and 16 (not shown) feature full-light doses (same as light program 5) for a dCLASP control with the appropriate Msn2 mutant (see **Figure S3D**) and a batch control, respectively. All light programs included 2s off, 1 s on pulse width modulation of the light dose. (**B**) Localization timecourses for all three Msn2 DBD mutants (with CLASP) in response to the above light programs. Lines and shaded regions represent the mean and standard deviation of Msn2 localization from at least 36 light sweep experiments per mutant.

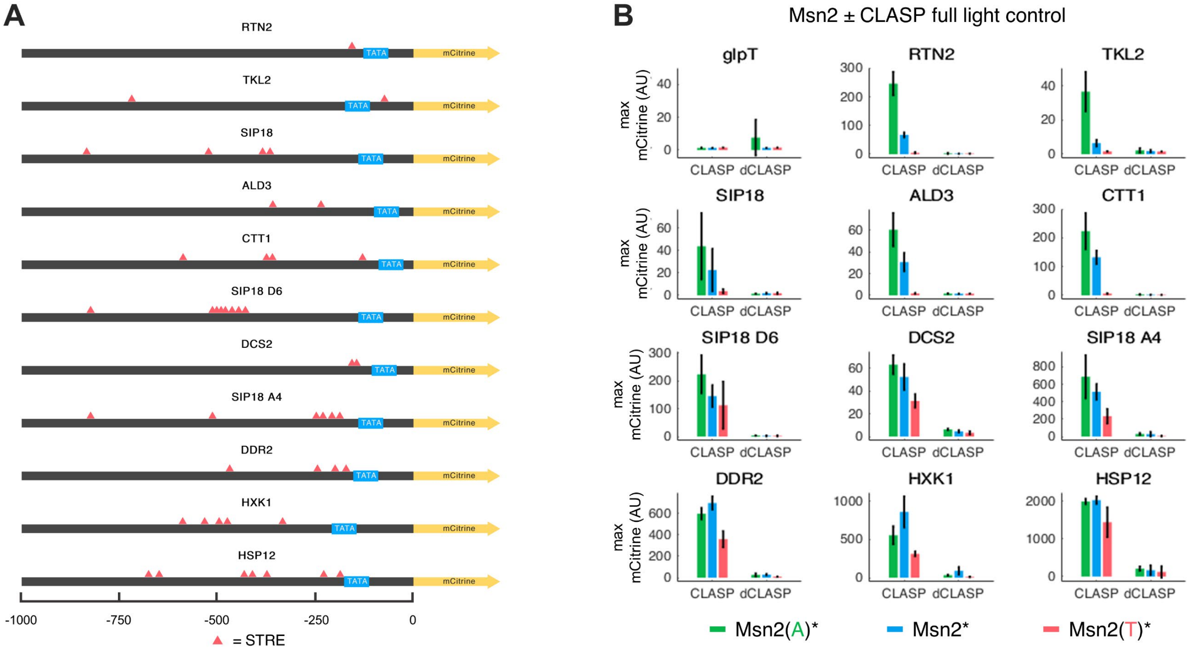

Figure 5.26 Light sweep experiment reporters and controls. (**A**) Schematic depictions of Msn2 target promoters showing the location of the TATA box and each Msn2 binding site (STRE), which has the sequence AGGGG. (**B**) Maximum promoter expression in full light for each Msn2 DBD mutant with either CLASP (light program 5) or dCLASP (light program 15) show that light-induced gene expression is due to optogenetic control of each Msn2 DBD mutant via CLASP. Bars and error bars represent the mean and standard deviation of expression for at least three biological replicates.

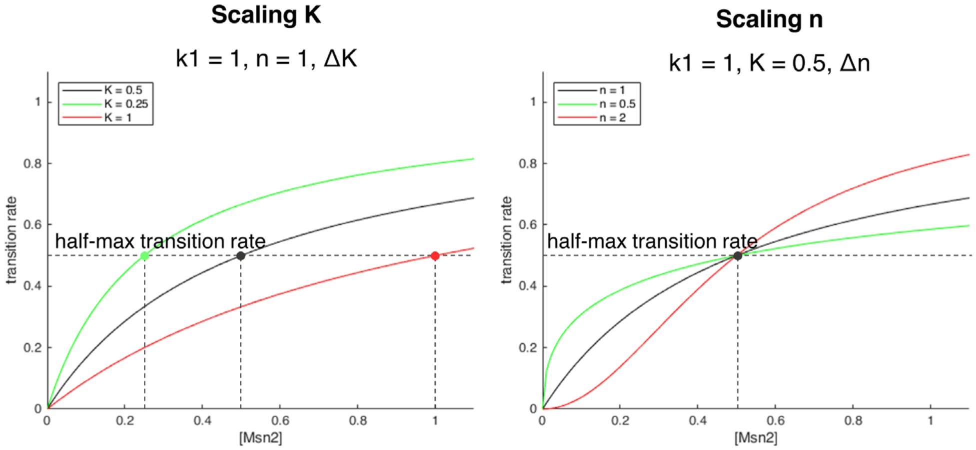

$$\text{transition rate} = \frac{k_1 Msn2(t)^n}{K^n + Msn2(t)^n}$$

Figure 5.27 Scaling K and n in gene expression model. K^n captures both the half-maximum point and slope of the curve relating nuclear Msn2 concentration to the rate at which the promoter transitions from P_{off} to P_{on}. He we depict of how individually scaling the K and n terms in the gene expression model affects the rate of promoter transition (from P_0 to P_{off}), which we take to represent chromatin remodeling at the promoter.

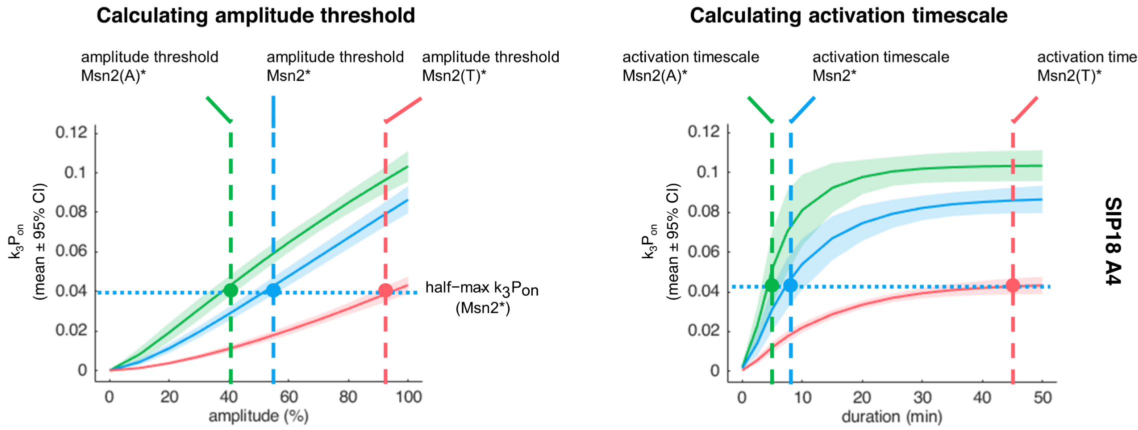

Figure 5.28 Calculating amplitude and duration thresholds. Schematic depicting the calculation of amplitude thresholds and activation timescales for each Msn2 DBD. We used the gene expression model to calculate the maximum level of k_3P_{on} achieved in response to ideal pulses of nuclear Msn2* varying in either amplitude or duration. We calculated an amplitude threshold and activation timescale for Msn2* (dashed blue lines) respectively describing the amplitude and duration of nuclear Msn2* needed to reach the half the maximum level of k_3P_{on} attained in response to a 50 min 100% amplitude pulse of nuclear Msn2* (dotted blue lines). We then calculated amplitude thresholds and activation timescales for Msn2(A)* and Msn2(T)* that respectively describe the amplitude and duration of nuclear Msn2(A*) (dashed green line) and nuclear Msn2(T)* (dashed red line) needed to attain the half-maximum level of k_3P_{on} of Msn2* (dotted blue line). Solid lines and shaded regions represent the mean and 95% confidence interval of predicted k_3P_{on} for the top 10 parameter sets of SIP18 A4. We calculated these thresholds based on k_3P_{on} rather than P_{on} because P_{on} varied substantially between parameter sets, as the rate of mRNA production (k_3) was allowed to vary widely when parameterizing the model. Scaling P_{on} by k_3 produced a measure of promoter activation (k_3P_{on}) with drastically reduced variation. The model overestimated expression for short pulses of Msn2(A)* for RTN2 and TKL2. Accordingly, levels of k_3P_{on} for RTN2 and TKL2 were forced to zero for pulses of Msn2(A)* less than or equal to 10 min when calculating their relative activation timescales.

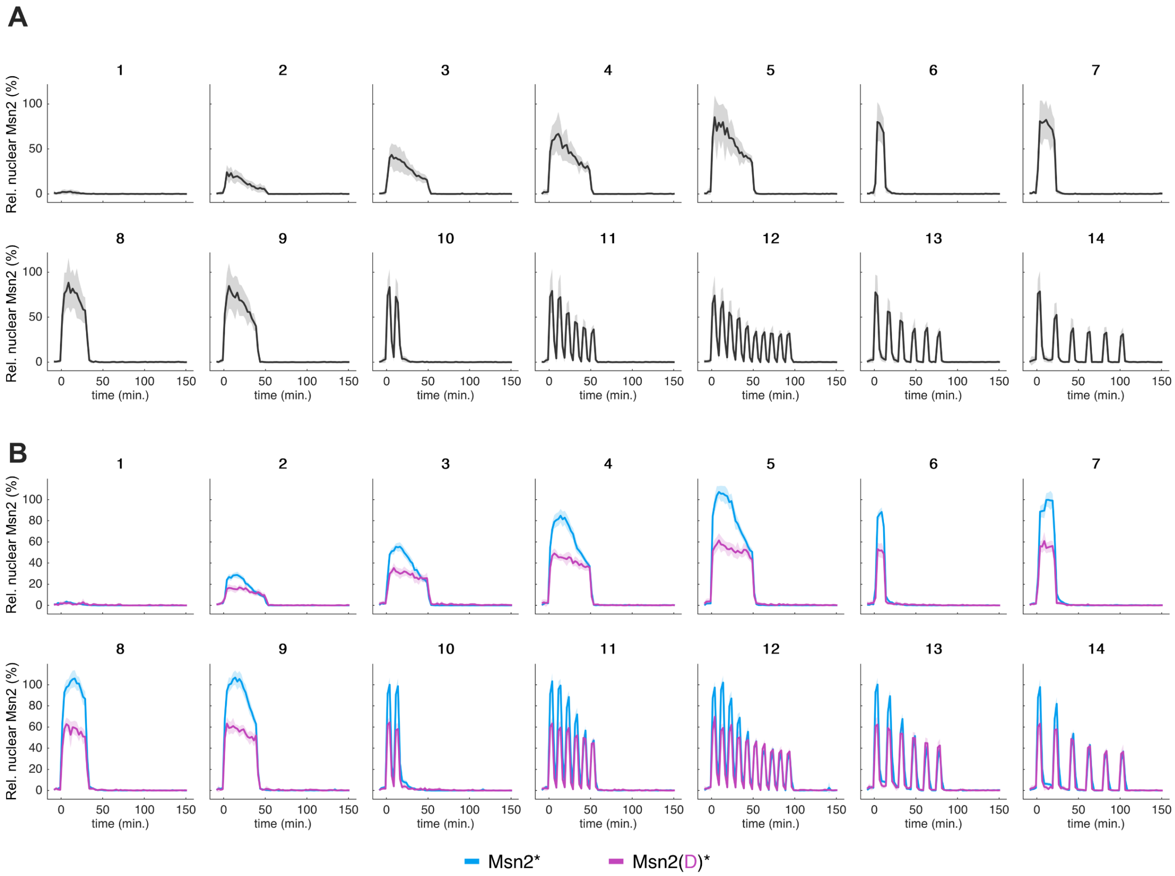

Figure 5.29 Addition Msn2 degradation timecourses. (**A**) Light sweep experiment in which every frame was taken at a different position indicates that decay in Msn2 localization time-coureses is not due to photobleaching. Lines and shaded regions represent mean and standard deviation of pooled localization measurements for three biological replicates each of Msn2*-CLASP and Msn2(A)*-CLASP. Experiments were performed in a no reporter control strain (glpT) to avoid mCitrine crosstalk into mScarlet channel. (**B**) Light sweep experiment for Msn2(D)*-CLASP, which features an S686D mutation in Msn2 that inhibits DNA-binding [55]. Lines and shaded regions represent mean and standard deviation of Msn2(D)* localization from 12 experiments representing 3 biological replicates each for 4 reporter strains. Msn2* localization acquired in separate experiments (see Figure 5.25B) is plotted for comparison.

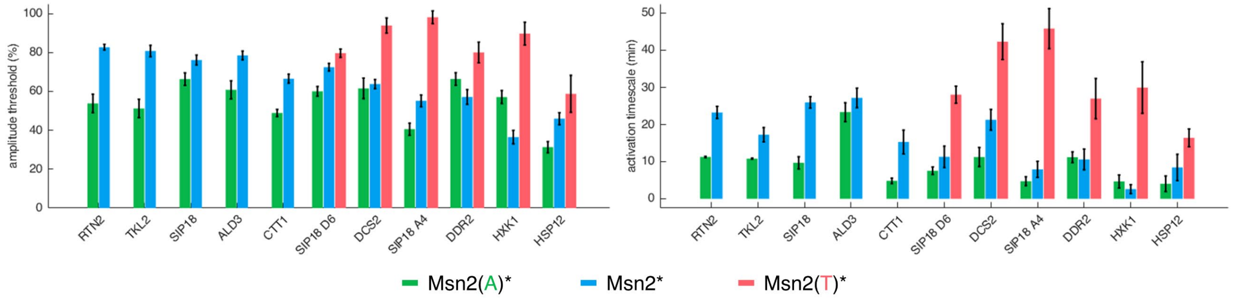

Figure 5.30 Amplitude thresholds and activation timescales for all Msn2 DBD mutants. Amplitude thresholds and activation timescales were calculated as described previously (see Figure 5.28). Bars and error bars show the mean and 96% confidence interval of amplitude and duration threshold for the top 10 parameter sets for each promoter and Msn2 DBD mutant. No thresholds are reported for Msn2(T)* where it unable to activate a given promoter in most cells.

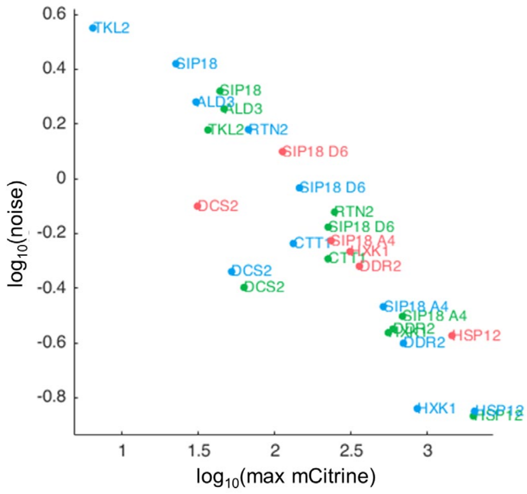

Figure 5.31 Expression versus noise. Noise (σ^2/μ^2) versus maximum expression (AU) following a 50 min 100% amplitude pulse of each Msn2 DBD mutant. Each point represents the mean of three biological replicates. Noise was calculated for each replicate as the mean noise level for times greater than 120 min.

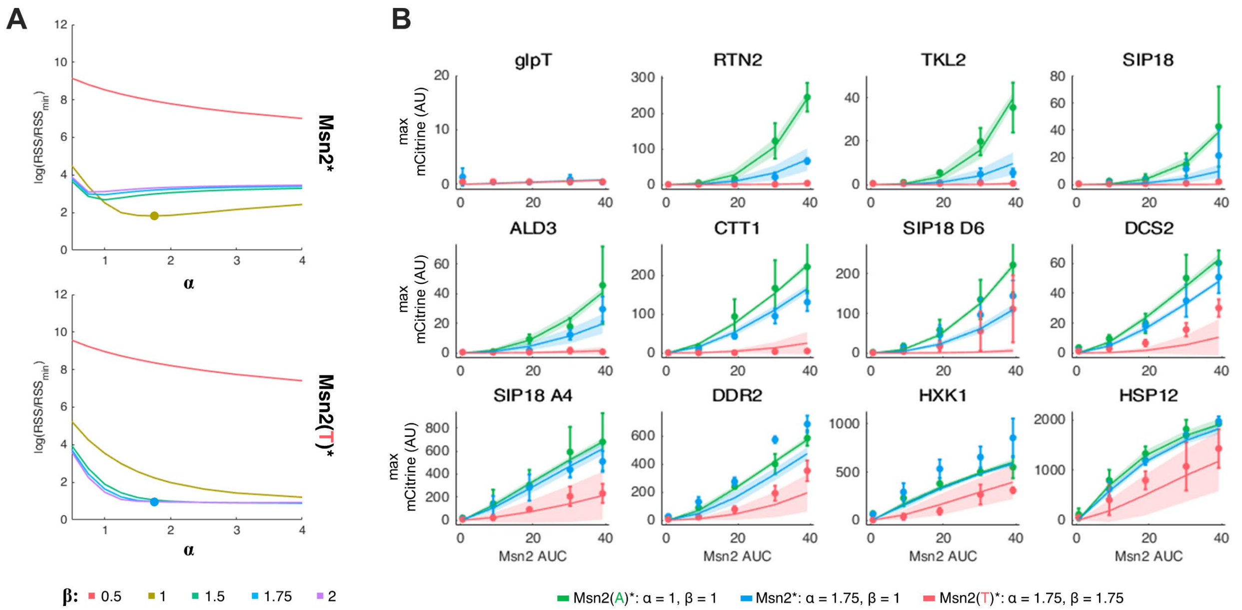

Figure 5.32 Modeling binding differences between Msn2 mutants (additional details). (**A**) Calculating scaling factors α and β to represent differences in binding affinity between the Msn2 DBD mutants. We repeatedly simulated gene expression using the top 10 parameter sets for each reporter and Msn2(A)* while scaling α and β to minimize the error between the predicted expression and the measured expression for Msn2* or Msn2(T)* across all reporters and light programs. Error was quantified for each promoter, parameter set, and pair of α and β values as the residual sum of squares error across all light programs (RSS) divided by the overall minimum RSS of each promoter (RSS_{min}). Lines show mean of normalized error (RSS/RSS_{min}) across all promoters versus α for each value of β (different colors). Based on the calculations we chose scaling values of α =1 and β = 1 for Msn2(A)*, α =1.75 and β = 1 for Msn2*, and α =1 and β = 1 for Msn2(T)* to represent differences in binding affinity between the Msn2 DBD mutants. (**B**) Comparison of measured and predicted expression using the top 10 parameter sets for Msn2(A)* for each promoter and the chosen values of α and β. Points and error bars represent mean and standard deviation of measured expression for three biological replicates. Lines and shaded regions represent the mean and 95% confidence interval of predicted expression.

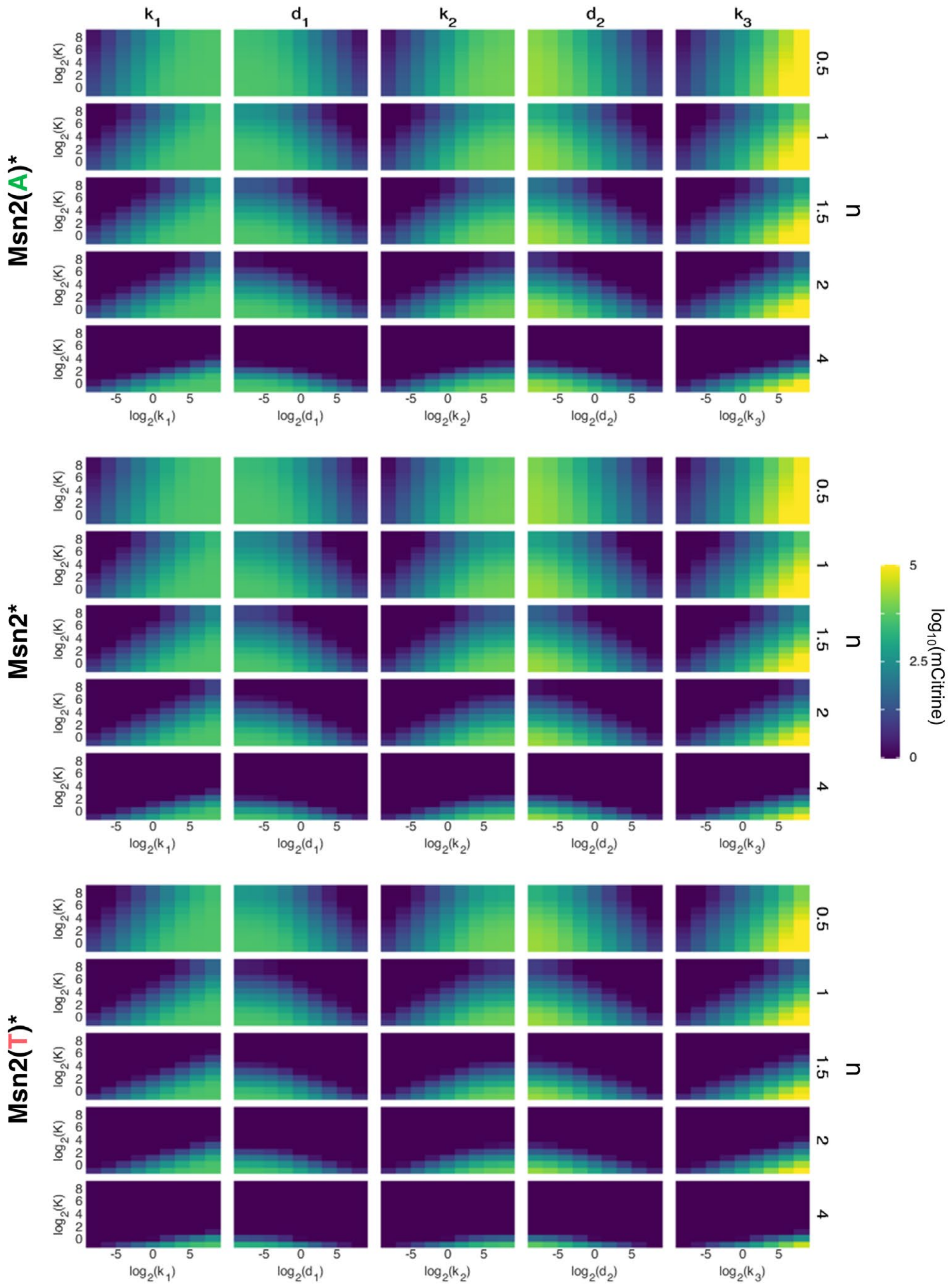

Figure 5.33 Predicted maximum expression of selected hypothetical promoters. Maximum predicted expression of hypothetical promoters in response to a 50 min 100% amplitude ideal pulse of nuclear Msn2(A)*, Msn2*, or Msn2(T)*. At a given value of K or n, each kinetic parameter (k_1, d_1, k_2, d_2, or k_3) was individually varied from $4^{-4} – 4^4$ while all other kinetic parameters were fixed at a value of one. K was allowed to vary from $2^0 – 2^8$ and n was set to 0.5, 1, 1.5, 2, or 4. All values were predicted using the three-state promoter model depicted in Figure 5.18 and the values $\alpha = 1$ and $\beta = 1$ for Msn2(A)*, $\alpha = 1.75$ and $\beta = 1$ for Msn2*, $\alpha = 1.75$ and $\beta = 1.75$ for Msn2(T)*

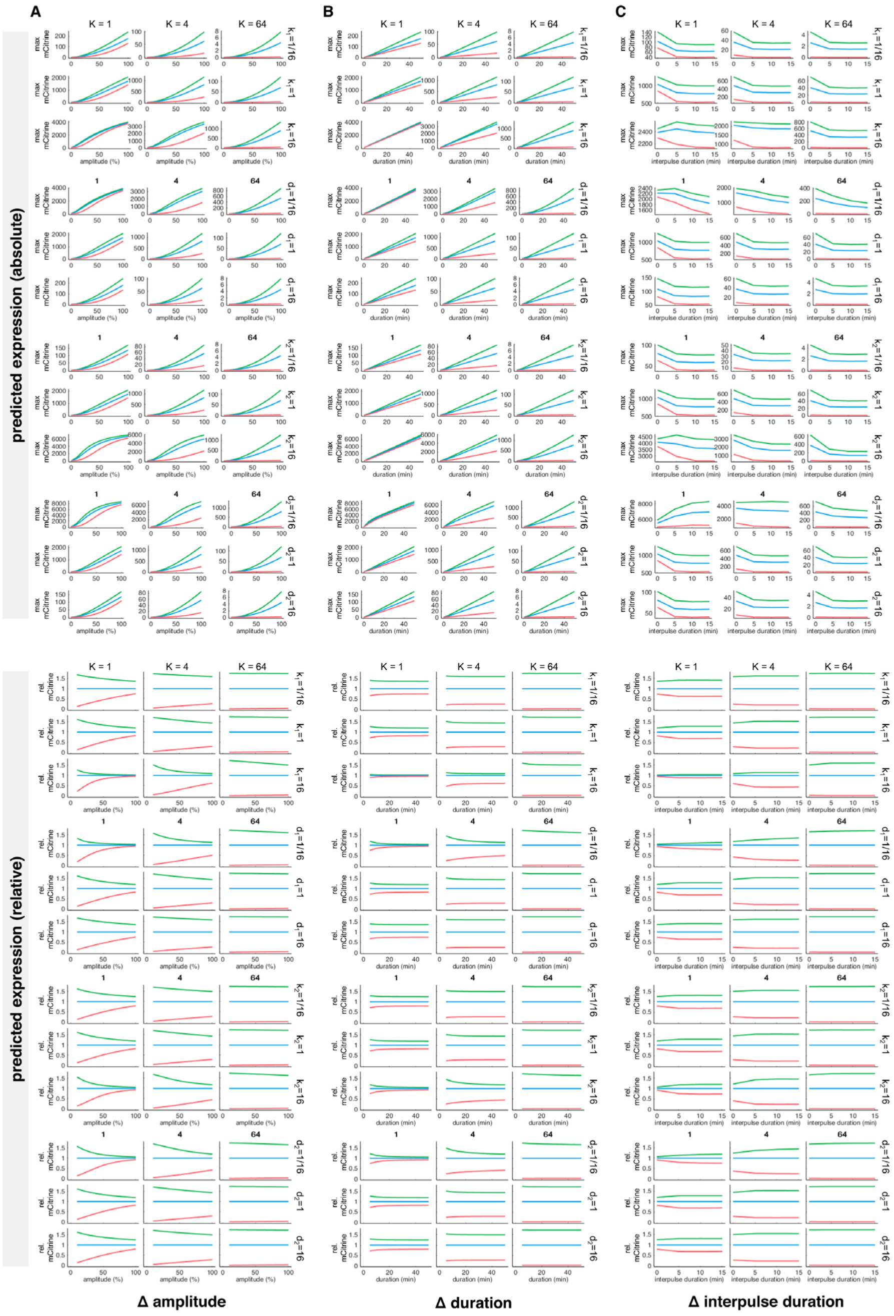

Figure 5.34 Predicted expression of hypothetical promoters versus nuclear localization. Predicted expression of selected hypothetical promoters in response to (**A**) a 50 min pulse of each Msn2 DBD mutant with amplitudes ranging from 0 – 100% (**B**) 100% amplitude pulses of each Msn2 DBD mutant with durations ranging from 0 – 50 min, and (**C**) six 5 min 100% amplitude pulses of each Msn2 DBD mutant interpulse durations ranging from 0 – 15 min. Top set of plots shows maximum expression of each hypothetical promoter, while bottom set of plots shows maximum promoter expression for each Msn2 DBD mutant normalized to maximum for Msn2*. In each 3 x 3 grid of plots, promoter affinity and given kinetic parameter were allowed to vary while all other kinetic parameters were fixed at one. For all plots, n = 1. All values were predicted using the three-state promoter model depicted in Figure 5.18 and the values α = 1 and β = 1 for Msn2(A)*, α = 1.75 and β = 1 for Msn2*, α = 1.75 and β = 1.75 for Msn2(T)*.

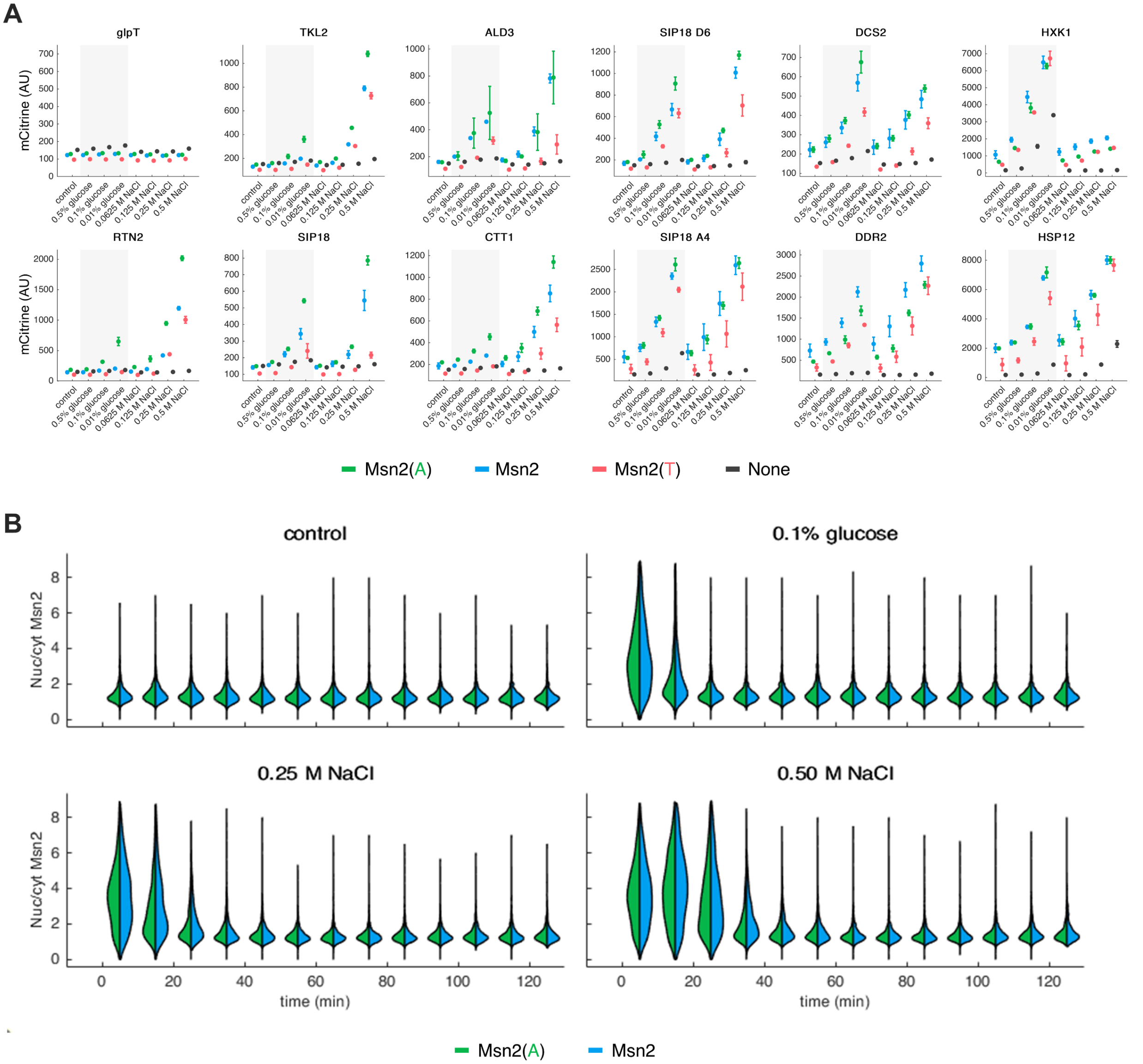

Figure 5.35 Reporter expression and Msn2 localization for glucose starvation and salt shock. (**A**) Fluorescent reporter expression following 2 hours of glucose starvation or hyperosmotic shock. All Msn2 mutants were expressed in the dCLASP system and had no mutations outside the DBD. Points and error bars represent the mean and standard deviation of fluorescence for at least three biological replicates. (**B**) Fluorescence microscopy measurements of nuclear/cytoplasmic localization for Msn2 and Msn2(A) following glucose starvation or hyperosmotic shock. Each violin plot represents single-cell localization measurements over a 12.5 min time window for three biological replicates of each Msn2 mutant. Msn2 mutants used here were in the dCLASP system and had no mutations outside the DBD

Chapter 6: Conclusions and future directions

6.1 Introduction

This thesis examined promoter decoding of TF localization dynamics and how decoding is affected by changes in the ability of the TF to bind DNA. To investigate the signal decoding of behaviors of promoters, we sought to generate defined patterns of Msn2 localization with light and measure downstream changes in gene expression. However, to do this, we first had to develop and refine methods for performing optogenetic experiments. Quantitative optogenetic experiments require the reliable delivery of precise light doses to cells under study, yet most light arrays used for optogenetic stimulation use inexpensive, off-the-shelf LEDs whose brightnesses vary considerably. In Chapter 3, we addressed this issue by developing a simple method for calibrating an LPA and, in Chapter 4, extended this method to enable the rapid calibration of an optoPlate using an automated microscope stage. In both cases, we demonstrated the ability to consistently deliver precise, targeted light doses.

These methods—and others highlighted in the Appendix—enabled us to perform the light sweep experiments of Chapter 5, where we systematically dissected how promoters respond to the nuclear localization dynamics of Msn2 and changes to its ability to bind DNA. In Section 5.3.2, we showed that the signal decoding behavior of Msn2 target promoters previously reported in response to PKA modulation persists when Msn2 localization is controlled directly with light. Using a gene expression model, we identified high, mid, and low sensitivity promoters and predicted that the effects of changing the DNA binding ability of Msn2 would be highly promoter dependent (Sections 5.3.3 and 5.3.5). Indeed, subsequent experiments confirmed that changing the DNA binding ability of Msn2 typically had a much stronger effect on low sensitivity promoters than high sensitivity promoters—though in general, increasing Msn2 affinity increased the expression of its target genes, making them less noisy and more responsive to shorter, weaker, and pulsatile doses of nuclear Msn2 (Sections 5.3.5 – 5.3.7). A sensitivity analysis of our gene expression model revealed that a low sensitivity to Msn2 (high K^n), slow activation kinetics, fast deactivation kinetics, or low amplitude doses of nuclear localization may cause a promoter to exhibit divergent responses to Msn2 mutants with different DNA binding abilities (Section 5.3.8). Subsequent experiments showed that changing the ability of Msn2 to bind DNA disrupted the ability of some target promoters to discriminate between natural stresses (5.3.9). Lastly, we found that the nuclear localization of Msn2 triggers its degradation, which caused the expression of some low sensitivity promoters to plateau for doses of nuclear Msn2 longer than 30 min (Sections 5.3.4 and 5.3.5). Collectively, our results contribute to understanding how promoters decode TF localization dynamics and point to strategies by which cells, or biomedical engineers, may control both TF localization dynamics and DNA binding affinity to enact specific gene expression programs.

6.2 Promoter decoding of Msn2 localization dynamics

In Section 5.2.3, we showed that the signal decoding behavior of Msn2 target promoters previously reported in response to PKA modulation persists when Msn2 localization is controlled directly with light. The promoters acted as filters of Msn2 localization dynamics: low sensitivity promoters filtered out low amplitude, short duration, and pulsatile doses of nuclear Msn2, while high sensitivity promoters were readily induced by nuclear Msn2, effectively integrating the nuclear Msn2 signal. However, the cellular mechanisms through which this occurs require further study. In particular, how does chromatin remodeling affect the decoding behaviors of promoters? Unlike the microfluidic devices used in previous studies of Msn2 dynamics, our optogenetic approach should allow the collection of stimulated cultures for genomic-scale measurements. For example, one could use an LPA to drive defined patterns of Msn2-CLASP localization in milliliter-scale cultures and collect samples at various timepoints to measure changes in mRNA expression or nucleosome occupancy, for example, by mRNA-seq or ATAC-seq. By leveraging the large number of Msn2 target genes (200+)—as well as existing genomic databases for *Saccharomyces cerevisiae*—it may be possible to identify common features of genes with similar decoding behaviors, such as the location of STREs or nucleosomes within their promoters or the presence of other regulators. Time-resolved mRNA measurements could then be used to refine our gene expression models by estimating promoter activity from immediately downstream mRNA levels rather than measurements of fluorescent reporters, which are further downstream and relatively slow to mature.

While direct optogenetic control of Msn2 isolates its contribution to gene expression, it is also divorced from the physiologically-relevant consequences of upstream signaling. We found few cases where our reporters were more strongly induced by pulsatile doses of nuclear Msn2 than continuous doses, yet Petrenko and colleagues reported that the secondary, pulsatile phase of Msn2 localization following glucose starvation induced stronger reporter expression than the initial, continuous phase [17] and Gutin and colleagues found that effective late stage activation of Msn2 target genes is Mck1 dependent [91]. These observations suggest that the ability of nuclear Msn2 to activate gene expression may vary over time due to the activity of other factors. Future studies may explore the contribution of these factors or identify time windows post-stimulation where the nuclear localization of Msn2 is most effective by combining optogenetic control of Msn2*-CLASP (or a more refined Msn2-CLASP mutant whose localization is completely disconnected from upstream regulation) with PKA inhibition, natural stresses, or gene knockouts. Aside from Mck1, other candidate knock-outs include the transcriptional repressors Sok2 and Sko1: under normal growth conditions, PKA activity suppresses the expression of HSP12 via Sok2 and Sko1, while Hog1 activity following hyperosmotic shock relieves repression by these factors [34].

Various studies have explored the role of Msn2’s paralog Msn4 and why it has been maintained for ~100 million years since its genesis in a whole genome duplication event [30], [35], [88], [92].

There are conflicting reports about the distinct roles of both paralogs: Chapal and colleagues found that Msn2 and Msn4 are functionally redundant when expressed under the same promoter [88], whereas AkhavanAghadam and colleagues reported that Msn2 and Msn4 play redundant roles in activating the high sensitivity genes DCS2 and SIP18 A4, but have distinct roles in activating the low sensitivity genes SIP18 and TKL2 [35]. While Msn2 and Msn4 have similar DBDs and exhibit highly similar DNA binding preferences [88], [89], our results suggest that any differences between them would manifest at low sensitivity genes. Future light sweep experiments comparing Msn2*-CLASP to a Msn2-CLASP mutant with an Msn4 DBD could resolve if such differences exist.

6.3 The role of DNA binding affinity in promoter decoding of TF localization dynamics

In Sections 5.3.5 – 5.3.7, we showed that increasing the DNA binding ability of Msn2 increased the expression of its target genes, making them less noisy and more responsive to shorter, weaker, and pulsatile doses of nuclear Msn2. Our comparison of the SIP18 mutants revealed that, in most respects, increasing the DNA binding affinity of Msn2 had similar effects to increasing the DNA binding affinity of a promoter. However, the relative ability to respond to pulsed versus continuous doses of nuclear Msn2 was set largely by the promoter, which is consistent with the previously proposed mechanism that SIP18 A4 is more responsive to short or pulsed bursts of nuclear Msn2 because it facilitates Msn2 binding and subsequent chromatin remodeling at the TATA box [8]. Overall, as predicted by our gene expression model, changes to the DNA binding ability of Msn2 generally had a stronger effect on the expression of low sensitivity genes than high sensitivity genes. In particular, the low affinity Msn2(T)* mutant failed to activate the low sensitivity genes in most cells, even for long, high amplitude doses of nuclear localization. Measurements of nucleosome occupancy like those proposed in Section 6.2 could thus reveal if decreasing the DNA binding ability of a TF decreases its capacity to initiate chromatin remodeling events. This may prove relevant for mammalian TFs such as p53 and NF-κB, whose nuclear localization dynamics and ability to bind DNA are both regulated by PTMs. Our results indicate that a TF capable of switching between high and low affinity binding modes as well as continuous and pulsed nuclear localization could exploit promoter dependent differences in responsiveness to such changes: our measurements for Msn2(T)* suggest that pulsatile doses of such a TF in its low affinity mode could robustly activate high sensitivity genes while minimizing the expression of the low sensitivity genes, while our measurements for Msn2(A)* suggest that continuous doses of the same TF in its high affinity mode could strongly activate all its target genes with decreased expression noise. Future studies of p53 and NF-κB may reveal if this occurs.

6.4 Localization triggered degradation of Msn2

Over the course of many light sweep experiments, we observed decay in the Msn2 nuclear localization timecourses consistent with previous reports that the nuclear accumulation of Msn2 triggers its degradation (see Section 5.3.4) [79], [80]. We also found that an Msn2 mutant incapable of binding DNA exhibited less signal decay, which agrees with observations that Msn2 degradation following heat shock involves DNA binding and Ssn3, a component of the mediator complex. This means that mediator both promotes the expression of Msn2 target genes and facilitates the degradation of Msn2—possibly demonstrating the so-called “black widow” model of transcriptional regulation [93]. The precise control of Msn2 localization afforded by our optogenetic approach revealed that degradation of Msn2 began about 14 min after it first entered the nucleus and continued while Msn2 was outside the nucleus. We also observed the consequences of degradation: expression of the low sensitivity promoters generally plateaued for pulses of nuclear localization longer than 30 min, demonstrating how degradation may act as a timer on the expression of some genes.

While widely documented in other contexts, degradation of Msn2 was not reported in earlier studies that used PKA inhibition to study the relationship between Msn2 localization dynamics and downstream gene expression. This may be due to differences in how we acquired and analyzed our measurements or it may be that Msn2 degradation is more prominent in our CLASP-based experimental system. To maintain a set stoichiometric relationship with a plasma membrane anchor, our Msn2-CLASP constructs were expressed under the moderate strength, constitutive RPL18B promoter, rather than the weak constitutive MSN2 promoter [70]. Localization triggered degradation may therefore function to restrain Msn2 concentrations closer to their natural level; reconfiguring the CLASP system to allow Msn2 expression closer to its natural level may show if this true. Alternatively, the nuclear localization of Msn2 without PKA activity may trigger degradation as a brake on the spurious activation of target genes. This is plausible because PKA regulates the mediator complex, which is involved in Msn2 degradation. This could be investigated by measuring light induced Msn2*-CLASP localization both with and without PKA inhibition.

6.5 Potential applications of this work

Recent work has exploited optogenetic control of gene expression in the biosynthesis of chemicals like isobutanol, lactic acid, and naringenin [76], [94], [95]. However, the ability to selectively drive multiple gene expression programs with light is limited by the spectral overlap of available optogenetic tools. To address this, Benzinger and colleagues developed a synthetic gene expression demultiplexer, which exploits the varying activation kinetics of multiple light-sensitive TFs to selectively activate multiple gene expression programs using a single input signal (pulsed doses of blue light). They demonstrated that different patterns of blue light could selectively activate the expression of proteins that control metabolic flux through a heterologous beta-carotene pathway in yeast [86]. The ability to control both TF activity dynamics and DNA binding could possibly expand the number of gene expression outcomes accessible using a single input signal like light. Absent that ability, there may be additional scope for improved demultiplexing of light inputs by mutating promoters to fine-tune their response to different patterns of TF localization: for example, our measurements suggest that mutations that reduce the affinity of a promoter for a TF may reduce unwanted activation in response to pulsatile light doses.

Msn2 activity can prime cells to survive future stresses, but at the cost of reduced cell growth [96], [97]. Cell-to-cell differences in cAMP/PKA signaling and Msn2 activity have been proposed as a nongenetic source of phenotypic heterogeneity that allows clonal populations of cells to survive uncertain environments [92], [98]. Our system could be used to clarify the role of Msn2 in stress tolerance by generating precise doses of Msn2 activity before applying a stress and measuring cell survival. Such insights could have applications in biotechnology. Zhao and colleagues used an optogenetic system to enhance the biosynthesis of isobutanol in batch cultures of yeast by switching cells from an initial rapid growth phase to a stressful production phase [95]. The rapid growth phase would likely benefit from low levels of Msn2 activity, while a dose of Msn2 activity prior to the switch may prime to cells to survive longer during the stressful production phase. Our system could potentially be used to identify the strength and timing of an Msn2 dose that enhances production and minimized the detrimental effects of Msn2 on cell growth. Lastly, optogenetic gene induction systems may prove a more palatable prospect than drugs for controlling yeast cultures used to produce food or drink.

Appendix

A.1 The cellular role of Msn2

A.1.1 Msn2 is a key regulator of the stress response in yeast

Msn2 and its paralog Msn4 were first identified as a multicopy suppressors of raffinose utilization defects in *Saccharomyces cerevisiae* strains with a thermosensitive SNF1 gene [96]. Subsequent work revealed that Msn2 and Msn4 are key regulators of the yeast environmental stress response (ESR)—a common transcriptomic response to a broad range of environmental stresses—and coordinate the expression of roughly 300 stress defense genes. Accordingly, mild activation of the ESR can impart resistance to future stresses, as can overexpression of Msn2, but at the cost of reduced cellular growth [16], [33]. Single deletion mutants of msn2 or msn4 have no obvious phenotype, but msn2Δ msn4Δ double deletes are hypersensitive to environmental stresses [96], [97]. Signals from diverse environmental stresses—including glucose or nitrogen starvation, hyperosmotic shock, heat shock, and oxidative stress—converge on Msn2 via multiple upstream signaling pathways (Figure A.1.1). The cAMP/PKA pathway plays a central role in the regulation of Msn2 activity: under normal growth conditions, phosphorylation by PKA inactivates Msn2 by causing its sequestration to the cytoplasm, but in response to environmental stress, Msn2 translocates to the nucleus as repression by PKA is relieved. However, PKA activity is sufficient but not necessary for stress-responsive nuclear localization of Msn2 and other pathways contribute to the regulation of Msn2 in a stress-dependent manner.

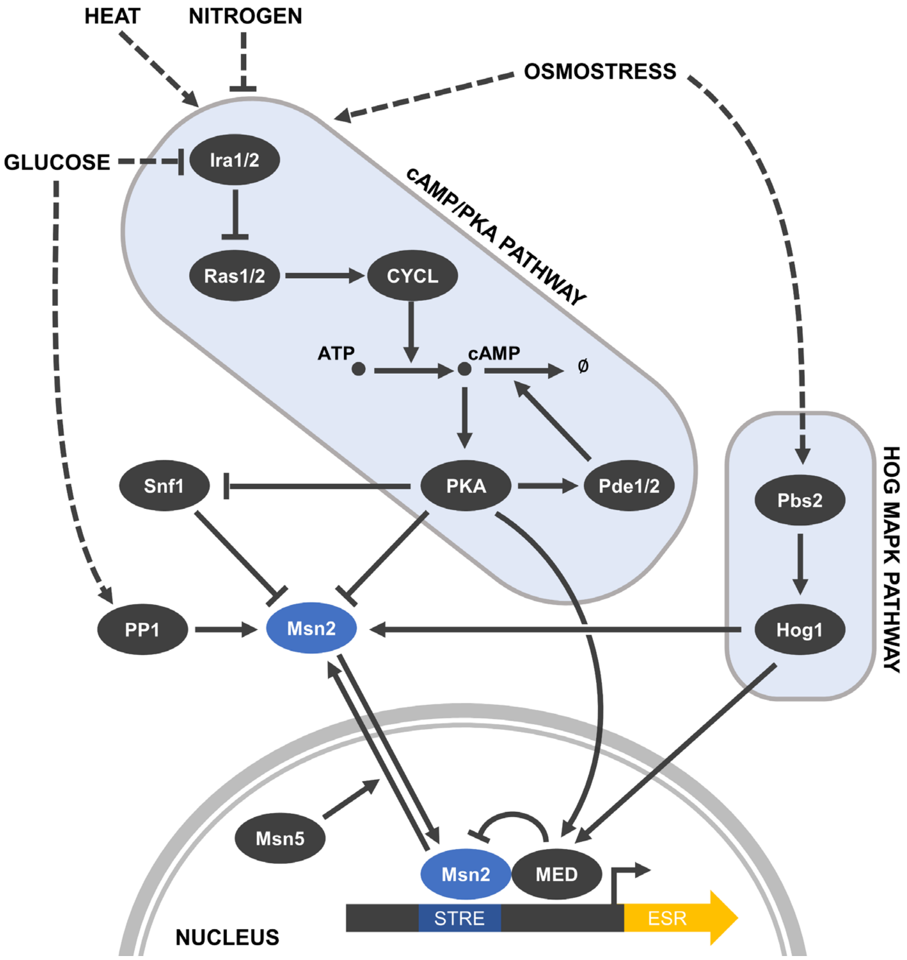

Figure A.1.1 Signaling via Msn2. Diverse environmental stresses converge on Msn2 to activate ESR genes. Here, CYCL denotes adenylyl cyclase and MED denotes the mediator complex

The cellular response to glucose starvation is primarily mediated by cAMP/PKA and is typified by an initial, coherent pulse of Msn2 nuclear localization followed by short, sporadic pulses with dose-dependent frequency [6]. However, the kinase Snf1 also plays a role in low glucose conditions—it can generate pulses of Msn2 nuclear localization in yeast strains with constitutively weak PKA activity—and protein phosphatase 1 (PP1), specifically its catalytic subunit Glc7, has been implicated in the dephosphorylation of Msn2 in response to stress [17], [99]. Hyperosmotic shock causes an initial, coherent burst of Msn2 nuclear localization with a dose-dependent duration that may be followed by a second wave of nuclear localization [6], [17]. This behavior is mediated by both the cAMP/PKA and HOG MAPK pathways: diminished PKA activity delays and weakens the initial burst, while the deletion of Hog1 (or Snf1) eliminates the second wave [17]. Nitrogen starvation also activates Msn2 via PKA, though it remains unclear how the nitrogen-responsive TOR pathway interacts with the cAMP/PKA pathway. Adding a further layer of complexity to the regulation of Msn2 target genes, signaling pathways regulating Msn2 activity have additional targets that also affect gene expression [34]. Both PKA and Hog1 regulate components of the mediator complex, which both promotes the expression of Msn2 target genes and facilitates the degradation of Msn2. Similarly, PKA activity in normal conditions suppresses the expression of an Msn2 target gene (HSP12) via the transcriptional repressors Sok2 and Sko1, while Hog1 activity following hyperosmotic shock relieves repression by these factors.

Msn2 is of particular interest as a model system for studying TF localization dynamics. Various mechanisms have been proposed to account for the dynamic, pulsing behavior of Msn2, including a negative feedback loop involving PKA-mediated decay of cAMP (via Pde1/2) and signaling pathway noise that is amplified by the small number of molecules involved [17], [100], [101]. Additional research expanded on the negative feedback model and suggested that stimulus-dependent positive feedback between PKA and Snf1 may account for differences in Msn2 dynamics between glucose starvation and hyperosmotic shock [102]. Recent work quantified the amount of information that may be encoded in Msn2 dynamics (up to 1.5 bits) or subsequently decoded by natural promoters (up to 1.3 bits), but suggested that higher fidelity signal transduction is possible by integrating the stress-specific activity of multiple TFs or the output of multiple target genes [9], [103].

A.1.2 Functional domains of Msn2

Upstream signaling pathways can control the activity of Msn2 via post-translational modifications (PTMs) of its functional domains (Figure A.1.2A), which include a transactivation domain (TAD), nuclear export signal (NES), nuclear localization signal (NLS), and zinc finger DNA binding domain (DBD) [18], [104]. The Msn2 TAD is predominantly disordered, but features two short structured motifs that are conserved in other yeast species and promote interactions with Gal11, a component of the mediator complex [105], [106]. The NLS promotes nuclear import of Msn2 via Kap121 and Kap123, while the NES promotes nuclear export via the exportin Msn5 [100], [107]. The activity of these domains is regulated by phosphorylation [55], [75]. Under normal growth conditions, PKA promotes cytoplasmic retention of Msn2 by phosphorylating key sites in its NLS (S582, S620, S625, and S633) and NES (S288 and S304). In response to stress, PKA activity is inhibited and dephosphorylation of these sites—likely by PP1—causes Msn2 to translocate to the nucleus [18], [99], [107]. Snf1 also inhibits the nuclear localization of Msn2 by phosphorylating at least one site (S582) in its NLS. The Msn2 TAD contains two potential PKA phosphosites (S194 and S201), but is reportedly insensitive to signaling via PKA [104]. This is supported by our measurements of stress induced gene expression for an Msn2 allele containing phosphomimetic mutations at these sites (Figure A.1.2B).

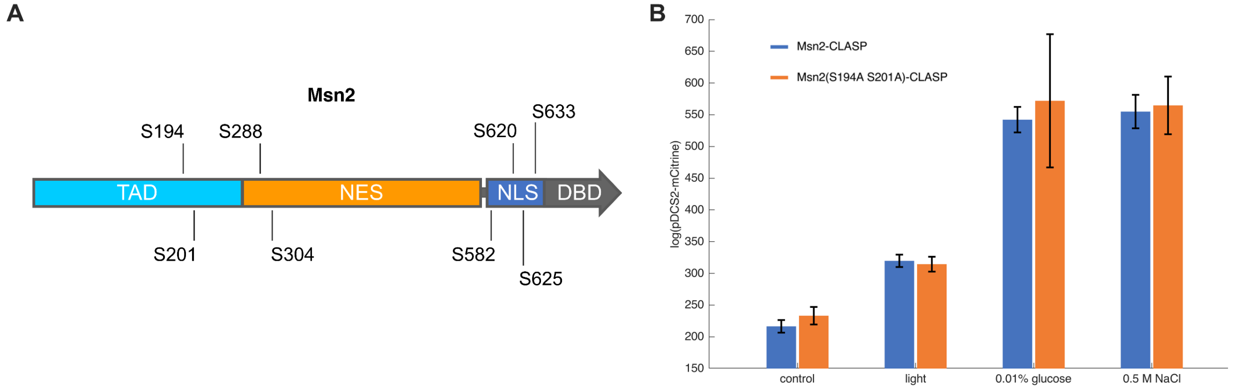

Figure A.1.2 Functional domains of Msn2. (**A**) Schematic showing relevant functional domains of Msn2—the transactivation domain (TAD), nuclear export signal (NES), nuclear localization signal (NLS), and zinc finger DNA binding domain (DBD)—and phosphosites targeted by PKA. (**B**) Expression of pDCS2-mCitrine following 50 min 155 AU blue light, glucose starvation, or hyperosmotic shock. Bars and error bars represent mean and standard deviation of fluorescence measured by flow cytometry two hours after stimulation.

A.1.3 Gene induction by Msn2

Msn2 mediates the expression of its target genes by binding stress response elements (STREs) in their promoters, which have the core consensus sequence AGGGG and function in both directions [97]. Msn2 binds STREs with limited flanking base preference and relatively low (sub-micromolar) affinity, which allows the graded activation of its target genes over a range Msn2 concentrations [54]. There are approximately 11,500 STREs in the yeast genome, roughly 3000 of which are upstream of yeast genes [108]. However, Msn2 does not bind most of these sites, especially those occluded by well-positioned nucleosomes, but can access STREs in nucleosome depleted regions or regions at the edge of nucleosomes. Once bound, Msn2 promotes nucleosome displacement by recruiting chromatin remodeling complexes like SWI/SNF and SAGA [7], [109]. Adding another layer of regulatory complexity, recent work has shown that the intrinsically disordered region (IDR) of Msn2 helps direct it to its target genes [110].

Some mechanisms appear to regulate DNA binding by Msn2, albeit indirectly. Cdc55, a regulatory subunit of protein phosphatase 2A (PP2A) prolongs Msn2 binding and RNA Pol II recruitment at Msn2 target genes, but does not directly affect the phosphorylation status of Msn2 [55]. Similarly, the STRE binding activity of Msn2 is diminished by deleting MCK1 and MDS1, which encode homologs of the mammalian glycogen synthase kinase GSK-3, though no interaction between these proteins and Msn2 has been detected [111]. Following stress, MCK1 is dispensable for induction of early responding Msn2 target genes, but is required for the subsequent induction of late responding genes [91].

It was also proposed that the DNA binding ability of Msn2 is directly regulated by phosphorylation of the S686 site within its DBD: Msn2 mutants with an S686D mutation mimicking constitutive phosphorylation fail to bind DNA or activate the expression of Msn2 target genes, while an S686A mutation mimicking constative dephosphorylation increases the expression of most target genes (Figure A.1.3) [55].

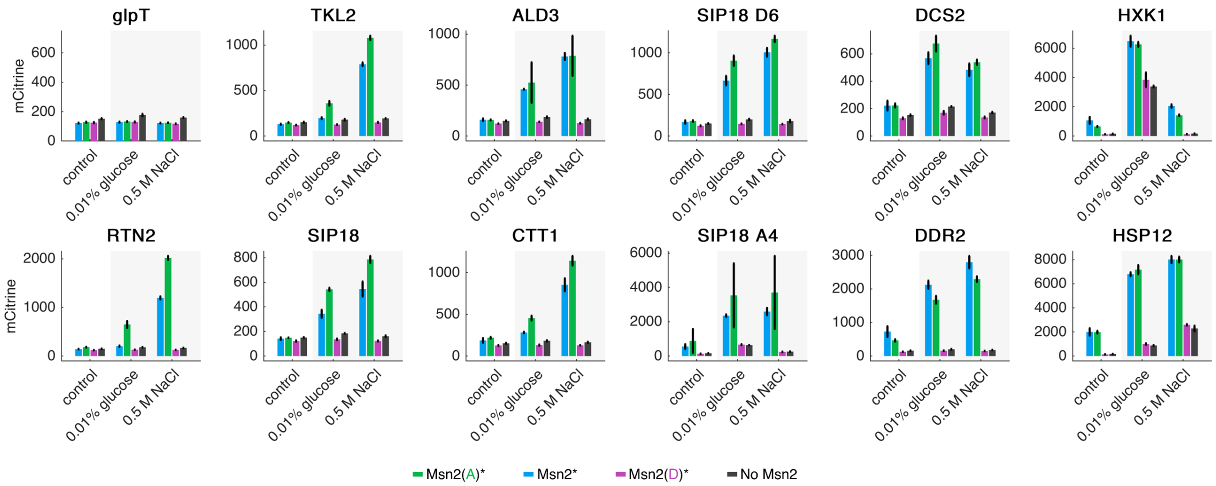

Figure A.1.3 Gene induction by Msn2(S686) mutants. Fluorescent reporter expression was measured by flow cytometry after two hours of severe glucose starvation or hyperosmotic shock. Bars and error bars represent mean and standard deviation of fluorescence for at least three biological replicates.

We investigated this possibility using the measurements from our light sweep experiments (Figure 5.12) and our computational model of gene expression (Figure 5.6). If DNA binding by Msn2 is prevented by phosphorylation of S686, then 1) Msn2* exists as some mix of active and inactive molecules and 2) Msn2(A)*, which features the S686A mutation, represents the 100% active, dephosphorylated state. Using an approach similar to that of Section 5.3.8, we reasoned that scaling the input concentration, Msn2(t), in our gene expression model for Msn2(A)* should recapitulate the expression for Msn2* across all reporters. We found that scaling the input concentration by a factor γ = 0.75 (indicated by blue circle in Figure A.1.4A) best allowed the model for Msn2(A)* to recapitulate the expression measurements for Msn2* over all light programs and reporters. This would imply that 25% of Msn2* molecules bear a phosphorylated S686 under normal growth conditions. However, scaling the input concentration of Msn2(A)* to capture the measured expression of low sensitivity promoters like RTN2 and TKL2 caused the predicted expression of high sensitivity promoters like HSP12 and HXK1 to undershoot their measured expression (Figure A.1.4B) and could not account for promoters like HXK1 where expression was consistently higher for Msn2* than Msn2(A)*. In contrast, it has been demonstrated that increasing the DNA binding affinity of a transcription factor can decrease the expression some target genes by allowing it to bind a large set of weaker, non-consensus sites throughout the genome [41].

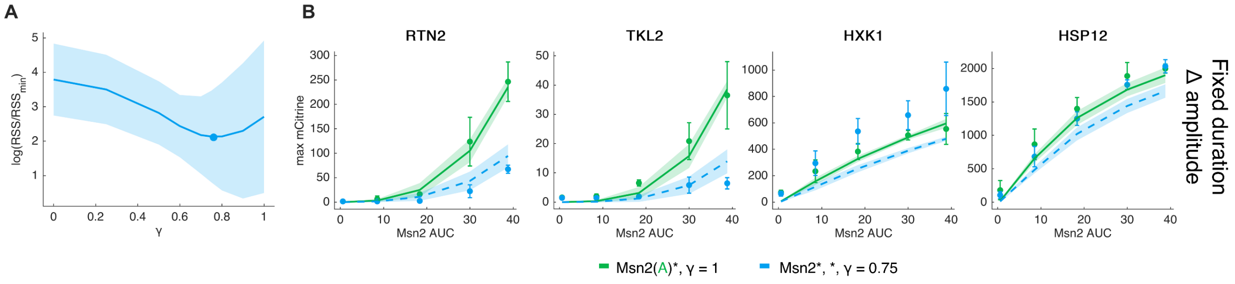

Figure A.1.4 Model exploration of possible phosphorylation of S686 in Msn2 DBD. (**A**) Using the top 10 parameter sets for each reporter and Msn2(A)*, we scaled the input concentration, Msn2(t), to find a scaling factor γ that minimized the error (RSS/RSS$_{min}$) between the predicted expression and the expression measured for Msn2* across all reporters and light programs. (**B**) Predicted versus measured expression of selected reporters in response to 50 min pulses of nuclear localization with amplitudes varying from 0 – 100%. Lines and shaded regions show mean and 95% confidence interval of expression predicted for top 10 parameter sets for Msn2(A)* with input concentration scaled by γ = 0.75. Points and error bars represent mean and standard deviation of measured expression.

We turned to the literature to further investigate if the regulation of Msn2 activity via phosphorylation of the S686 site is well supported. Potential phosphorylation of S686 was reported for cells growing on glucose with a site probability of 76.3%, just above the 75% threshold at which a phosphosite was designated as confidently localized [55]. Attempts to measure the phosphorylation state of S686 in other conditions failed and it was noted that the peptide region containing the S686 site is difficult to analyze by mass spectrometry. Further attempts to raise a phosphospecific antiserum to the site were unsuccessful and treatment of a GST-tagged Msn2 DBD with phosphatase had no obvious effect on DNA binding. An earlier study found that the ability of Msn2 to bind DNA is independent of stress, as there is no significant difference in STRE-binding ability *in vitro* between myc-tagged Msn2 extracts from stressed versus unstressed cells [18]. Taken together, our results and the literature indicate that the DNA binding ability of Msn2 is not directly regulated by phosphorylation of S686 and that an S686A mutation simply increases the ability of Msn2 to bind most target genes.

We analyzed the effects of the S686A mutation on gene expression using previously published microarray data collected from cells overexpressing either Msn2 or Msn2(6A), an allele of Msn2 that is constitutively nuclear and features the S686A mutation (Figure A.1.5) [108]. We focused on genes that were induced above a two-fold threshold: of these, 230 genes (green) were most highly expressed for Msn2(6A), while 106 genes (blue) were most highly expressed for Msn2. We then compared the flanking bases of these groups since previous *in vitro* measurements of DNA binding by Msn2 revealed a higher affinity for STREs flanked by a 5' adenine. Both groups were enriched for STREs with a 5' flanking adenine, especially Msn2(6A), though this may reflect 1) that it induced more genes above the two-fold threshold and 2) that 38% of STREs in the yeast genome have 5' flanking adenines.

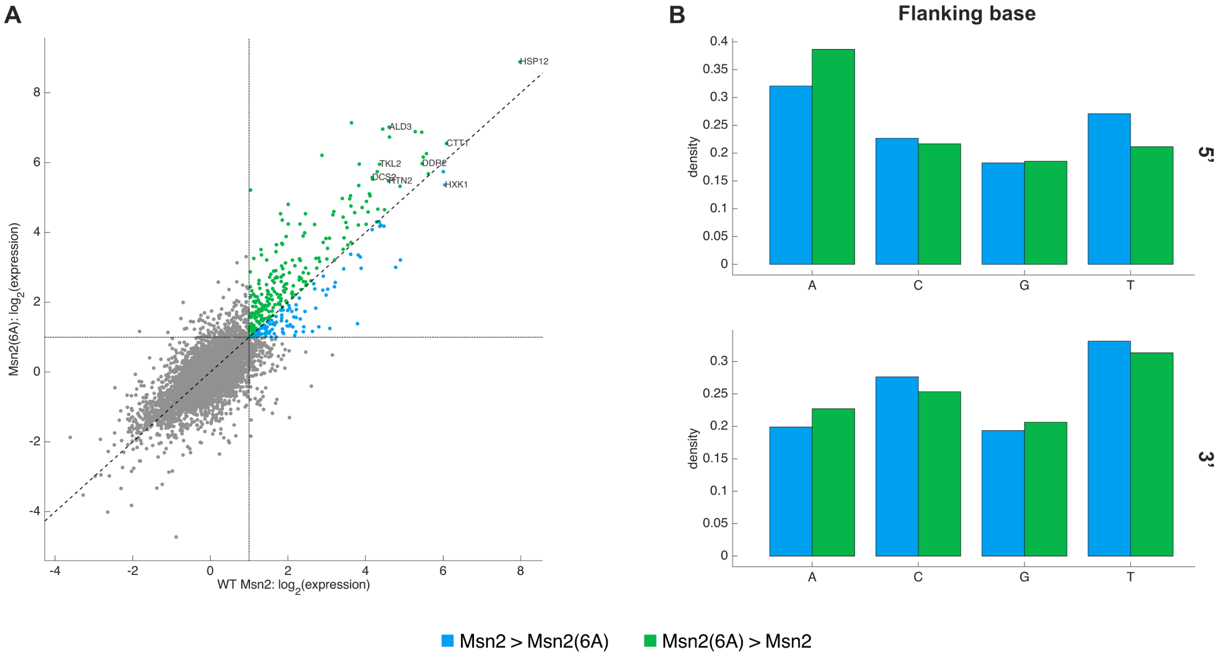

Figure A.1.5 Msn2 versus Msn2(6A). (**A**) Expression of Msn2 target genes 90 min after estradiol was added to strains with Msn2 or Msn2(6A) under the control of the Z_4EV induction system. There were 106 genes (containing 181 STREs) with greater than two-fold induction and higher expression for Msn2 than

Msn2(6A) (blue). There were 230 genes (containing 383 STREs) with greater than two-fold induction and higher expression for Msn2(6A) than Msn2 (green). (**B**) Frequency of 5’ and 3’ flanking bases for STREs of genes highlighted in Figure A.1.5A.

A.1.4 Msn4, the paralog of Msn2

Msn2 has a paralog, Msn4, that arose through whole genome duplication (WGD). Msn2 and Msn4 share 41% sequence homology and are both regulated by PKA, exhibit similar pulsatile dynamics, and bind STREs, though Msn2 expression is constitutive, while Msn4 expression is induced by Msn2 [88], [96]. Various studies have explored why both TFs have been maintained for ~100 million years since the WGD event [30], [35], [88]. It was proposed that asynchronous nuclear localization of Msn2 and Msn4 in response to natural stresses can enhance the expression of their shared targets [30]. Conversely, a study using chemical modulation of PKA activity found that strong induction of SIP18 and TKL2 requires both Msn2 and Msn4 [35]. Whether or not Msn2 and Msn4 are functionally redundant is disputed [35], [88].

A.2 Integrating optogenetic stimulation and microscopy

A.2.1 Introduction

The work in this thesis relating light-induced Msn2 localization dynamics to gene expression required the ability to simultaneously stimulate cells with light and measure their response via fluorescence microscopy. In fact, the light sweep experiments of Chapter 5 alone entailed more than 2500 individual timelapse microscopy experiments. We therefore needed to develop an experimental system capable of collecting, organizing, and analyzing single-cell fluorescence measurements at high-throughput.

A.2.2 Refinements to the optoPlate to facilitate microscopy

To stimulate cells with light and measure resulting changes in TF localization or reporter expression, we used a custom adaptor to mount an optoPlate on a microscope stage over a 96-well plate containing our reporter strains. Because microscopes magnify everything, especially your mistakes, this involved a few rounds of refinements and failed experiments. To enable high-throughput optogenetic imaging experiments, Edvard Grødem rewrote the optoPlate firmware so that it could be 1) calibrated as described in Chapter 4, 2) programmed directly from a plate map containing the details of each experiment, and 3) controlled by the microscope. The updated firmware and stage adaptor are available online [68].

A.2.3 Control of high-throughput microscopy

We used the JOBS module of NIS-Elements to control our high-throughput timelapse microscopy experiments. Our custom JOB communicated with the optoPlate to sync the timed delivery of light with the experiment and turn off LEDs in wells being imaged. We maintained focus using the Nikon Perfect Focus System (PFS). However, when imaging many wells of a 96-well plate under a heavy optoPlate that could occasionally shift, perfect focus was at best an aspiration. We therefore created a custom refocusing algorithm that could re-establish focus by returning to previously logged z-positions at which a given well was in focus or, failing that, incrementally moving up and down in z-space until focus was restored.

A.2.4 Segmentation and measurement of yeast from microscopy images

Our light sweep experiments collected a large amount of image data (more than 1.4 TB of raw .ND2 files). To gain biological insights from this data, we developed a custom image analysis pipeline in MATLAB. Briefly (as shown in Figure A.2.1A), we loaded multi-channel timelapse images (.ND2 files) and extracted timestamps using the Bio-Formats loader [112]. The images were processed with a Laplacian of Gaussian filter to enhance contrast and circular regions of interest (ROIs) likely containing yeast cells or nuclei were identified using MATLAB's circle finder. Single-cell fluorescence measurements were then made for each ROI. Optionally, cells and nuclei identified from different image channels could be paired and tracked, though we did not do this for the light sweep experiments.

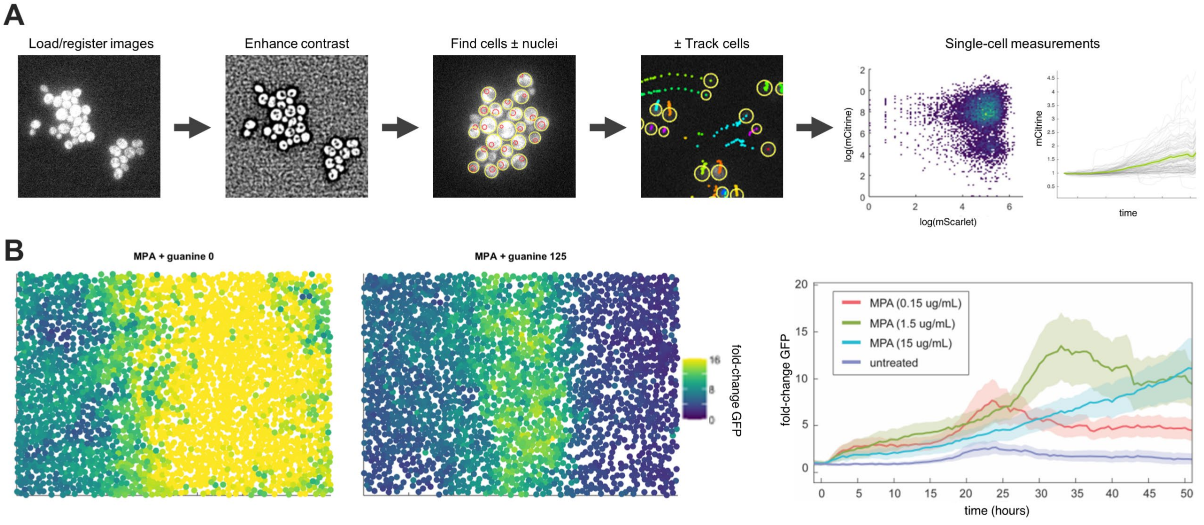

Figure A.2.1 Custom image analysis tools. (**A**) Overview of image analysis pipeline. (**B**) Images collected by Erica Schwotzer showing expression of an IMD2 reporter (GFP) following treatment with mycophenolic acid (MPA). (Left) Spatial distribution of IMD2 expression at a single timepoint for two conditions. Each point represents median GFP expression of a single yeast cell. (Right) IMD2 expression over time following treatment. Lines and shaded regions represent mean and standard deviation of single-cell GFP measurements.

This simple approach proved surprisingly effective and could identify single cells from images of densely grown yeast. This led to a collaboration with Erica Schwotzer of the Brow Lab who investigates the role of post-transcriptional regulation in the expression of IMD2, a gene involved in guanine nucleotide synthesis whose human equivalent is associated with retinal degeneration. Erica wanted to measure IMD2 expression from images of yeast grown to confluence (Figure A.2.1B), but this proved difficult using publicly available image analysis tools. I therefore analyzed her images using my MATLAB pipeline and will be a co-author on her upcoming paper:

Schwotzer EL, Sweeney K, Sundlin KE, McClean MN, and Brow DA. Expression of the *Saccharomyces cerevisiae* IMD2 gene is induced by cell crowding on a solid substrate (in preparation)

A.2.5 Integrating optogenetic control, microscopy, and image analysis

To facilitate high-throughput experiments, we integrated the components of our system (optoPlate, microscope, and image analysis pipeline) using plate maps—spreadsheets defining the strains, conditions, and light programs for each well imaged (Figure A.2.2). Light programs containing the appropriate time-varying light dose per well were flashed to the optoPlate directly from the plate map. The plate map was also used to name each image output by the microscope and to append the correct labels (reporter, Msn2 mutant, light condition, etc.) to each single-cell fluorescence measurement extracted by the image analysis pipeline. An arbitrary number of labels for each well can be stored in a given plate map. Overall, this system allowed us to image a 96-well plate each day and automatically analyze the resulting (50 GB) set of images overnight using a mid-range laptop computer.

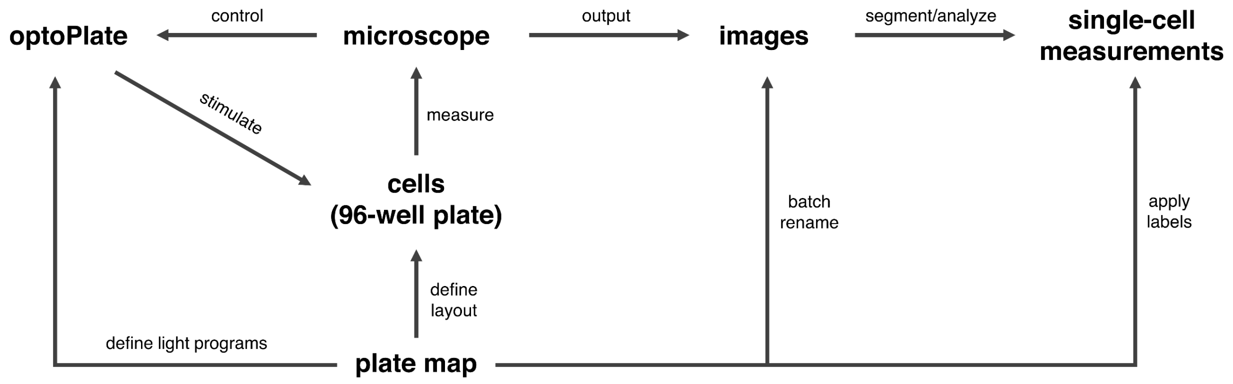

Figure A.2.2 Integrated optogenetic microscopy system. The optoPlate delivers defined time-varying light doses to cells growing in a 96-well plate on a microscope, which controls the optoPlate as described previously and outputs images for analysis by a custom MATLAB pipeline. Plate maps defining the layout of the 96-well plate and the light doses delivered by the optoPlate were used to label the images and the single-cell fluorescence measurements extracted from them.

A.3 A custom pipeline for high-throughput analysis of flow cytometry data

In the course of the work presented in this thesis, I used flow cytometry extensively to both measure the response of Msn2 target genes to stress and screen newly constructed strains. For the light sweep experiments alone, I created over 100 yeast strains (see Section A.5), each of which had to be screened to identify at least three biological replicates with appropriate levels of Msn2 ± CLASP. In total, this entailed screening thousands of colonies by flow cytometry, which was prohibitively slow using off-the-shelf software for analyzing flow cytometry data. I therefore developed a custom MATLAB pipeline for analyzing flow cytometry data (Figure A.3.1). This pipeline integrates an existing .FCS file loader [73] and plotting toolbox [72] with new tools for gating events and applying labels from plate maps (96-well or 384-well) like those described in Section A.2.5, allowing for high-throughput, automated analysis of flow cytometry data. The pipeline is available online [113] and has been used by other McClean Lab members in their research.

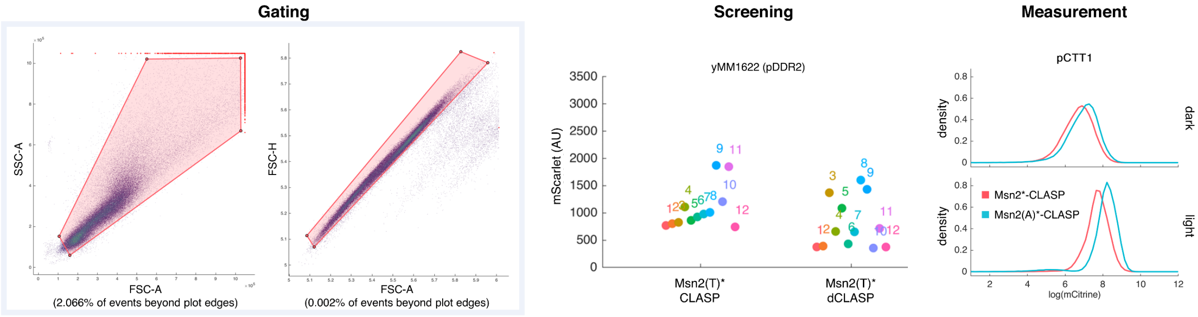

Figure A.3.1 Overview of flow cytometry analysis pipeline. (Left) One may apply an arbitrary number of nested gates to their flow cytometry data. Here a gate was applied to exclude debris (SSC-A vs FSC-A) and another gate was applied to the remaining events to isolate singlets (FSC-H vs FSC-A). Automatic labeling from plate maps allows high-throughput analysis of flow cytometry measurements for screening strains (middle) or performing experiments (right).

A.4 LOV actually: controlling Msn2 with LINUS

Our initial efforts to control Msn2 with light used LINUS (light inducible nuclear localization signal) [37]. Like the yeLANS component of CLASP (Figure 5.1), LINUS is based on the LOV2 domain of *Avena sativa* phototropin 1, but has a different NLS embedded within its Jα tail. Msn2-LINUS constructs exhibited graded nuclear localization in response to increasing doses of blue light (Figure A.4.1A), but were poor at inducing the expression of Msn2 target genes (data not shown). We initially thought that leakiness, the spontaneous unfolding of the Jα tail in the dark, caused unwanted nuclear localization and thus degradation of Msn2-LINUS (see Section 5.3.4). However, the basal expression of mScarlet-LINUS was 4.1-fold lower than mScarlet-yeLANS (Figure A.4.1B), indicating that even without Msn2, LINUS is poorly expressed or degraded by the cell, possibly because its SV40-based NLS includes a sequence (KKKRK) similar to D box degrons [114], [115].

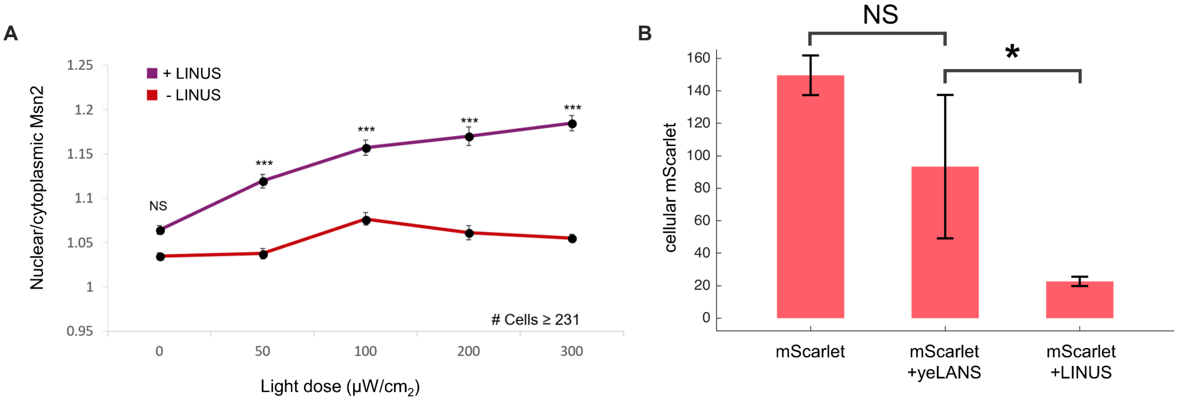

Figure A.4.1 Controlling Msn2 with LINUS. (**A**) Msn2 ± LINUS localization versus light dose. Cells were exposed to blue light on an LPA five-minutes, then fixed and measured by fluorescence microscopy. Points and error bars represent mean and SEM of single-cell nuclear localization measurements. (**B**) Flow cytometry measurements showing basal fluorescence of mScarlet, mScarlet-yeLANS, and mScarlet-LINUS, all expressed under the constitutive Msn2 promoter. Bars and error bars represent mean and standard deviation of fluorescence for three biological replicates. A two-sample t-test of the null hypothesis that mScarlet-yeLANS>mScarlet-LINUS showed a significant difference (p = 0.025) between constructs.

A.5 List of strains used in light sweep experiments

The following strains were used for the light sweep experiments and were constructed and screened as described in Section 5.2.1. All strains are in the S288C background.

Strain	Genotype	Description
yMM1603/pMM0845	MAT alpha his3D1 leu2D0 lys2D0 MET15 ura3D0 Nhp6a-iRFP msn2D0 msn4D0 leu2D0::ConS-glpT_promoter-sfGFP_BBa_B0015_terminator-Con1-pLEU2-LEU2-Ag_tLEU2 URA3 5' Homology-ConS-pRPL18B-Zdk1-Msn2-mScarlet-yeLANS-tADH1-Con1-pRPL18B-Hs_RGS2(33-67)_13aa-iRFP713 (iRFP)-asLOV2(404-546)-tPGK1-ConE-URA3 (pSc-native-tSc)-URA3 3' Homology-KanR-ColE1	glpT-sfGFP + Msn2-CLASP
yMM1603/pMM0846	MAT alpha his3D1 leu2D0 lys2D0 MET15 ura3D0 Nhp6a-iRFP msn2D0 msn4D0 leu2D0::ConS-glpT_promoter-sfGFP_BBa_B0015_terminator-Con1-pLEU2-LEU2-Ag_tLEU2 URA3 5' Homology-ConS-pRPL18B-Zdk1-Msn2(S582E S620E S625E S633E S686A)-mScarlet-yeLANS-tADH1-Con1-pRPL18B-Hs_RGS2(33-67)_13aa-iRFP713 (iRFP)-asLOV2(404-546)-tPGK1-ConE-URA3 (pSc-native-tSc)-URA3 3' Homology-KanR-ColE1	glpT-sfGFP + Msn2(A)*-CLASP
yMM1603/pMM0847	MAT alpha his3D1 leu2D0 lys2D0 MET15 ura3D0 Nhp6a-iRFP msn2D0 msn4D0 leu2D0::ConS-glpT_promoter-sfGFP_BBa_B0015_terminator-Con1-pLEU2-LEU2-Ag_tLEU2 URA3 5' Homology-ConS-pRPL18B-Zdk1-Msn2(S582E S620E S625E S633E)-mScarlet-yeLANS-tADH1-Con1-pRPL18B-Hs_RGS2(33- 67)_13aa-iRFP713 (iRFP)-asLOV2(404-546)-tPGK1-ConE-URA3 (pSc-native-tSc)-URA3 3' Homology-KanR-ColE1	glpT-sfGFP + Msn2*-CLASP
yMM1603/pMM0858	MAT alpha his3D1 leu2D0 lys2D0 MET15 ura3D0 Nhp6a-iRFP msn2D0 msn4D0 leu2D0::ConS-glpT_promoter-sfGFP_BBa_B0015_terminator-Con1-pLEU2-LEU2-Ag_tLEU2 URA3 5' Homology-ConS-pRPL18B-Msn2-mScarlet-tADH1-Con1-pRPL18B-Hs_RGS2(33-67)_13aa-iRFP713 (iRFP)-asLOV2(404-546)-tPGK1-ConE-URA3 (pSc-native-tSc)-URA3 3' Homology-KanR-ColE1	glpT-sfGFP + Msn2-dCLASP
yMM1603/pMM0859	MAT alpha his3D1 leu2D0 lys2D0 MET15 ura3D0 Nhp6a-iRFP msn2D0 msn4D0 leu2D0::ConS-glpT_promoter-sfGFP_BBa_B0015_terminator-Con1-pLEU2-LEU2-Ag_tLEU2 URA3 5' Homology-ConS-pRPL18B-Msn2(S582E S620E S625E S633E S686A)-mScarlet-tADH1-Con1-pRPL18B-Hs_RGS2(33- 67)_13aa-iRFP713 (iRFP)-asLOV2(404-546)-tPGK1-ConE-URA3 (pSc-native-tSc)-URA3 3' Homology-KanR-ColE1	glpT-sfGFP + Msn2(A)*-dCLASP
yMM1603/pMM0860	MAT alpha his3D1 leu2D0 lys2D0 MET15 ura3D0 Nhp6a-iRFP msn2D0 msn4D0 leu2D0::ConS-glpT_promoter-sfGFP_BBa_B0015_terminator-Con1-pLEU2-LEU2-Ag_tLEU2 URA3 5' Homology-ConS-pRPL18B-Msn2(S582E S620E S625E S633E)-mScarlet-tADH1-Con1-pRPL18B-Hs_RGS2(33- 67)_13aa-iRFP713 (iRFP)-asLOV2(404-546)-tPGK1-ConE-URA3 (pSc-native-tSc)-URA3 3' Homology-KanR-ColE1	glpT-sfGFP + Msn2*-dCLASP
yMM1603/pMM1079	MAT alpha his3D1 leu2D0 lys2D0 MET15 ura3D0 Nhp6a-iRFP msn2D0 msn4D0 leu2D0::ConS-glpT_promoter-sfGFP_BBa_B0015_terminator-Con1-pLEU2-LEU2-Ag_tLEU2 URA3 5' Homology-ConS-pRPL18B-Zdk1-Msn2(S582E S620E S625E S633E S671T N672G R674K)-mScarlet-yeLANS-tADH1-Con1-pRPL18B-Hs_RGS2(33- 67)_13aa-iRFP713 (iRFP)-asLOV2(404-546)-tPGK1-ConE-URA3 (pSc-native-tSc)-URA3 3' Homology-KanR-ColE1	glpT-sfGFP + Msn2(T)*-CLASP
yMM1603/pMM1083	MAT alpha his3D1 leu2D0 lys2D0 MET15 ura3D0 Nhp6a-iRFP msn2D0 msn4D0 leu2D0::ConS-glpT_promoter-sfGFP_BBa_B0015_terminator-Con1-pLEU2-LEU2-Ag_tLEU2 URA3 5' Homology-ConS-pRPL18B-Msn2(S582E S620E S625E S633E S671T N672G R674K)-mScarlet-tADH1-Con1-pRPL18B-Hs_RGS2(33- 67)_13aa-iRFP713 (iRFP)-asLOV2(404-546)-tPGK1-ConE-URA3 (pSc-native-tSc)-URA3 3' Homology-KanR-ColE1	glpT-sfGFP + Msn2(T)*-dCLASP
yMM1604/pMM0845	MAT alpha his3D1 leu2D0 lys2D0 MET15 ura3D0 Nhp6a-iRFP msn2D0 msn4D0 leu2D0::ConS-pHXK1-mCitrine(V163A)-tADH1-Con1-pLEU2-LEU2-Ag_tLEU2 URA3 5' Homology-ConS-pRPL18B-Zdk1-Msn2-mScarlet-yeLANS-tADH1-Con1-pRPL18B-Hs_RGS2(33-67)_13aa-iRFP713 (iRFP)-asLOV2(404-546)-tPGK1-ConE-URA3 (pSc-native-tSc)-URA3 3' Homology-KanR-ColE1	HXK1-mCitrine + Msn2-CLASP

yMM1604/pMM0846	MAT alpha his3D1 leu2D0 lys2D0 MET15 ura3D0 Nhp6a-iRFP msn2D0 msn4D0 leu2D0::ConS-pHXK1-mCitrine(V163A)-tADH1-Con1-pLEU2-LEU2-Ag_tLEU2 URA3 5' Homology-ConS-pRPL18B-Zdk1-Msn2(S582E S620E S625E S633E S686A)-mScarlet-yeLANS-tADH1-Con1-pRPL18B-Hs_RGS2(33-67)_13aa-iRFP713 (iRFP)-asLOV2(404-546)-tPGK1-ConE-URA3 (pSc-native-tSc)-URA3 3' Homology-KanR-ColE1	HXK1-mCitrine + Msn2(A)*-CLASP
yMM1604/pMM0847	MAT alpha his3D1 leu2D0 lys2D0 MET15 ura3D0 Nhp6a-iRFP msn2D0 msn4D0 leu2D0::ConS-pHXK1-mCitrine(V163A)-tADH1-Con1-pLEU2-LEU2-Ag_tLEU2 URA3 5' Homology-ConS-pRPL18B-Zdk1-Msn2(S582E S620E S625E S633E)-mScarlet-yeLANS-tADH1-Con1-pRPL18B-Hs_RGS2(33- 67)_13aa-iRFP713 (iRFP)-asLOV2(404-546)-tPGK1-ConE-URA3 (pSc-native-tSc)-URA3 3' Homology-KanR-ColE1	HXK1-mCitrine + Msn2*-CLASP
yMM1604/pMM0858	MAT alpha his3D1 leu2D0 lys2D0 MET15 ura3D0 Nhp6a-iRFP msn2D0 msn4D0 leu2D0::ConS-pHXK1-mCitrine(V163A)-tADH1-Con1-pLEU2-LEU2-Ag_tLEU2 URA3 5' Homology-ConS-pRPL18B-Msn2-mScarlet-tADH1-Con1-pRPL18B-Hs_RGS2(33- 67)_13aa-iRFP713 (iRFP)-asLOV2(404-546)-tPGK1-ConE-URA3 (pSc-native-tSc)-URA3 3' Homology-KanR-ColE1	HXK1-mCitrine + Msn2-dCLASP
yMM1604/pMM0859	MAT alpha his3D1 leu2D0 lys2D0 MET15 ura3D0 Nhp6a-iRFP msn2D0 msn4D0 leu2D0::ConS-pHXK1-mCitrine(V163A)-tADH1-Con1-pLEU2-LEU2-Ag_tLEU2 URA3 5' Homology-ConS-pRPL18B-Msn2(S582E S620E S625E S633E S686A)-mScarlet-tADH1-Con1-pRPL18B-Hs_RGS2(33- 67)_13aa-iRFP713 (iRFP)-asLOV2(404-546)-tPGK1-ConE-URA3 (pSc-native-tSc)-URA3 3' Homology-KanR-ColE1	HXK1-mCitrine + Msn2(A)*-dCLASP
yMM1604/pMM0860	MAT alpha his3D1 leu2D0 lys2D0 MET15 ura3D0 Nhp6a-iRFP msn2D0 msn4D0 leu2D0::ConS-pHXK1-mCitrine(V163A)-tADH1-Con1-pLEU2-LEU2-Ag_tLEU2 URA3 5' Homology-ConS-pRPL18B-Msn2(S582E S620E S625E S633E)-mScarlet-tADH1-Con1-pRPL18B-Hs_RGS2(33- 67)_13aa-iRFP713 (iRFP)-asLOV2(404-546)-tPGK1-ConE-URA3 (pSc-native-tSc)-URA3 3' Homology-KanR-ColE1	HXK1-mCitrine + Msn2*-dCLASP
yMM1604/pMM1070	MAT alpha his3D1 leu2D0 lys2D0 MET15 ura3D0 Nhp6a-iRFP msn2D0 msn4D0 leu2D0::ConS-pHXK1-mCitrine(V163A)-tADH1-Con1-pLEU2-LEU2-Ag_tLEU2 URA3 5' Homology-ConS-pRPL18B-Zdk1-Msn2(S582E S620E S625E S633E S686D)-mScarlet-yeLANS-tADH1-Con1-pRPL18B-Hs_RGS2(33- 67)_13aa-iRFP713 (iRFP)-asLOV2(404-546)-tPGK1-ConE-URA3 (pSc-native-tSc)-URA3 3' Homology-KanR-ColE1	HXK1-mCitrine + Msn2(D)*-CLASP
yMM1604/pMM1072	MAT alpha his3D1 leu2D0 lys2D0 MET15 ura3D0 Nhp6a-iRFP msn2D0 msn4D0 leu2D0::ConS-pHXK1-mCitrine(V163A)-tADH1-Con1-pLEU2-LEU2-Ag_tLEU2 URA3 5' Homology-ConS-pRPL18B-Msn2(S582E S620E S625E S633E S686D)-mScarlet-tADH1-Con1-pRPL18B-Hs_RGS2(33- 67)_13aa-iRFP713 (iRFP)-asLOV2(404-546)-tPGK1-ConE-URA3 (pSc-native-tSc)-URA3 3' Homology-KanR-ColE1	HXK1-mCitrine + Msn2(D)*-dCLASP
yMM1604/pMM1079	MAT alpha his3D1 leu2D0 lys2D0 MET15 ura3D0 Nhp6a-iRFP msn2D0 msn4D0 leu2D0::ConS-pHXK1-mCitrine(V163A)-tADH1-Con1-pLEU2-LEU2-Ag_tLEU2 URA3 5' Homology-ConS-pRPL18B-Zdk1-Msn2(S582E S620E S625E S633E S671T N672G R674K)-mScarlet-yeLANS-tADH1-Con1-pRPL18B-Hs_RGS2(33- 67)_13aa-iRFP713 (iRFP)-asLOV2(404-546)-tPGK1-ConE-URA3 (pSc-native-tSc)-URA3 3' Homology-KanR-ColE1	HXK1-mCitrine + Msn2(T)*-CLASP
yMM1604/pMM1083	MAT alpha his3D1 leu2D0 lys2D0 MET15 ura3D0 Nhp6a-iRFP msn2D0 msn4D0 leu2D0::ConS-pHXK1-mCitrine(V163A)-tADH1-Con1-pLEU2-LEU2-Ag_tLEU2 URA3 5' Homology-ConS-pRPL18B-Msn2(S582E S620E S625E S633E S671T N672G R674K)-mScarlet-tADH1-Con1-pRPL18B-Hs_RGS2(33- 67)_13aa-iRFP713 (iRFP)-asLOV2(404-546)-tPGK1-ConE-URA3 (pSc-native-tSc)-URA3 3' Homology-KanR-ColE1	HXK1-mCitrine + Msn2(T)*-dCLASP
yMM1605/pMM0845	MAT alpha his3D1 leu2D0 lys2D0 MET15 ura3D0 Nhp6a-iRFP msn2D0 msn4D0 leu2D0::ConS-pCTT1-mCitrine(V163A)-tADH1-Con1-pLEU2-LEU2-Ag_tLEU2 URA3 5' Homology-ConS-pRPL18B-Zdk1-Msn2-mScarlet-yeLANS-tADH1-Con1-pRPL18B-Hs_RGS2(33-67)_13aa-iRFP713 (iRFP)-asLOV2(404-546)-tPGK1-ConE-URA3 (pSc-native-tSc)-URA3 3' Homology-KanR-ColE1	CTT1-mCitrine + Msn2-CLASP
yMM1605/pMM0846	MAT alpha his3D1 leu2D0 lys2D0 MET15 ura3D0 Nhp6a-iRFP msn2D0 msn4D0 leu2D0::ConS-pCTT1-mCitrine(V163A)-tADH1-Con1-pLEU2-LEU2-Ag_tLEU2 URA3 5' Homology-ConS-pRPL18B-Zdk1-Msn2(S582E S620E S625E S633E S686A)-mScarlet-yeLANS-tADH1-Con1-pRPL18B-Hs_RGS2(33-67)_13aa-iRFP713 (iRFP)-asLOV2(404-546)-tPGK1-ConE-URA3 (pSc-native-tSc)-URA3 3' Homology-KanR-ColE1	CTT1-mCitrine + Msn2(A)*-CLASP
yMM1605/pMM0847	MAT alpha his3D1 leu2D0 lys2D0 MET15 ura3D0 Nhp6a-iRFP msn2D0 msn4D0 leu2D0::ConS-pCTT1-mCitrine(V163A)-tADH1-Con1-pLEU2-LEU2-Ag_tLEU2 URA3 5' Homology-ConS-pRPL18B-Zdk1-Msn2(S582E S620E S625E S633E)-mScarlet-yeLANS-tADH1-Con1-pRPL18B-Hs_RGS2(33- 67)_13aa-iRFP713 (iRFP)-asLOV2(404-546)-tPGK1-ConE-URA3 (pSc-native-tSc)-URA3 3' Homology-KanR-ColE1	CTT1-mCitrine + Msn2*-CLASP

yMM1605/pMM0858	MAT alpha his3D1 leu2D0 lys2D0 MET15 ura3D0 Nhp6a-iRFP msn2D0 msn4D0 leu2D0::ConS-pCTT1-mCitrine(V163A)-tADH1-Con1-pLEU2-LEU2-Ag_tLEU2 URA3 5' Homology-ConS-pRPL18B-Msn2-mScarlet-tADH1-Con1-pRPL18B-Hs_RGS2(33- 67)_13aa-iRFP713 (iRFP)-asLOV2(404-546)-tPGK1-ConE-URA3 (pSc-native-tSc)-URA3 3' Homology-KanR-ColE1	CTT1-mCitrine + Msn2-dCLASP
yMM1605/pMM0859	MAT alpha his3D1 leu2D0 lys2D0 MET15 ura3D0 Nhp6a-iRFP msn2D0 msn4D0 leu2D0::ConS-pCTT1-mCitrine(V163A)-tADH1-Con1-pLEU2-LEU2-Ag_tLEU2 URA3 5' Homology-ConS-pRPL18B-Msn2(S582E S620E S625E S633E S686A)-mScarlet-tADH1-Con1-pRPL18B-Hs_RGS2(33- 67)_13aa-iRFP713 (iRFP)-asLOV2(404-546)-tPGK1-ConE-URA3 (pSc-native-tSc)-URA3 3' Homology-KanR-ColE1	CTT1-mCitrine + Msn2(A)*-dCLASP
yMM1605/pMM0860	MAT alpha his3D1 leu2D0 lys2D0 MET15 ura3D0 Nhp6a-iRFP msn2D0 msn4D0 leu2D0::ConS-pCTT1-mCitrine(V163A)-tADH1-Con1-pLEU2-LEU2-Ag_tLEU2 URA3 5' Homology-ConS-pRPL18B-Msn2(S582E S620E S625E S633E)-mScarlet-tADH1-Con1-pRPL18B-Hs_RGS2(33- 67)_13aa-iRFP713 (iRFP)-asLOV2(404-546)-tPGK1-ConE-URA3 (pSc-native-tSc)-URA3 3' Homology-KanR-ColE1	CTT1-mCitrine + Msn2*-dCLASP
yMM1605/pMM1070	MAT alpha his3D1 leu2D0 lys2D0 MET15 ura3D0 Nhp6a-iRFP msn2D0 msn4D0 leu2D0::ConS-pCTT1-mCitrine(V163A)-tADH1-Con1-pLEU2-LEU2-Ag_tLEU2 URA3 5' Homology-ConS-pRPL18B-Zdk1-Msn2(S582E S620E S625E S633E S686D)-mScarlet-yeLANS-tADH1-Con1-pRPL18B-Hs_RGS2(33- 67)_13aa-iRFP713 (iRFP)-asLOV2(404-546)-tPGK1-ConE-URA3 (pSc-native-tSc)-URA3 3' Homology-KanR-ColE1	CTT1-mCitrine + Msn2(D)*-CLASP
yMM1605/pMM1072	MAT alpha his3D1 leu2D0 lys2D0 MET15 ura3D0 Nhp6a-iRFP msn2D0 msn4D0 leu2D0::ConS-pCTT1-mCitrine(V163A)-tADH1-Con1-pLEU2-LEU2-Ag_tLEU2 URA3 5' Homology-ConS-pRPL18B-Msn2(S582E S620E S625E S633E S686D)-mScarlet-tADH1-Con1-pRPL18B-Hs_RGS2(33- 67)_13aa-iRFP713 (iRFP)-asLOV2(404-546)-tPGK1-ConE-URA3 (pSc-native-tSc)-URA3 3' Homology-KanR-ColE1	CTT1-mCitrine + Msn2(D)*-dCLASP
yMM1605/pMM1079	MAT alpha his3D1 leu2D0 lys2D0 MET15 ura3D0 Nhp6a-iRFP msn2D0 msn4D0 leu2D0::ConS-pCTT1-mCitrine(V163A)-tADH1-Con1-pLEU2-LEU2-Ag_tLEU2 URA3 5' Homology-ConS-pRPL18B-Zdk1-Msn2(S582E S620E S625E S633E S671T N672G R674K)-mScarlet-yeLANS-tADH1-Con1-pRPL18B-Hs_RGS2(33- 67)_13aa-iRFP713 (iRFP)-asLOV2(404-546)-tPGK1-ConE-URA3 (pSc-native-tSc)-URA3 3' Homology-KanR-ColE1	CTT1-mCitrine + Msn2(T)*-CLASP
yMM1605/pMM1083	MAT alpha his3D1 leu2D0 lys2D0 MET15 ura3D0 Nhp6a-iRFP msn2D0 msn4D0 leu2D0::ConS-pCTT1-mCitrine(V163A)-tADH1-Con1-pLEU2-LEU2-Ag_tLEU2 URA3 5' Homology-ConS-pRPL18B-Msn2(S582E S620E S625E S633E S671T N672G R674K)-mScarlet-tADH1-Con1-pRPL18B-Hs_RGS2(33- 67)_13aa-iRFP713 (iRFP)-asLOV2(404-546)-tPGK1-ConE-URA3 (pSc-native-tSc)-URA3 3' Homology-KanR-ColE1	CTT1-mCitrine + Msn2(T)*-dCLASP
yMM1606/pMM0845	MAT alpha his3D1 leu2D0 lys2D0 MET15 ura3D0 Nhp6a-iRFP msn2D0 msn4D0 leu2D0::ConS-pSIP18-mCitrine(V163A)-tADH1-Con1-pLEU2-LEU2-Ag_tLEU2 URA3 5' Homology-ConS-pRPL18B-Zdk1-Msn2-mScarlet-yeLANS-tADH1-Con1-pRPL18B-Hs_RGS2(33-67)_13aa-iRFP713 (iRFP)-asLOV2(404-546)-tPGK1-ConE-URA3 (pSc-native-tSc)-URA3 3' Homology-KanR-ColE1	SIP18-mCitrine + Msn2-CLASP
yMM1606/pMM0846	MAT alpha his3D1 leu2D0 lys2D0 MET15 ura3D0 Nhp6a-iRFP msn2D0 msn4D0 leu2D0::ConS-pSIP18-mCitrine(V163A)-tADH1-Con1-pLEU2-LEU2-Ag_tLEU2 URA3 5' Homology-ConS-pRPL18B-Zdk1-Msn2(S582E S620E S625E S633E S686A)-mScarlet-yeLANS-tADH1-Con1-pRPL18B-Hs_RGS2(33-67)_13aa-iRFP713 (iRFP)-asLOV2(404-546)-tPGK1-ConE-URA3 (pSc-native-tSc)-URA3 3' Homology-KanR-ColE1	SIP18-mCitrine + Msn2(A)*-CLASP
yMM1606/pMM0847	MAT alpha his3D1 leu2D0 lys2D0 MET15 ura3D0 Nhp6a-iRFP msn2D0 msn4D0 leu2D0::ConS-pSIP18-mCitrine(V163A)-tADH1-Con1-pLEU2-LEU2-Ag_tLEU2 URA3 5' Homology-ConS-pRPL18B-Zdk1-Msn2(S582E S620E S625E S633E)-mScarlet-yeLANS-tADH1-Con1-pRPL18B-Hs_RGS2(33- 67)_13aa-iRFP713 (iRFP)-asLOV2(404-546)-tPGK1-ConE-URA3 (pSc-native-tSc)-URA3 3' Homology-KanR-ColE1	SIP18-mCitrine + Msn2*-CLASP
yMM1606/pMM0858	MAT alpha his3D1 leu2D0 lys2D0 MET15 ura3D0 Nhp6a-iRFP msn2D0 msn4D0 leu2D0::ConS-pSIP18-mCitrine(V163A)-tADH1-Con1-pLEU2-LEU2-Ag_tLEU2 URA3 5' Homology-ConS-pRPL18B-Msn2-mScarlet-tADH1-Con1-pRPL18B-Hs_RGS2(33- 67)_13aa-iRFP713 (iRFP)-asLOV2(404-546)-tPGK1-ConE-URA3 (pSc-native-tSc)-URA3 3' Homology-KanR-ColE1	SIP18-mCitrine + Msn2-dCLASP
yMM1606/pMM0859	MAT alpha his3D1 leu2D0 lys2D0 MET15 ura3D0 Nhp6a-iRFP msn2D0 msn4D0 leu2D0::ConS-pSIP18-mCitrine(V163A)-tADH1-Con1-pLEU2-LEU2-Ag_tLEU2 URA3 5' Homology-ConS-pRPL18B-Msn2(S582E S620E S625E S633E S686A)-mScarlet-tADH1-Con1-pRPL18B-Hs_RGS2(33- 67)_13aa-iRFP713 (iRFP)-asLOV2(404-546)-tPGK1-ConE-URA3 (pSc-native-tSc)-URA3 3' Homology-KanR-ColE1	SIP18-mCitrine + Msn2(A)*-dCLASP

yMM1606/pMM0860	MAT alpha his3D1 leu2D0 lys2D0 MET15 ura3D0 Nhp6a-iRFP msn2D0 msn4D0 leu2D0::ConS-pSIP18-mCitrine(V163A)-tADH1-Con1-pLEU2-LEU2-Ag_tLEU2 URA3 5' Homology-ConS-pRPL18B-Msn2(S582E S620E S625E S633E)-mScarlet-tADH1-Con1-pRPL18B-Hs_RGS2(33- 67)_13aa-iRFP713 (iRFP)-asLOV2(404-546)-tPGK1-ConE-URA3 (pSc-native-tSc)-URA3 3' Homology-KanR-ColE1	SIP18-mCitrine + Msn2*-dCLASP
yMM1606/pMM1079	MAT alpha his3D1 leu2D0 lys2D0 MET15 ura3D0 Nhp6a-iRFP msn2D0 msn4D0 leu2D0::ConS-pSIP18-mCitrine(V163A)-tADH1-Con1-pLEU2-LEU2-Ag_tLEU2 URA3 5' Homology-ConS-pRPL18B-Zdk1-Msn2(S582E S620E S625E S633E S671T N672G R674K)-mScarlet-yeLANS-tADH1-Con1-pRPL18B-Hs_RGS2(33- 67)_13aa-iRFP713 (iRFP)-asLOV2(404-546)-tPGK1-ConE-URA3 (pSc-native-tSc)-URA3 3' Homology-KanR-ColE1	SIP18-mCitrine + Msn2(T)*-CLASP
yMM1606/pMM1083	MAT alpha his3D1 leu2D0 lys2D0 MET15 ura3D0 Nhp6a-iRFP msn2D0 msn4D0 leu2D0::ConS-pSIP18-mCitrine(V163A)-tADH1-Con1-pLEU2-LEU2-Ag_tLEU2 URA3 5' Homology-ConS-pRPL18B-Msn2(S582E S620E S625E S633E S671T N672G R674K)-mScarlet-tADH1-Con1-pRPL18B-Hs_RGS2(33- 67)_13aa-iRFP713 (iRFP)-asLOV2(404-546)-tPGK1-ConE-URA3 (pSc-native-tSc)-URA3 3' Homology-KanR-ColE1	SIP18-mCitrine + Msn2(T)*-dCLASP
yMM1607/pMM0845	MAT alpha his3D1 leu2D0 lys2D0 MET15 ura3D0 Nhp6a-iRFP msn2D0 msn4D0 leu2D0::ConS-pDCS2-mCitrine(V163A)-tADH1-Con1-pLEU2-LEU2-Ag_tLEU2 URA3 5' Homology-ConS-pRPL18B-Zdk1-Msn2-mScarlet-yeLANS-tADH1-Con1-pRPL18B-Hs_RGS2(33-67)_13aa-iRFP713 (iRFP)-asLOV2(404-546)-tPGK1-ConE-URA3 (pSc-native-tSc)-URA3 3' Homology-KanR-ColE1	DCS2-mCitrine + Msn2-CLASP
yMM1607/pMM0846	MAT alpha his3D1 leu2D0 lys2D0 MET15 ura3D0 Nhp6a-iRFP msn2D0 msn4D0 leu2D0::ConS-pDCS2-mCitrine(V163A)-tADH1-Con1-pLEU2-LEU2-Ag_tLEU2 URA3 5' Homology-ConS-pRPL18B-Zdk1-Msn2(S582E S620E S625E S633E S686A)-mScarlet-yeLANS-tADH1-Con1-pRPL18B-Hs_RGS2(33-67)_13aa-iRFP713 (iRFP)-asLOV2(404-546)-tPGK1-ConE-URA3 (pSc-native-tSc)-URA3 3' Homology-KanR-ColE1	DCS2-mCitrine + Msn2(A)*-CLASP
yMM1607/pMM0847	MAT alpha his3D1 leu2D0 lys2D0 MET15 ura3D0 Nhp6a-iRFP msn2D0 msn4D0 leu2D0::ConS-pDCS2-mCitrine(V163A)-tADH1-Con1-pLEU2-LEU2-Ag_tLEU2 URA3 5' Homology-ConS-pRPL18B-Zdk1-Msn2(S582E S620E S625E S633E)-mScarlet-yeLANS-tADH1-Con1-pRPL18B-Hs_RGS2(33- 67)_13aa-iRFP713 (iRFP)-asLOV2(404-546)-tPGK1-ConE-URA3 (pSc-native-tSc)-URA3 3' Homology-KanR-ColE1	DCS2-mCitrine + Msn2*-CLASP
yMM1607/pMM0858	MAT alpha his3D1 leu2D0 lys2D0 MET15 ura3D0 Nhp6a-iRFP msn2D0 msn4D0 leu2D0::ConS-pDCS2-mCitrine(V163A)-tADH1-Con1-pLEU2-LEU2-Ag_tLEU2 URA3 5' Homology-ConS-pRPL18B-Msn2-mScarlet-tADH1-Con1-pRPL18B-Hs_RGS2(33- 67)_13aa-iRFP713 (iRFP)-asLOV2(404-546)-tPGK1-ConE-URA3 (pSc-native-tSc)-URA3 3' Homology-KanR-ColE1	DCS2-mCitrine + Msn2-dCLASP
yMM1607/pMM0859	MAT alpha his3D1 leu2D0 lys2D0 MET15 ura3D0 Nhp6a-iRFP msn2D0 msn4D0 leu2D0::ConS-pDCS2-mCitrine(V163A)-tADH1-Con1-pLEU2-LEU2-Ag_tLEU2 URA3 5' Homology-ConS-pRPL18B-Msn2(S582E S620E S625E S633E S686A)-mScarlet-tADH1-Con1-pRPL18B-Hs_RGS2(33- 67)_13aa-iRFP713 (iRFP)-asLOV2(404-546)-tPGK1-ConE-URA3 (pSc-native-tSc)-URA3 3' Homology-KanR-ColE1	DCS2-mCitrine + Msn2(A)*-dCLASP
yMM1607/pMM0860	MAT alpha his3D1 leu2D0 lys2D0 MET15 ura3D0 Nhp6a-iRFP msn2D0 msn4D0 leu2D0::ConS-pDCS2-mCitrine(V163A)-tADH1-Con1-pLEU2-LEU2-Ag_tLEU2 URA3 5' Homology-ConS-pRPL18B-Msn2(S582E S620E S625E S633E)-mScarlet-tADH1-Con1-pRPL18B-Hs_RGS2(33- 67)_13aa-iRFP713 (iRFP)-asLOV2(404-546)-tPGK1-ConE-URA3 (pSc-native-tSc)-URA3 3' Homology-KanR-ColE1	DCS2-mCitrine + Msn2*-dCLASP
yMM1607/pMM1079	MAT alpha his3D1 leu2D0 lys2D0 MET15 ura3D0 Nhp6a-iRFP msn2D0 msn4D0 leu2D0::ConS-pDCS2-mCitrine(V163A)-tADH1-Con1-pLEU2-LEU2-Ag_tLEU2 URA3 5' Homology-ConS-pRPL18B-Zdk1-Msn2(S582E S620E S625E S633E S671T N672G R674K)-mScarlet-yeLANS-tADH1-Con1-pRPL18B-Hs_RGS2(33- 67)_13aa-iRFP713 (iRFP)-asLOV2(404-546)-tPGK1-ConE-URA3 (pSc-native-tSc)-URA3 3' Homology-KanR-ColE1	DCS2-mCitrine + Msn2(T)*-CLASP
yMM1607/pMM1083	MAT alpha his3D1 leu2D0 lys2D0 MET15 ura3D0 Nhp6a-iRFP msn2D0 msn4D0 leu2D0::ConS-pDCS2-mCitrine(V163A)-tADH1-Con1-pLEU2-LEU2-Ag_tLEU2 URA3 5' Homology-ConS-pRPL18B-Msn2(S582E S620E S625E S633E S671T N672G R674K)-mScarlet-tADH1-Con1-pRPL18B-Hs_RGS2(33- 67)_13aa-iRFP713 (iRFP)-asLOV2(404-546)-tPGK1-ConE-URA3 (pSc-native-tSc)-URA3 3' Homology-KanR-ColE1	DCS2-mCitrine + Msn2(T)*-dCLASP
yMM1608/pMM0845	MAT alpha his3D1 leu2D0 lys2D0 MET15 ura3D0 Nhp6a-iRFP msn2D0 msn4D0 leu2D0::ConS-pHSP12-mCitrine(V163A)-tADH1-Con1-pLEU2-LEU2-Ag_tLEU2 URA3 5' Homology-ConS-pRPL18B-Zdk1-Msn2-mScarlet-yeLANS-tADH1-Con1-pRPL18B-Hs_RGS2(33-67)_13aa-iRFP713 (iRFP)-asLOV2(404-546)-tPGK1-ConE-URA3 (pSc-native-tSc)-URA3 3' Homology-KanR-ColE1	HSP12-mCitrine + Msn2-CLASP

yMM1608/pMM0846	MAT alpha his3D1 leu2D0 lys2D0 MET15 ura3D0 Nhp6a-iRFP msn2D0 msn4D0 leu2D0::ConS-pHSP12-mCitrine(V163A)-tADH1-Con1-pLEU2-LEU2-Ag_tLEU2 URA3 5' Homology-ConS-pRPL18B-Zdk1-Msn2(S582E S620E S625E S633E S686A)-mScarlet-yeLANS-tADH1-Con1-pRPL18B-Hs_RGS2(33-67)_13aa-iRFP713 (iRFP)-asLOV2(404-546)-tPGK1-ConE-URA3 (pSc-native-tSc)-URA3 3' Homology-KanR-ColE1	HSP12-mCitrine + Msn2(A)*-CLASP
yMM1608/pMM0847	MAT alpha his3D1 leu2D0 lys2D0 MET15 ura3D0 Nhp6a-iRFP msn2D0 msn4D0 leu2D0::ConS-pHSP12-mCitrine(V163A)-tADH1-Con1-pLEU2-LEU2-Ag_tLEU2 URA3 5' Homology-ConS-pRPL18B-Zdk1-Msn2(S582E S620E S625E S633E)-mScarlet-yeLANS-tADH1-Con1-pRPL18B-Hs_RGS2(33- 67)_13aa-iRFP713 (iRFP)-asLOV2(404-546)-tPGK1-ConE-URA3 (pSc-native-tSc)-URA3 3' Homology-KanR-ColE1	HSP12-mCitrine + Msn2*-CLASP
yMM1608/pMM0858	MAT alpha his3D1 leu2D0 lys2D0 MET15 ura3D0 Nhp6a-iRFP msn2D0 msn4D0 leu2D0::ConS-pHSP12-mCitrine(V163A)-tADH1-Con1-pLEU2-LEU2-Ag_tLEU2 URA3 5' Homology-ConS-pRPL18B-Msn2-mScarlet-tADH1-Con1-pRPL18B-Hs_RGS2(33- 67)_13aa-iRFP713 (iRFP)-asLOV2(404-546)-tPGK1-ConE-URA3 (pSc-native-tSc)-URA3 3' Homology-KanR-ColE1	HSP12-mCitrine + Msn2-dCLASP
yMM1608/pMM0859	MAT alpha his3D1 leu2D0 lys2D0 MET15 ura3D0 Nhp6a-iRFP msn2D0 msn4D0 leu2D0::ConS-pHSP12-mCitrine(V163A)-tADH1-Con1-pLEU2-LEU2-Ag_tLEU2 URA3 5' Homology-ConS-pRPL18B-Msn2(S582E S620E S625E S633E S686A)-mScarlet-tADH1-Con1-pRPL18B-Hs_RGS2(33- 67)_13aa-iRFP713 (iRFP)-asLOV2(404-546)-tPGK1-ConE-URA3 (pSc-native-tSc)-URA3 3' Homology-KanR-ColE1	HSP12-mCitrine + Msn2(A)*-dCLASP
yMM1608/pMM0860	MAT alpha his3D1 leu2D0 lys2D0 MET15 ura3D0 Nhp6a-iRFP msn2D0 msn4D0 leu2D0::ConS-pHSP12-mCitrine(V163A)-tADH1-Con1-pLEU2-LEU2-Ag_tLEU2 URA3 5' Homology-ConS-pRPL18B-Msn2(S582E S620E S625E S633E)-mScarlet-tADH1-Con1-pRPL18B-Hs_RGS2(33- 67)_13aa-iRFP713 (iRFP)-asLOV2(404-546)-tPGK1-ConE-URA3 (pSc-native-tSc)-URA3 3' Homology-KanR-ColE1	HSP12-mCitrine + Msn2*-dCLASP
yMM1608/pMM1070	MAT alpha his3D1 leu2D0 lys2D0 MET15 ura3D0 Nhp6a-iRFP msn2D0 msn4D0 leu2D0::ConS-pHSP12-mCitrine(V163A)-tADH1-Con1-pLEU2-LEU2-Ag_tLEU2 URA3 5' Homology-ConS-pRPL18B-Zdk1-Msn2(S582E S620E S625E S633E S686D)-mScarlet-yeLANS-tADH1-Con1-pRPL18B-Hs_RGS2(33- 67)_13aa-iRFP713 (iRFP)-asLOV2(404-546)-tPGK1-ConE-URA3 (pSc-native-tSc)-URA3 3' Homology-KanR-ColE1	HSP12-mCitrine + Msn2(D)*-CLASP
yMM1608/pMM1072	MAT alpha his3D1 leu2D0 lys2D0 MET15 ura3D0 Nhp6a-iRFP msn2D0 msn4D0 leu2D0::ConS-pHSP12-mCitrine(V163A)-tADH1-Con1-pLEU2-LEU2-Ag_tLEU2 URA3 5' Homology-ConS-pRPL18B-Msn2(S582E S620E S625E S633E S686D)-mScarlet-tADH1-Con1-pRPL18B-Hs_RGS2(33- 67)_13aa-iRFP713 (iRFP)-asLOV2(404-546)-tPGK1-ConE-URA3 (pSc-native-tSc)-URA3 3' Homology-KanR-ColE1	HSP12-mCitrine + Msn2(D)*-dCLASP
yMM1608/pMM1079	MAT alpha his3D1 leu2D0 lys2D0 MET15 ura3D0 Nhp6a-iRFP msn2D0 msn4D0 leu2D0::ConS-pHSP12-mCitrine(V163A)-tADH1-Con1-pLEU2-LEU2-Ag_tLEU2 URA3 5' Homology-ConS-pRPL18B-Zdk1-Msn2(S582E S620E S625E S633E S671T N672G R674K)-mScarlet-yeLANS-tADH1-Con1-pRPL18B-Hs_RGS2(33- 67)_13aa-iRFP713 (iRFP)-asLOV2(404-546)-tPGK1-ConE-URA3 (pSc-native-tSc)-URA3 3' Homology-KanR-ColE1	HSP12-mCitrine + Msn2(T)*-CLASP
yMM1608/pMM1083	MAT alpha his3D1 leu2D0 lys2D0 MET15 ura3D0 Nhp6a-iRFP msn2D0 msn4D0 leu2D0::ConS-pHSP12-mCitrine(V163A)-tADH1-Con1-pLEU2-LEU2-Ag_tLEU2 URA3 5' Homology-ConS-pRPL18B-Msn2(S582E S620E S625E S633E S671T N672G R674K)-mScarlet-tADH1-Con1-pRPL18B-Hs_RGS2(33- 67)_13aa-iRFP713 (iRFP)-asLOV2(404-546)-tPGK1-ConE-URA3 (pSc-native-tSc)-URA3 3' Homology-KanR-ColE1	HSP12-mCitrine + Msn2(T)*-dCLASP
yMM1620/pMM0845	MAT alpha his3D1 leu2D0 lys2D0 MET15 ura3D0 Nhp6a-iRFP msn2D0 msn4D0 leu2D0::ConS-pSIP18_A4-mCitrine(V163A)-tADH1-Con1-pLEU2-LEU2-Ag_tLEU2 URA3 5' Homology-ConS-pRPL18B-Zdk1-Msn2-mScarlet-yeLANS-tADH1-Con1-pRPL18B-Hs_RGS2(33-67)_13aa-iRFP713 (iRFP)-asLOV2(404-546)-tPGK1-ConE-URA3 (pSc-native-tSc)-URA3 3' Homology-KanR-ColE1	SIP18_A4-mCitrine + Msn2-CLASP
yMM1620/pMM0846	MAT alpha his3D1 leu2D0 lys2D0 MET15 ura3D0 Nhp6a-iRFP msn2D0 msn4D0 leu2D0::ConS-pSIP18_A4-mCitrine(V163A)-tADH1-Con1-pLEU2-LEU2-Ag_tLEU2 URA3 5' Homology-ConS-pRPL18B-Zdk1-Msn2(S582E S620E S625E S633E S686A)-mScarlet-yeLANS-tADH1-Con1-pRPL18B-Hs_RGS2(33-67)_13aa-iRFP713 (iRFP)-asLOV2(404-546)-tPGK1-ConE-URA3 (pSc-native-tSc)-URA3 3' Homology-KanR-ColE1	SIP18_A4-mCitrine + Msn2(A)*-CLASP
yMM1620/pMM0847	MAT alpha his3D1 leu2D0 lys2D0 MET15 ura3D0 Nhp6a-iRFP msn2D0 msn4D0 leu2D0::ConS-pSIP18_A4-mCitrine(V163A)-tADH1-Con1-pLEU2-LEU2-Ag_tLEU2 URA3 5' Homology-ConS-pRPL18B-Zdk1-Msn2(S582E S620E S625E S633E)-mScarlet-yeLANS-tADH1-Con1-pRPL18B-Hs_RGS2(33- 67)_13aa-iRFP713 (iRFP)-asLOV2(404-546)-tPGK1-ConE-URA3 (pSc-native-tSc)-URA3 3' Homology-KanR-ColE1	SIP18_A4-mCitrine + Msn2*-CLASP

yMM1620/pMM0858	MAT alpha his3D1 leu2D0 lys2D0 MET15 ura3D0 Nhp6a-iRFP msn2D0 msn4D0 leu2D0::ConS-pSIP18_A4-mCitrine(V163A)-tADH1-Con1-pLEU2-LEU2-Ag_tLEU2 URA3 5' Homology-ConS-pRPL18B-Msn2-mScarlet-tADH1-Con1-pRPL18B-Hs_RGS2(33- 67)_13aa-iRFP713 (iRFP)-asLOV2(404-546)-tPGK1-ConE-URA3 (pSc-native-tSc)-URA3 3' Homology-KanR-ColE1	SIP18_A4-mCitrine + Msn2-dCLASP
yMM1620/pMM0859	MAT alpha his3D1 leu2D0 lys2D0 MET15 ura3D0 Nhp6a-iRFP msn2D0 msn4D0 leu2D0::ConS-pSIP18_A4-mCitrine(V163A)-tADH1-Con1-pLEU2-LEU2-Ag_tLEU2 URA3 5' Homology-ConS-pRPL18B-Msn2(S582E S620E S625E S633E S686A)-mScarlet-tADH1-Con1-pRPL18B-Hs_RGS2(33- 67)_13aa-iRFP713 (iRFP)-asLOV2(404-546)-tPGK1-ConE-URA3 (pSc-native-tSc)-URA3 3' Homology-KanR-ColE1	SIP18_A4-mCitrine + Msn2(A)*-dCLASP
yMM1620/pMM0860	MAT alpha his3D1 leu2D0 lys2D0 MET15 ura3D0 Nhp6a-iRFP msn2D0 msn4D0 leu2D0::ConS-pSIP18_A4-mCitrine(V163A)-tADH1-Con1-pLEU2-LEU2-Ag_tLEU2 URA3 5' Homology-ConS-pRPL18B-Msn2(S582E S620E S625E S633E)-mScarlet-tADH1-Con1-pRPL18B-Hs_RGS2(33- 67)_13aa-iRFP713 (iRFP)-asLOV2(404-546)-tPGK1-ConE-URA3 (pSc-native-tSc)-URA3 3' Homology-KanR-ColE1	SIP18_A4-mCitrine + Msn2*-dCLASP
yMM1620/pMM1079	MAT alpha his3D1 leu2D0 lys2D0 MET15 ura3D0 Nhp6a-iRFP msn2D0 msn4D0 leu2D0::ConS-pSIP18_A4-mCitrine(V163A)-tADH1-Con1-pLEU2-LEU2-Ag_tLEU2 URA3 5' Homology-ConS-pRPL18B-Zdk1-Msn2(S582E S620E S625E S633E S671T N672G R674K)-mScarlet-yeLANS-tADH1-Con1-pRPL18B-Hs_RGS2(33- 67)_13aa-iRFP713 (iRFP)-asLOV2(404-546)-tPGK1-ConE-URA3 (pSc-native-tSc)-URA3 3' Homology-KanR-ColE1	SIP18_A4-mCitrine + Msn2(T)*-CLASP
yMM1620/pMM1083	MAT alpha his3D1 leu2D0 lys2D0 MET15 ura3D0 Nhp6a-iRFP msn2D0 msn4D0 leu2D0::ConS-pSIP18_A4-mCitrine(V163A)-tADH1-Con1-pLEU2-LEU2-Ag_tLEU2 URA3 5' Homology-ConS-pRPL18B-Msn2(S582E S620E S625E S633E S671T N672G R674K)-mScarlet-tADH1-Con1-pRPL18B-Hs_RGS2(33- 67)_13aa-iRFP713 (iRFP)-asLOV2(404-546)-tPGK1-ConE-URA3 (pSc-native-tSc)-URA3 3' Homology-KanR-ColE1	SIP18_A4-mCitrine + Msn2(T)*-dCLASP
yMM1621/pMM0845	MAT alpha his3D1 leu2D0 lys2D0 MET15 ura3D0 Nhp6a-iRFP msn2D0 msn4D0 leu2D0::ConS-pSIP18_D6-mCitrine(V163A)-tADH1-Con1-pLEU2-LEU2-Ag_tLEU2 URA3 5' Homology-ConS-pRPL18B-Zdk1-Msn2-mScarlet-yeLANS-tADH1-Con1-pRPL18B-Hs_RGS2(33-67)_13aa-iRFP713 (iRFP)-asLOV2(404-546)-tPGK1-ConE-URA3 (pSc-native-tSc)-URA3 3' Homology-KanR-ColE1	SIP18_D6-mCitrine + Msn2-CLASP
yMM1621/pMM0846	MAT alpha his3D1 leu2D0 lys2D0 MET15 ura3D0 Nhp6a-iRFP msn2D0 msn4D0 leu2D0::ConS-pSIP18_D6-mCitrine(V163A)-tADH1-Con1-pLEU2-LEU2-Ag_tLEU2 URA3 5' Homology-ConS-pRPL18B-Zdk1-Msn2(S582E S620E S625E S633E S686A)-mScarlet-yeLANS-tADH1-Con1-pRPL18B-Hs_RGS2(33-67)_13aa-iRFP713 (iRFP)-asLOV2(404-546)-tPGK1-ConE-URA3 (pSc-native-tSc)-URA3 3' Homology-KanR-ColE1	SIP18_D6-mCitrine + Msn2(A)*-CLASP
yMM1621/pMM0847	MAT alpha his3D1 leu2D0 lys2D0 MET15 ura3D0 Nhp6a-iRFP msn2D0 msn4D0 leu2D0::ConS-pSIP18_D6-mCitrine(V163A)-tADH1-Con1-pLEU2-LEU2-Ag_tLEU2 URA3 5' Homology-ConS-pRPL18B-Zdk1-Msn2(S582E S620E S625E S633E)-mScarlet-yeLANS-tADH1-Con1-pRPL18B-Hs_RGS2(33- 67)_13aa-iRFP713 (iRFP)-asLOV2(404-546)-tPGK1-ConE-URA3 (pSc-native-tSc)-URA3 3' Homology-KanR-ColE1	SIP18_D6-mCitrine + Msn2*-CLASP
yMM1621/pMM0858	MAT alpha his3D1 leu2D0 lys2D0 MET15 ura3D0 Nhp6a-iRFP msn2D0 msn4D0 leu2D0::ConS-pSIP18_D6-mCitrine(V163A)-tADH1-Con1-pLEU2-LEU2-Ag_tLEU2 URA3 5' Homology-ConS-pRPL18B-Msn2-mScarlet-tADH1-Con1-pRPL18B-Hs_RGS2(33- 67)_13aa-iRFP713 (iRFP)-asLOV2(404-546)-tPGK1-ConE-URA3 (pSc-native-tSc)-URA3 3' Homology-KanR-ColE1	SIP18_D6-mCitrine + Msn2-dCLASP
yMM1621/pMM0859	MAT alpha his3D1 leu2D0 lys2D0 MET15 ura3D0 Nhp6a-iRFP msn2D0 msn4D0 leu2D0::ConS-pSIP18_D6-mCitrine(V163A)-tADH1-Con1-pLEU2-LEU2-Ag_tLEU2 URA3 5' Homology-ConS-pRPL18B-Msn2(S582E S620E S625E S633E S686A)-mScarlet-tADH1-Con1-pRPL18B-Hs_RGS2(33- 67)_13aa-iRFP713 (iRFP)-asLOV2(404-546)-tPGK1-ConE-URA3 (pSc-native-tSc)-URA3 3' Homology-KanR-ColE1	SIP18_D6-mCitrine + Msn2(A)*-dCLASP
yMM1621/pMM0860	MAT alpha his3D1 leu2D0 lys2D0 MET15 ura3D0 Nhp6a-iRFP msn2D0 msn4D0 leu2D0::ConS-pSIP18_D6-mCitrine(V163A)-tADH1-Con1-pLEU2-LEU2-Ag_tLEU2 URA3 5' Homology-ConS-pRPL18B-Msn2(S582E S620E S625E S633E)-mScarlet-tADH1-Con1-pRPL18B-Hs_RGS2(33- 67)_13aa-iRFP713 (iRFP)-asLOV2(404-546)-tPGK1-ConE-URA3 (pSc-native-tSc)-URA3 3' Homology-KanR-ColE1	SIP18_D6-mCitrine + Msn2*-dCLASP
yMM1621/pMM1079	MAT alpha his3D1 leu2D0 lys2D0 MET15 ura3D0 Nhp6a-iRFP msn2D0 msn4D0 leu2D0::ConS-pSIP18_D6-mCitrine(V163A)-tADH1-Con1-pLEU2-LEU2-Ag_tLEU2 URA3 5' Homology-ConS-pRPL18B-Zdk1-Msn2(S582E S620E S625E S633E S671T N672G R674K)-mScarlet-yeLANS-tADH1-Con1-pRPL18B-Hs_RGS2(33- 67)_13aa-iRFP713 (iRFP)-asLOV2(404-546)-tPGK1-ConE-URA3 (pSc-native-tSc)-URA3 3' Homology-KanR-ColE1	SIP18_D6-mCitrine + Msn2(T)*-CLASP

yMM1621/pMM1083	MAT alpha his3D1 leu2D0 lys2D0 MET15 ura3D0 Nhp6a-iRFP msn2D0 msn4D0 leu2D0::ConS-pSIP18_D6-mCitrine(V163A)-tADH1-Con1-pLEU2-LEU2-Ag_tLEU2 URA3 5' Homology-ConS-pRPL18B-Msn2(S582E S620E S625E S633E S671T N672G R674K)-mScarlet-tADH1-Con1-pRPL18B-Hs_RGS2(33- 67)_13aa-iRFP713 (iRFP)-asLOV2(404-546)-tPGK1-ConE-URA3 (pSc-native-tSc)-URA3 3' Homology-KanR-ColE1	SIP18_D6-mCitrine + Msn2(T)*-dCLASP
yMM1622/pMM0845	MAT alpha his3D1 leu2D0 lys2D0 MET15 ura3D0 Nhp6a-iRFP msn2D0 msn4D0 leu2D0::ConS-pDDR2-mCitrine(V163A)-tADH1-Con1-pLEU2-LEU2-Ag_tLEU2 URA3 5' Homology-ConS-pRPL18B-Zdk1-Msn2-mScarlet-yeLANS-tADH1-Con1-pRPL18B-Hs_RGS2(33-67)_13aa-iRFP713 (iRFP)-asLOV2(404-546)-tPGK1-ConE-URA3 (pSc-native-tSc)-URA3 3' Homology-KanR-ColE1	DDR2-mCitrine + Msn2-CLASP
yMM1622/pMM0846	MAT alpha his3D1 leu2D0 lys2D0 MET15 ura3D0 Nhp6a-iRFP msn2D0 msn4D0 leu2D0::ConS-pDDR2-mCitrine(V163A)-tADH1-Con1-pLEU2-LEU2-Ag_tLEU2 URA3 5' Homology-ConS-pRPL18B-Zdk1-Msn2(S582E S620E S625E S633E S686A)-mScarlet-yeLANS-tADH1-Con1-pRPL18B-Hs_RGS2(33-67)_13aa-iRFP713 (iRFP)-asLOV2(404-546)-tPGK1-ConE-URA3 (pSc-native-tSc)-URA3 3' Homology-KanR-ColE1	DDR2-mCitrine + Msn2(A)*-CLASP
yMM1622/pMM0847	MAT alpha his3D1 leu2D0 lys2D0 MET15 ura3D0 Nhp6a-iRFP msn2D0 msn4D0 leu2D0::ConS-pDDR2-mCitrine(V163A)-tADH1-Con1-pLEU2-LEU2-Ag_tLEU2 URA3 5' Homology-ConS-pRPL18B-Zdk1-Msn2(S582E S620E S625E S633E)-mScarlet-yeLANS-tADH1-Con1-pRPL18B-Hs_RGS2(33- 67)_13aa-iRFP713 (iRFP)-asLOV2(404-546)-tPGK1-ConE-URA3 (pSc-native-tSc)-URA3 3' Homology-KanR-ColE1	DDR2-mCitrine + Msn2*-CLASP
yMM1622/pMM0858	MAT alpha his3D1 leu2D0 lys2D0 MET15 ura3D0 Nhp6a-iRFP msn2D0 msn4D0 leu2D0::ConS-pDDR2-mCitrine(V163A)-tADH1-Con1-pLEU2-LEU2-Ag_tLEU2 URA3 5' Homology-ConS-pRPL18B-Msn2-mScarlet-tADH1-Con1-pRPL18B-Hs_RGS2(33- 67)_13aa-iRFP713 (iRFP)-asLOV2(404-546)-tPGK1-ConE-URA3 (pSc-native-tSc)-URA3 3' Homology-KanR-ColE1	DDR2-mCitrine + Msn2-dCLASP
yMM1622/pMM0859	MAT alpha his3D1 leu2D0 lys2D0 MET15 ura3D0 Nhp6a-iRFP msn2D0 msn4D0 leu2D0::ConS-pDDR2-mCitrine(V163A)-tADH1-Con1-pLEU2-LEU2-Ag_tLEU2 URA3 5' Homology-ConS-pRPL18B-Msn2(S582E S620E S625E S633E S686A)-mScarlet-tADH1-Con1-pRPL18B-Hs_RGS2(33- 67)_13aa-iRFP713 (iRFP)-asLOV2(404-546)-tPGK1-ConE-URA3 (pSc-native-tSc)-URA3 3' Homology-KanR-ColE1	DDR2-mCitrine + Msn2(A)*-dCLASP
yMM1622/pMM0860	MAT alpha his3D1 leu2D0 lys2D0 MET15 ura3D0 Nhp6a-iRFP msn2D0 msn4D0 leu2D0::ConS-pDDR2-mCitrine(V163A)-tADH1-Con1-pLEU2-LEU2-Ag_tLEU2 URA3 5' Homology-ConS-pRPL18B-Msn2(S582E S620E S625E S633E)-mScarlet-tADH1-Con1-pRPL18B-Hs_RGS2(33- 67)_13aa-iRFP713 (iRFP)-asLOV2(404-546)-tPGK1-ConE-URA3 (pSc-native-tSc)-URA3 3' Homology-KanR-ColE1	DDR2-mCitrine + Msn2*-dCLASP
yMM1622/pMM1070	MAT alpha his3D1 leu2D0 lys2D0 MET15 ura3D0 Nhp6a-iRFP msn2D0 msn4D0 leu2D0::ConS-pDDR2-mCitrine(V163A)-tADH1-Con1-pLEU2-LEU2-Ag_tLEU2 URA3 5' Homology-ConS-pRPL18B-Zdk1-Msn2(S582E S620E S625E S633E S686D)-mScarlet-yeLANS-tADH1-Con1-pRPL18B-Hs_RGS2(33- 67)_13aa-iRFP713 (iRFP)-asLOV2(404-546)-tPGK1-ConE-URA3 (pSc-native-tSc)-URA3 3' Homology-KanR-ColE1	DDR2-mCitrine + Msn2(D)*-CLASP
yMM1622/pMM1072	MAT alpha his3D1 leu2D0 lys2D0 MET15 ura3D0 Nhp6a-iRFP msn2D0 msn4D0 leu2D0::ConS-pDDR2-mCitrine(V163A)-tADH1-Con1-pLEU2-LEU2-Ag_tLEU2 URA3 5' Homology-ConS-pRPL18B-Msn2(S582E S620E S625E S633E S686D)-mScarlet-tADH1-Con1-pRPL18B-Hs_RGS2(33- 67)_13aa-iRFP713 (iRFP)-asLOV2(404-546)-tPGK1-ConE-URA3 (pSc-native-tSc)-URA3 3' Homology-KanR-ColE1	DDR2-mCitrine + Msn2(D)*-dCLASP
yMM1622/pMM1079	MAT alpha his3D1 leu2D0 lys2D0 MET15 ura3D0 Nhp6a-iRFP msn2D0 msn4D0 leu2D0::ConS-pDDR2-mCitrine(V163A)-tADH1-Con1-pLEU2-LEU2-Ag_tLEU2 URA3 5' Homology-ConS-pRPL18B-Zdk1-Msn2(S582E S620E S625E S633E S671T N672G R674K)-mScarlet-yeLANS-tADH1-Con1-pRPL18B-Hs_RGS2(33- 67)_13aa-iRFP713 (iRFP)-asLOV2(404-546)-tPGK1-ConE-URA3 (pSc-native-tSc)-URA3 3' Homology-KanR-ColE1	DDR2-mCitrine + Msn2(T)*-CLASP
yMM1622/pMM1083	MAT alpha his3D1 leu2D0 lys2D0 MET15 ura3D0 Nhp6a-iRFP msn2D0 msn4D0 leu2D0::ConS-pDDR2-mCitrine(V163A)-tADH1-Con1-pLEU2-LEU2-Ag_tLEU2 URA3 5' Homology-ConS-pRPL18B-Msn2(S582E S620E S625E S633E S671T N672G R674K)-mScarlet-tADH1-Con1-pRPL18B-Hs_RGS2(33- 67)_13aa-iRFP713 (iRFP)-asLOV2(404-546)-tPGK1-ConE-URA3 (pSc-native-tSc)-URA3 3' Homology-KanR-ColE1	DDR2-mCitrine + Msn2(T)*-dCLASP
yMM1623/pMM0845	MAT alpha his3D1 leu2D0 lys2D0 MET15 ura3D0 Nhp6a-iRFP msn2D0 msn4D0 leu2D0::ConS-pTKL2-mCitrine(V163A)-tADH1-Con1-pLEU2-LEU2-Ag_tLEU2 URA3 5' Homology-ConS-pRPL18B-Zdk1-Msn2-mScarlet-yeLANS-tADH1-Con1-pRPL18B-Hs_RGS2(33-67)_13aa-iRFP713 (iRFP)-asLOV2(404-546)-tPGK1-ConE-URA3 (pSc-native-tSc)-URA3 3' Homology-KanR-ColE1	TKL2-mCitrine + Msn2-CLASP

yMM1623/pMM0846	MAT alpha his3D1 leu2D0 lys2D0 MET15 ura3D0 Nhp6a-iRFP msn2D0 msn4D0 leu2D0::ConS-pTKL2-mCitrine(V163A)-tADH1-Con1-pLEU2-LEU2-Ag_tLEU2 URA3 5' Homology-ConS-pRPL18B-Zdk1-Msn2(S582E S620E S625E S633E S686A)-mScarlet-yeLANS-tADH1-Con1-pRPL18B-Hs_RGS2(33-67)_13aa-iRFP713 (iRFP)-asLOV2(404-546)-tPGK1-ConE-URA3 (pSc-native-tSc)-URA3 3' Homology-KanR-ColE1	TKL2-mCitrine + Msn2(A)*-CLASP
yMM1623/pMM0847	MAT alpha his3D1 leu2D0 lys2D0 MET15 ura3D0 Nhp6a-iRFP msn2D0 msn4D0 leu2D0::ConS-pTKL2-mCitrine(V163A)-tADH1-Con1-pLEU2-LEU2-Ag_tLEU2 URA3 5' Homology-ConS-pRPL18B-Zdk1-Msn2(S582E S620E S625E S633E)-mScarlet-yeLANS-tADH1-Con1-pRPL18B-Hs_RGS2(33- 67)_13aa-iRFP713 (iRFP)-asLOV2(404-546)-tPGK1-ConE-URA3 (pSc-native-tSc)-URA3 3' Homology-KanR-ColE1	TKL2-mCitrine + Msn2*-CLASP
yMM1623/pMM0858	MAT alpha his3D1 leu2D0 lys2D0 MET15 ura3D0 Nhp6a-iRFP msn2D0 msn4D0 leu2D0::ConS-pTKL2-mCitrine(V163A)-tADH1-Con1-pLEU2-LEU2-Ag_tLEU2 URA3 5' Homology-ConS-pRPL18B-Msn2-mScarlet-tADH1-Con1-pRPL18B-Hs_RGS2(33- 67)_13aa-iRFP713 (iRFP)-asLOV2(404-546)-tPGK1-ConE-URA3 (pSc-native-tSc)-URA3 3' Homology-KanR-ColE1	TKL2-mCitrine + Msn2-dCLASP
yMM1623/pMM0859	MAT alpha his3D1 leu2D0 lys2D0 MET15 ura3D0 Nhp6a-iRFP msn2D0 msn4D0 leu2D0::ConS-pTKL2-mCitrine(V163A)-tADH1-Con1-pLEU2-LEU2-Ag_tLEU2 URA3 5' Homology-ConS-pRPL18B-Msn2(S582E S620E S625E S633E S686A)-mScarlet-tADH1-Con1-pRPL18B-Hs_RGS2(33- 67)_13aa-iRFP713 (iRFP)-asLOV2(404-546)-tPGK1-ConE-URA3 (pSc-native-tSc)-URA3 3' Homology-KanR-ColE1	TKL2-mCitrine + Msn2(A)*-dCLASP
yMM1623/pMM0860	MAT alpha his3D1 leu2D0 lys2D0 MET15 ura3D0 Nhp6a-iRFP msn2D0 msn4D0 leu2D0::ConS-pTKL2-mCitrine(V163A)-tADH1-Con1-pLEU2-LEU2-Ag_tLEU2 URA3 5' Homology-ConS-pRPL18B-Msn2(S582E S620E S625E S633E)-mScarlet-tADH1-Con1-pRPL18B-Hs_RGS2(33- 67)_13aa-iRFP713 (iRFP)-asLOV2(404-546)-tPGK1-ConE-URA3 (pSc-native-tSc)-URA3 3' Homology-KanR-ColE1	TKL2-mCitrine + Msn2*-dCLASP
yMM1623/pMM1079	MAT alpha his3D1 leu2D0 lys2D0 MET15 ura3D0 Nhp6a-iRFP msn2D0 msn4D0 leu2D0::ConS-pTKL2-mCitrine(V163A)-tADH1-Con1-pLEU2-LEU2-Ag_tLEU2 URA3 5' Homology-ConS-pRPL18B-Zdk1-Msn2(S582E S620E S625E S633E S671T N672G R674K)-mScarlet-yeLANS-tADH1-Con1-pRPL18B-Hs_RGS2(33- 67)_13aa-iRFP713 (iRFP)-asLOV2(404-546)-tPGK1-ConE-URA3 (pSc-native-tSc)-URA3 3' Homology-KanR-ColE1	TKL2-mCitrine + Msn2(T)*-CLASP
yMM1623/pMM1083	MAT alpha his3D1 leu2D0 lys2D0 MET15 ura3D0 Nhp6a-iRFP msn2D0 msn4D0 leu2D0::ConS-pTKL2-mCitrine(V163A)-tADH1-Con1-pLEU2-LEU2-Ag_tLEU2 URA3 5' Homology-ConS-pRPL18B-Msn2(S582E S620E S625E S633E S671T N672G R674K)-mScarlet-tADH1-Con1-pRPL18B-Hs_RGS2(33- 67)_13aa-iRFP713 (iRFP)-asLOV2(404-546)-tPGK1-ConE-URA3 (pSc-native-tSc)-URA3 3' Homology-KanR-ColE1	TKL2-mCitrine + Msn2(T)*-dCLASP
yMM1624/pMM0845	MAT alpha his3D1 leu2D0 lys2D0 MET15 ura3D0 Nhp6a-iRFP msn2D0 msn4D0 leu2D0::ConS-pALD3-mCitrine(V163A)-tADH1-Con1-pLEU2-LEU2-Ag_tLEU2 URA3 5' Homology-ConS-pRPL18B-Zdk1-Msn2-mScarlet-yeLANS-tADH1-Con1-pRPL18B-Hs_RGS2(33-67)_13aa-iRFP713 (iRFP)-asLOV2(404-546)-tPGK1-ConE-URA3 (pSc-native-tSc)-URA3 3' Homology-KanR-ColE1	ALD3-mCitrine + Msn2-CLASP
yMM1624/pMM0846	MAT alpha his3D1 leu2D0 lys2D0 MET15 ura3D0 Nhp6a-iRFP msn2D0 msn4D0 leu2D0::ConS-pALD3-mCitrine(V163A)-tADH1-Con1-pLEU2-LEU2-Ag_tLEU2 URA3 5' Homology-ConS-pRPL18B-Zdk1-Msn2(S582E S620E S625E S633E S686A)-mScarlet-yeLANS-tADH1-Con1-pRPL18B-Hs_RGS2(33-67)_13aa-iRFP713 (iRFP)-asLOV2(404-546)-tPGK1-ConE-URA3 (pSc-native-tSc)-URA3 3' Homology-KanR-ColE1	ALD3-mCitrine + Msn2(A)*-CLASP
yMM1624/pMM0847	MAT alpha his3D1 leu2D0 lys2D0 MET15 ura3D0 Nhp6a-iRFP msn2D0 msn4D0 leu2D0::ConS-pALD3-mCitrine(V163A)-tADH1-Con1-pLEU2-LEU2-Ag_tLEU2 URA3 5' Homology-ConS-pRPL18B-Zdk1-Msn2(S582E S620E S625E S633E)-mScarlet-yeLANS-tADH1-Con1-pRPL18B-Hs_RGS2(33- 67)_13aa-iRFP713 (iRFP)-asLOV2(404-546)-tPGK1-ConE-URA3 (pSc-native-tSc)-URA3 3' Homology-KanR-ColE1	ALD3-mCitrine + Msn2*-CLASP
yMM1624/pMM0858	MAT alpha his3D1 leu2D0 lys2D0 MET15 ura3D0 Nhp6a-iRFP msn2D0 msn4D0 leu2D0::ConS-pALD3-mCitrine(V163A)-tADH1-Con1-pLEU2-LEU2-Ag_tLEU2 URA3 5' Homology-ConS-pRPL18B-Msn2-mScarlet-tADH1-Con1-pRPL18B-Hs_RGS2(33- 67)_13aa-iRFP713 (iRFP)-asLOV2(404-546)-tPGK1-ConE-URA3 (pSc-native-tSc)-URA3 3' Homology-KanR-ColE1	ALD3-mCitrine + Msn2-dCLASP
yMM1624/pMM0859	MAT alpha his3D1 leu2D0 lys2D0 MET15 ura3D0 Nhp6a-iRFP msn2D0 msn4D0 leu2D0::ConS-pALD3-mCitrine(V163A)-tADH1-Con1-pLEU2-LEU2-Ag_tLEU2 URA3 5' Homology-ConS-pRPL18B-Msn2(S582E S620E S625E S633E S686A)-mScarlet-tADH1-Con1-pRPL18B-Hs_RGS2(33- 67)_13aa-iRFP713 (iRFP)-asLOV2(404-546)-tPGK1-ConE-URA3 (pSc-native-tSc)-URA3 3' Homology-KanR-ColE1	ALD3-mCitrine + Msn2(A)*-dCLASP

yMM1624/pMM0860	MAT alpha his3D1 leu2D0 lys2D0 MET15 ura3D0 Nhp6a-iRFP msn2D0 msn4D0 leu2D0::ConS-pALD3-mCitrine(V163A)-tADH1-Con1-pLEU2-LEU2-Ag_tLEU2 URA3 5' Homology-ConS-pRPL18B-Msn2(S582E S620E S625E S633E)-mScarlet-tADH1-Con1-pRPL18B-Hs_RGS2(33- 67)_13aa-iRFP713 (iRFP)-asLOV2(404-546)-tPGK1-ConE-URA3 (pSc-native-tSc)-URA3 3' Homology-KanR-ColE1	ALD3-mCitrine + Msn2*-dCLASP
yMM1624/pMM1079	MAT alpha his3D1 leu2D0 lys2D0 MET15 ura3D0 Nhp6a-iRFP msn2D0 msn4D0 leu2D0::ConS-pALD3-mCitrine(V163A)-tADH1-Con1-pLEU2-LEU2-Ag_tLEU2 URA3 5' Homology-ConS-pRPL18B-Zdk1-Msn2(S582E S620E S625E S633E S671T N672G R674K)-mScarlet-yeLANS-tADH1-Con1-pRPL18B-Hs_RGS2(33- 67)_13aa-iRFP713 (iRFP)-asLOV2(404-546)-tPGK1-ConE-URA3 (pSc-native-tSc)-URA3 3' Homology-KanR-ColE1	ALD3-mCitrine + Msn2(T)*-CLASP
yMM1624/pMM1083	MAT alpha his3D1 leu2D0 lys2D0 MET15 ura3D0 Nhp6a-iRFP msn2D0 msn4D0 leu2D0::ConS-pALD3-mCitrine(V163A)-tADH1-Con1-pLEU2-LEU2-Ag_tLEU2 URA3 5' Homology-ConS-pRPL18B-Msn2(S582E S620E S625E S633E S671T N672G R674K)-mScarlet-tADH1-Con1-pRPL18B-Hs_RGS2(33- 67)_13aa-iRFP713 (iRFP)-asLOV2(404-546)-tPGK1-ConE-URA3 (pSc-native-tSc)-URA3 3' Homology-KanR-ColE1	ALD3-mCitrine + Msn2(T)*-dCLASP
yMM1625/pMM0845	MAT alpha his3D1 leu2D0 lys2D0 MET15 ura3D0 Nhp6a-iRFP msn2D0 msn4D0 leu2D0::ConS-pRTN2-mCitrine(V163A)-tADH1-Con1-pLEU2-LEU2-Ag_tLEU2 URA3 5' Homology-ConS-pRPL18B-Zdk1-Msn2-mScarlet-yeLANS-tADH1-Con1-pRPL18B-Hs_RGS2(33-67)_13aa-iRFP713 (iRFP)-asLOV2(404-546)-tPGK1-ConE-URA3 (pSc-native-tSc)-URA3 3' Homology-KanR-ColE1	RTN2-mCitrine + Msn2-CLASP
yMM1625/pMM0846	MAT alpha his3D1 leu2D0 lys2D0 MET15 ura3D0 Nhp6a-iRFP msn2D0 msn4D0 leu2D0::ConS-pRTN2-mCitrine(V163A)-tADH1-Con1-pLEU2-LEU2-Ag_tLEU2 URA3 5' Homology-ConS-pRPL18B-Zdk1-Msn2(S582E S620E S625E S633E S686A)-mScarlet-yeLANS-tADH1-Con1-pRPL18B-Hs_RGS2(33-67)_13aa-iRFP713 (iRFP)-asLOV2(404-546)-tPGK1-ConE-URA3 (pSc-native-tSc)-URA3 3' Homology-KanR-ColE1	RTN2-mCitrine + Msn2(A)*-CLASP
yMM1625/pMM0847	MAT alpha his3D1 leu2D0 lys2D0 MET15 ura3D0 Nhp6a-iRFP msn2D0 msn4D0 leu2D0::ConS-pRTN2-mCitrine(V163A)-tADH1-Con1-pLEU2-LEU2-Ag_tLEU2 URA3 5' Homology-ConS-pRPL18B-Zdk1-Msn2(S582E S620E S625E S633E)-mScarlet-yeLANS-tADH1-Con1-pRPL18B-Hs_RGS2(33- 67)_13aa-iRFP713 (iRFP)-asLOV2(404-546)-tPGK1-ConE-URA3 (pSc-native-tSc)-URA3 3' Homology-KanR-ColE1	RTN2-mCitrine + Msn2*-CLASP
yMM1625/pMM0858	MAT alpha his3D1 leu2D0 lys2D0 MET15 ura3D0 Nhp6a-iRFP msn2D0 msn4D0 leu2D0::ConS-pRTN2-mCitrine(V163A)-tADH1-Con1-pLEU2-LEU2-Ag_tLEU2 URA3 5' Homology-ConS-pRPL18B-Msn2-mScarlet-tADH1-Con1-pRPL18B-Hs_RGS2(33- 67)_13aa-iRFP713 (iRFP)-asLOV2(404-546)-tPGK1-ConE-URA3 (pSc-native-tSc)-URA3 3' Homology-KanR-ColE1	RTN2-mCitrine + Msn2-dCLASP
yMM1625/pMM0859	MAT alpha his3D1 leu2D0 lys2D0 MET15 ura3D0 Nhp6a-iRFP msn2D0 msn4D0 leu2D0::ConS-pRTN2-mCitrine(V163A)-tADH1-Con1-pLEU2-LEU2-Ag_tLEU2 URA3 5' Homology-ConS-pRPL18B-Msn2(S582E S620E S625E S633E S686A)-mScarlet-tADH1-Con1-pRPL18B-Hs_RGS2(33- 67)_13aa-iRFP713 (iRFP)-asLOV2(404-546)-tPGK1-ConE-URA3 (pSc-native-tSc)-URA3 3' Homology-KanR-ColE1	RTN2-mCitrine + Msn2(A)*-dCLASP
yMM1625/pMM0860	MAT alpha his3D1 leu2D0 lys2D0 MET15 ura3D0 Nhp6a-iRFP msn2D0 msn4D0 leu2D0::ConS-pRTN2-mCitrine(V163A)-tADH1-Con1-pLEU2-LEU2-Ag_tLEU2 URA3 5' Homology-ConS-pRPL18B-Msn2(S582E S620E S625E S633E)-mScarlet-tADH1-Con1-pRPL18B-Hs_RGS2(33- 67)_13aa-iRFP713 (iRFP)-asLOV2(404-546)-tPGK1-ConE-URA3 (pSc-native-tSc)-URA3 3' Homology-KanR-ColE1	RTN2-mCitrine + Msn2*-dCLASP
yMM1625/pMM1079	MAT alpha his3D1 leu2D0 lys2D0 MET15 ura3D0 Nhp6a-iRFP msn2D0 msn4D0 leu2D0::ConS-pRTN2-mCitrine(V163A)-tADH1-Con1-pLEU2-LEU2-Ag_tLEU2 URA3 5' Homology-ConS-pRPL18B-Zdk1-Msn2(S582E S620E S625E S633E S671T N672G R674K)-mScarlet-yeLANS-tADH1-Con1-pRPL18B-Hs_RGS2(33- 67)_13aa-iRFP713 (iRFP)-asLOV2(404-546)-tPGK1-ConE-URA3 (pSc-native-tSc)-URA3 3' Homology-KanR-ColE1	RTN2-mCitrine + Msn2(T)*-CLASP
yMM1625/pMM1083	MAT alpha his3D1 leu2D0 lys2D0 MET15 ura3D0 Nhp6a-iRFP msn2D0 msn4D0 leu2D0::ConS-pRTN2-mCitrine(V163A)-tADH1-Con1-pLEU2-LEU2-Ag_tLEU2 URA3 5' Homology-ConS-pRPL18B-Msn2(S582E S620E S625E S633E S671T N672G R674K)-mScarlet-tADH1-Con1-pRPL18B-Hs_RGS2(33- 67)_13aa-iRFP713 (iRFP)-asLOV2(404-546)-tPGK1-ConE-URA3 (pSc-native-tSc)-URA3 3' Homology-KanR-ColE1	RTN2-mCitrine + Msn2(T)*-dCLASP

A.6 Quantifying yeast colony growth from images of plates

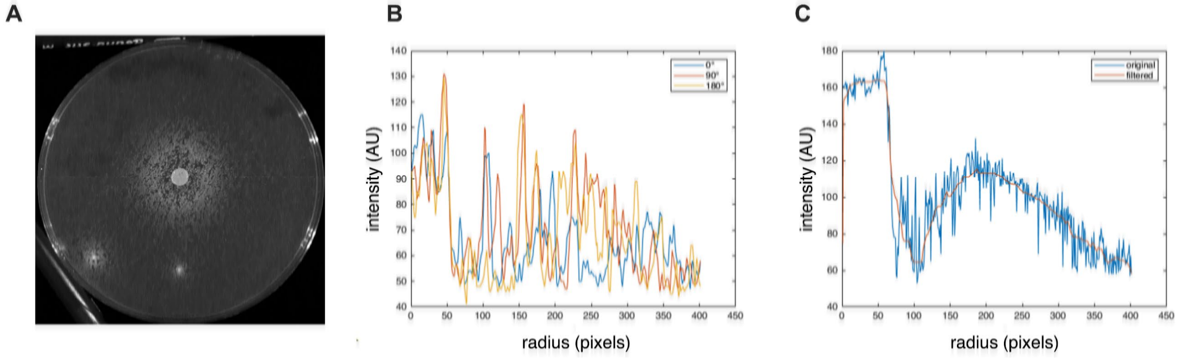

Figure A.6.1 Yeast colony growth and intensity profiles. (**A**) Yeast growing on a petri dish featuring a dense central spot, sparsely populated valley, and outer ring. (**B**) Noisy intensity profiles of individual angular slices through the central spot. (**C**) Composite intensity profile generated by a clock-scan, both raw (blue) and filtered (orange).

Another member of the McClean Lab, Neydis Moreno Morales, was interested in how cooperativity and the availability of nutrients shape the growth of yeast on plates. In her experiments, yeast tended to form a dense central spot surrounded by a region of sparse colony growth (a valley) and an outer ring of moderate colony growth (Figure A.6.1A). She wanted to quantify the boundaries of these regions from images, but the boundaries shifted based on experimental conditions and were often ill-defined. Having some experience in image analysis, I decided to give the problem a try. One option was to plot the intensity of angular slices through the central spot and try to extract features (region boundaries) from the resulting intensity profiles, but individual angular slices were usually too noisy to be useful (Figure A.6.1B). Another option was to extract features from the composite intensity profile given by a clock-scan [116], which calculates the average pixel intensity versus radius for all angular slices (Figure A.6.1C). However, this discarded a lot of information, provided only one intensity profile from which to extract features, and gave no indication of or well- or ill-defined the region boundaries were. I therefore decided to try a bootstrap-based approach in MATLAB to repeatedly identify potential features from randomly selected sets of angular slices and then select the most frequently identified potential features as true features.

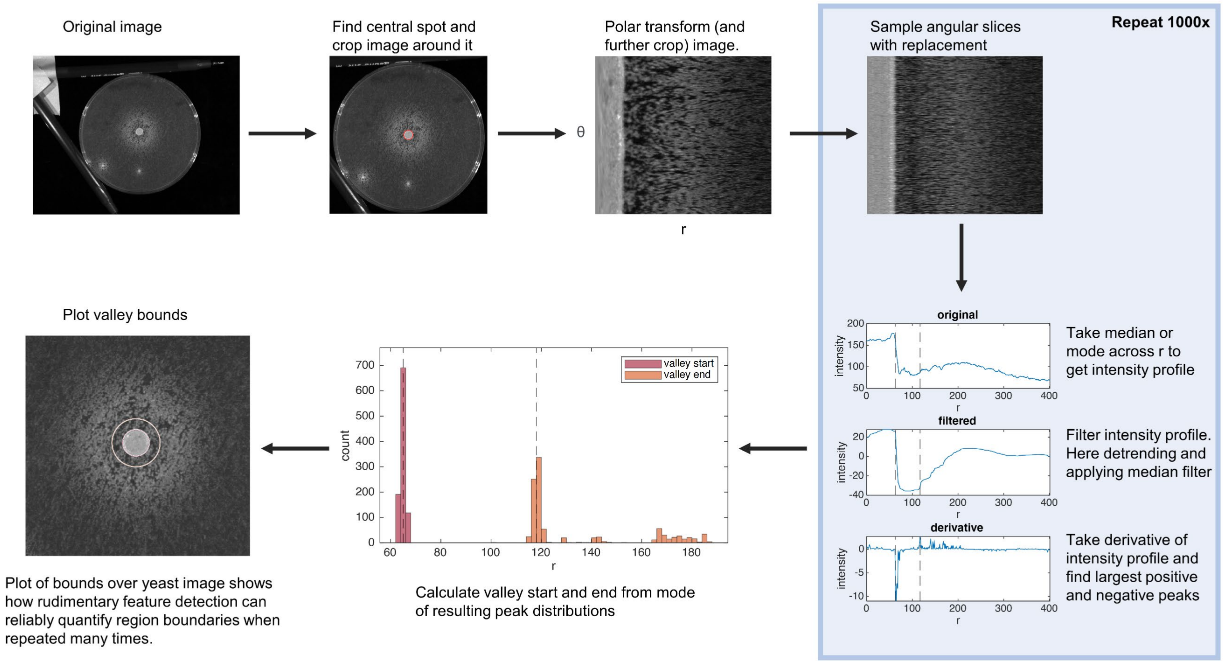

Figure A.6.2 Overview of automated method for quantifying yeast colony growth. A schematic depicting a simple approach for identifying features from bootstrapped composite slices, though more complex feature identification techniques (for example, curve fitting) could also be used.

As shown in Figure A.6.2, this process starts by roughly identifying the central yeast spot using MATLAB’s circle finder and cropping the image around this spot. A polar transformation is then applied to create a polar image where each row of pixels corresponds to an angular slice through the plate. The angular slices are then sampled with replacement to construct composite images from which intensity profiles are generated by taking the median intensity value at each radius. The intensity profile is filtered and features are identified from the resulting signal. For example, potential valley bounds can be identified as the locations where the derivative of the filtered intensity profile is at its maximum and minimum. This process is repeated many times to create distributions of potential features. True features are then selected as the mode of these distributions; confidence intervals showing how well- or ill-defined each feature is can also be calculated from the distributions. Since all features lie on roughly the same plane, it is also possible to identify the outer edges of the plate (which is 100 mm across) and convert the feature measurements to physical units. This approach was published with Neydis' research [117].

A.7 Biological signal generators

This section was adapted from the following review article:

T. D. Scott*, K. Sweeney*, and M. N. McClean, “Biological signal generators: integrating synthetic biology tools and in silico control,” *Curr. Opin. Syst. Biol.*, vol. 14, pp. 58–65, Feb. 2019. (

*These authors contributed equally

A.7.1 Abstract

Biological networks sense extracellular stimuli and generate appropriate outputs within the cell that determine cellular response. Biological signal generators are becoming an important tool for understanding how information is transmitted in these networks and controlling network behavior. Signal generators produce well-defined, dynamic, intracellular signals of important network components, such as kinase activity or the concentration of a specific transcription factor. Synthetic biology tools coupled with *in silico* control have enabled the construction of these sophisticated biological signal generators. Here we review recent advances in biological signal generator construction and their use in systems biology studies. Challenges for constructing signal generators for a wider range of biological networks and generalizing their use are discussed.

A.7.2 Introduction

Biological networks consist of interacting components that regulate one another through post-translational modifications, regulation of transcription, and other mechanisms (Figure A.7.1). Advances in reporting and imaging technologies have allowed us to see multiple steps in the transmission of information through the cell as external stimuli are processed into intracellular responses. It is now apparent that biological components encode information in many ways, including in both the amplitude and the dynamics of their activity [7], [118]–[121]. This is akin to the processing of information by electrical circuits, which take input signals and convert them to output signals to achieve a desired outcome and where information is encoded in both the frequency and amplitude of the signal. Electrical engineers use signal generators, which create programmable signals such as voltage waves, to understand the importance of specific electrical signals and unravel the function of components and subcircuits. Until recently, biologists have had no equivalent tool for probing biological networks.

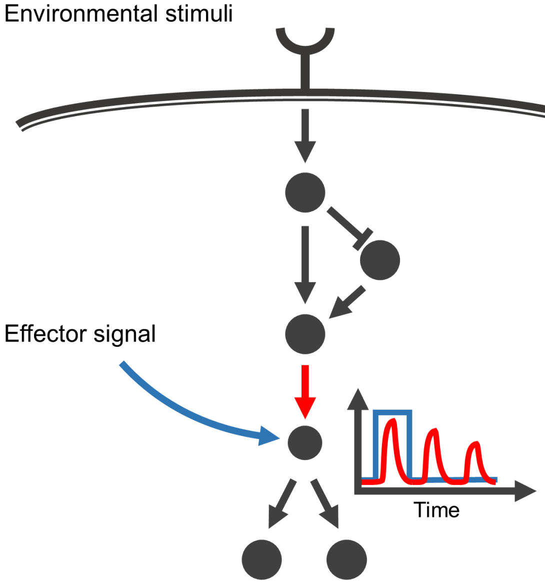

Figure A.7.1 Schematic depiction of a biological network. Biological networks, such as the cartoon network shown here, sense extracellular stimuli and convert those stimuli into appropriate intracellular responses. The network transforms a signal and information is encoded in the dynamics and amplitude of component activity (*e.g.* red signal). A biological signal generator can bypass the upstream network to produce controllable levels of component activity (*e.g.* blue signal) making it possible to dissect how information is transmitted or to control specific desirable responses.

A.7.3 Components of a biological signal generator

An electronic signal generator generates electronic signals specified by a user. In much the same way, a biological signal generator should produce a desired intracellular signal (such as kinase activity or transcription factor (TF) concentration) specified by a user (Figure A.7.2A). The basic components of a biological signal generator include a controller, plant, and sensor (Figure A.7.2B)**.** Some, or all, of these components might be needed in order to get the desired range of signals from the biological signal generator. A critical component of a biological signal generator is the biological **plant**, which is controlled to produce the desired output signal. For example, the plant might be a chemically-inducible promoter that drives expression of a TF, whose concentration is the desired output. Some early biological signal generators consisted of nothing more than the plant and offered only limited precision or control. In our example, chemical inducer might be added to induce the promoter and dramatically overexpress the desired TF.

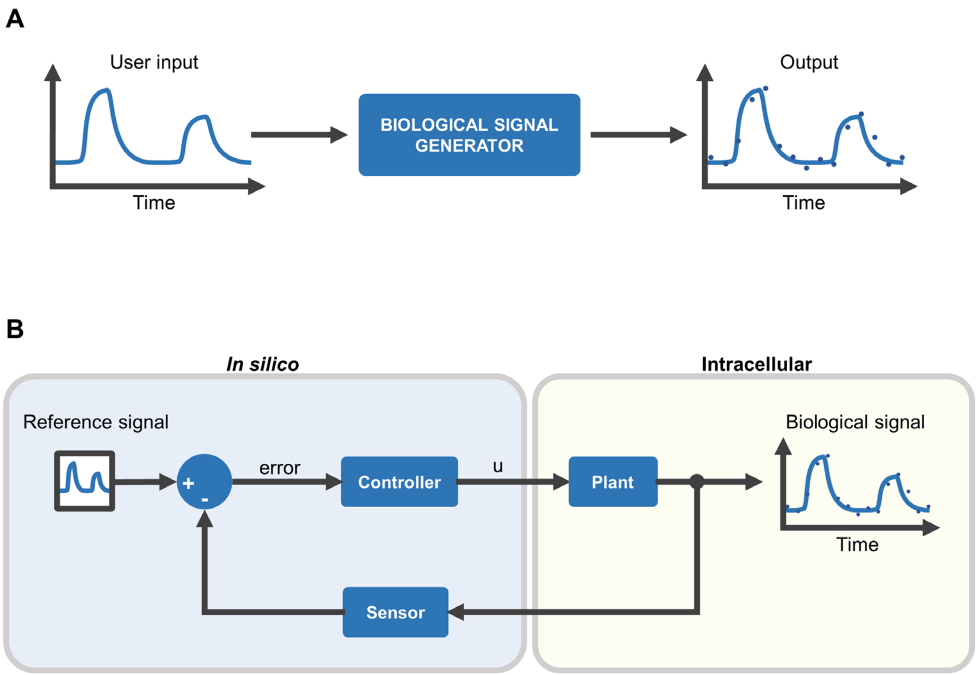

Figure A.7.2 Components of a biological signal generator. (**A**) A biological signal generate converts an input signal to an intracellular output signal. (**B**) Schematic depiction showing the components of a biological signal generator.

More sophisticated signals can be generated by developing a control scheme for the plant. A controller can send an effector signal (u) to the plant (in our example, u is the amount of chemical inducer) to achieve a desired biological signal, namely, the user-defined **reference signal**. If the output of the biological signal generator has no influence on the effector signal, this is called **open-**

loop control. Open-loop control schemes *can* be very effective [122], [123] when coupled with accurate models of the biological plant that allow appropriate effector signals to be designed. However, because the output of the biological signal generator is not fed-back to control the effector signal these types of controllers cannot compensate for changes in the plant with time nor reject unexpected disturbances. **Closed-loop,** or feedback, control schemes can compensate for these biological changes by using the output of the biological signal generator to determine the effector signal. In a closed-loop control scheme the output is measured by a sensor and compared to a user-defined desired output to create an error signal, which is fed into a controller that determines the effector signal that will best drive the plant towards producing the desired output signal.

In principle, a biological signal generator can be implemented entirely within a cell. For example, regulators (signal generators that keep their output at a constant level) have been implemented using entirely *intracellular* components [124]–[126]. However, biological signal generators capable of producing more complicated output signals commonly consist of an intracellular biological plant with *extracellular in silico* implementation of the controller and sensing (Figure A.7.2B).

A.7.4 The importance of biological signal generators

Standard static perturbations of biological networks (such as gene knockouts or knockdowns) yield information about the identity of components in a biological network but lack kinetic information. Step-shocks such as rapid overexpression, have been theoretically and experimentally shown to be inferior to time-varying inputs, such as oscillations, for identifying network components, protein interactions, and kinetic properties [127], [128]. Additionally, step responses can be insufficient for characterizing networks containing feedback or feed-forward loops [129]–[131]. There has been extensive research in engineering and systems biology devoted to the design of optimal stimuli for discrimination between models of complex systems [128], [132]. However, without a biological signal generator capable of producing complex time-varying signals the application of these tools to unraveling biological networks is limited. In synthetic biology applications, biological signal generators have the potential to dramatically improve the design process by allowing the behavior of individual biological components or genetic circuits to be well characterized over a range of inputs [122], [133]. Additionally, fine-tuning and control of biological networks for applications in biotechnology or biomedicine requires the ability to dynamically program component activity in the network. Recent advances in synthetic biology and *in silico* control have started to allow the creation of the necessary biological signal generators for these and other applications.

A.7.5 Synthetic biology tools for biological signal generators

Conditional systems for modulating protein function are common research tools in the biological sciences [134]. Often these systems work by controlling protein concentration, as in systems where a ligand-responsive transcriptional activator or repressor acts on a specific promoter to control the expression and subsequent production of a protein of interest. Biological signal generators of protein function can be built around these conditional systems by using appropriate instrumentation and controllers to drive the ligand-effector signal that generates output from the conditional system, or biological **plant**. Control strategies often require development of predictive mathematical models to describe how the conditional system responds to the effector.

Many conditional systems employ promoters naturally regulated by nutrients or stress. One of the first examples of a closed-loop biological signal generator utilized a stress-responsive promoter and osmotic stress to drive gene expression in yeast [135]. Similar controllers have been built utilizing control of nutrient-responsive promoters [136], [137]. However, nutrients and stress regulate many processes within the cell, making them less-than-ideal effectors. Significant effort in synthetic biology has focused on designing chemically-inducible “orthogonal” conditional systems that interact minimally with existing cellular regulation and machinery [31], [138]–[140]. These orthogonal induction systems are well suited for constructing signal generators. Fracassi *et al* used an orthogonal Tet-responsive promoter to drive an intracellular protein concentration signal in mammalian cells [141]. As the toolkit of orthogonal conditional systems continues to expand new possibilities are emerging for designing biological signal generators. For example, recent development of modular CRISPRi technologies have enabled the activation or repression of multiple orthogonal promoters simultaneously [142], [143]. Systems that regulate protein function rather than protein concentration are also possible. The O’Shea group created a biological signal generator using an analog-sensitive version of protein kinase A (PKA). By controlling PKA-activity and therefore downstream signals of TF activity they were able to determine how the amplitude, frequency, and duration of TF activity encoded differential gene expression [7].

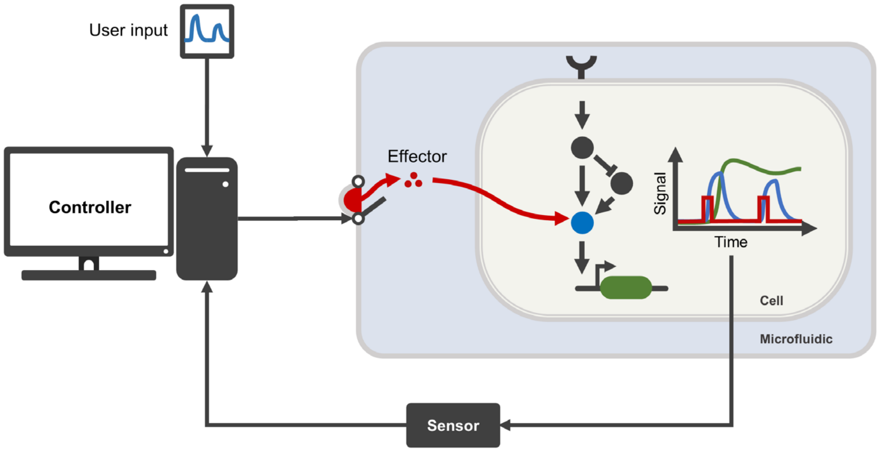

Figure A.7.3 Schematic depiction of a biological signal generator. In this cartoon system, a computer controls a microfluidic device to deliver an effector molecule (red) that drives the activity of a cellular signaling component (blue) to match a user-specified input signal. The effect of this perturbation on downstream gene expression (green) is subsequently measured and used to control the effector concentration.

Biological signal generators built around chemically-regulated biological plants have used microfluidic technology to control the effector signal (Figure A.7.3) [7], [137], [141], [144]. Microfluidic devices allow for fast, time-varying effector signals due to the small volumes of media in play. However, there are limitations. Most microfluidic devices allow for only small amounts of cell culture and cell material is difficult to recover from the device, often limiting downstream assays to single-cell imaging of fluorescent reporters (though see Lane, *et al* [31]). An alternative to chemical effectors is to drive the plant using light effectors (optogenetics). Light presents some advantages over chemical effectors because its wavelength, intensity, temporal duration, and spatial dimension can be precisely controlled in cultures of cells. Synthetic biology advances have created optogenetic tools effective for controlling a variety of cellular processes, from gene regulation to protein localization [37], [38], [145], [146]. The optogenetic toolkit continues to expand and efforts are in progress to make technology for building light-responsive biological plants and the necessary light-control hardware more accessible [56], [59]. Optogenetics has been used as an effector in large culture vessels because light can be more quickly added and removed than a chemical [64], [95], [122]. One of the first demonstrations of *in silico* feedback control to create a biological signal generator of protein concentration used a light-responsive promoter to drive gene expression in cultures of yeast [147]. Subsequent powerful examples of optogenetic signal generators include a regulator for maintaining protein concentration in chemostat cultures of microbes [64], a biological signal generator for characterizing a synthetic inverter gene circuit in *E. coli* [133], a high-throughput kinase activity generator in mammalian cell cultures [121], and single-cell level control of gene expression in a population of *E. coli* [148].

A.7.6 *In silico* controllers for biological signal generators

In some of the simplest biological signal generators, the output of the biological plant is assumed to directly follow this effector signal—the effector signal is turned on when output is desired and turned off when it is not. For systems in which the plant responds rapidly and faithfully to the effector signal, this can be an effective approach [7], [120], [121], [144]. However, many biological plants are affected by interactions with the cellular milieu, including feedback due to stress and resource limitation [124]. Additionally, delays and waveform differences between the effector signal and plant output often need to be considered [64]. In these cases, a more sophisticated controller is required to design an appropriate effector signal.

Open-loop control strategies use a model of the biological plant to design effector signals that lead to the desired output [122], [137]. Characterization of an appropriate model requires measuring the relationship between effector input and plant output (the **input/output relationship**) and fitting a model that can describe this behavior over a wide-enough range of conditions [133]. An alternative to open-loop control is closed-loop control, where the error between the actual and desired output of the plant is used to determine the effector signal. Unlike open-loop controllers, closed-loop controllers can compensate for unexpected disturbances (such as those caused by environmental fluctuations) in a process known as **disturbance rejection**. The majority of biological signal generators that have been implemented to date and that are capable of generating complex signals such as ramps and oscillations utilize closed-loop control [136], [137], [141], [147], [149], [150]. However, utilizing a predictive photoconversion model of the optogenetic biological plants, Olson and colleagues were able to generate sophisticated signals in *E. coli* gene expression using open-loop control [123].

One of the simplest forms of closed-loop control is bang-bang control. In bang-bang control, the effector signal is turned on when the actual output falls below the desired output and turned off when the actual output rises above the desired output. This kind of controller is easy to implement and has successfully been used to create biological signal generators around slowly changing biological plants [64]. However, bang-bang controllers tend to oscillate around the desired output, particularly when there is a lag between the effector signal and the output response**.** Proportional-integral-derivative (PID) controllers are widely used in industrial control systems and have been successfully implemented in biological signal generators [137], [147]. PID controllers apply correction based on the proportional, integral, and derivative terms of the error signal. Compared to bang-bang controllers they take account of much more information, including changes in the error with time. More sophisticated controllers are also possible. For example, model predictive control (MPC) relies on a dynamic model of the underlying biological plant, often an empirical model obtained from **system identification** techniques, to design an effector signal. Model predictive control has been used to build biological protein signal generators and control processes such as cell growth [135], [137], [141], [147]. MPC can anticipate future events using the underlying model and thus usually provide more accurate signal generator output as well as better disturbance rejection, at the cost of additional computational expense.

A.7.7 Insights gained from biological signal generators

Biological signal generators can be used to input complex intracellular signals into a network of interest (Figure A.7.4) to gain biological insight. An important aspect of biological networks is how they transmit and transform intracellular signals. Dynamic intracellular signals, such as pulses in kinase and transcription factor activity, are known to carry information and generate distinct downstream responses [7], [22], [120], [151]. These dynamic signals can be transformed by subnetworks within the cell with important consequences for cellular response. For example, linear enzymatic cascades often function as low pass filters, integrating high frequency signals and transmitting lower frequency signals with high fidelity [144], [152].

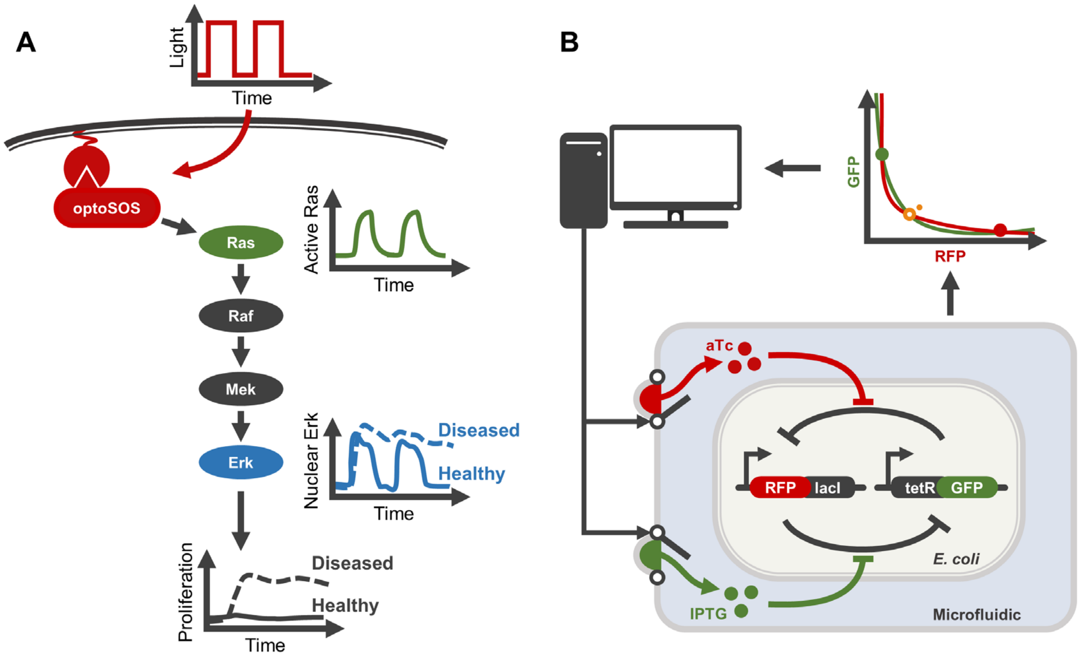

Figure A.7.4 Signal generators can be used to gain insight into biological systems. (**A**) In Bugaj, et al [121], a biological signal generator was used to drive waves of Ras activity and measure how normal and diseased Ras-ERK cascades transmitted that activity. Diseased networks transmitted the signal with less fidelity, leading to hyperactivity of ERK and incorrect interpretation of normally non-proliferative signals. **(B)** Signal generators can also be used to maintain biological systems in a desirable state. Lugagne, et al [153] used a biological signal generator to control the concentration of two repressors in a bistable toggle switch. By pulsing the concentration of the repressors the authors were able to maintain the toggle switch near its unstable state (orange), a state that could not be obtained without dynamic control.

The Ras-ERK pathway regulates important cellular decisions such as proliferation and is known to function as a low-pass filter of Ras-activity with a specific bandwidth [152]. Recently, Bugaj, *et al* [121] utilized a biological signal generator of Ras activity to examine how cancer mutations disrupt this property in the Ras-Erk pathway (Figure A.7.4A). They use the Opto-SOS optogenetic system [145], [152] to drive different frequency signals of Ras activity and observe the filtering properties of the Ras-ERK cascade. They found that filtering activity is altered in a lung cancer cell line (H1395) leading to low-fidelity activation in cancer cells at frequencies where normal cells transmit the signal faithfully. This led to abnormally high Erk output and aberrant cell-cycle entry in response to otherwise non-proliferative pulsatile inputs. This example shows that biological signal generators can give valuable insight into how alteration of signaling dynamics drives disease.

Harrigan, *et al* [154] recently used a biological signal generator to determine the requirements for dynamic feedback regulation in the *S. cerevisiae* mating pathway. Signaling cascades are tightly regulated by factors which prevent the pathway from over- or under-activating. In response to mating pheromone, a MAPK cascade in haploid yeast drives expression of genes needed for mating as well as repressors of upstream signaling to downregulate the pathway. Harrigan, *et al* used a biological signal generator with an optogenetically controlled biological plant driving protein concentration of three regulators of the *S. cerevisiae* mating pathway: *SST2*, *MSG5*, or *GPA1*. Their closed-loop optogenetic control (CLOC) system continuously sampled and measured mating pathway output (using a fluorescent reporter and flow cytometry) and tuned output from the biological signal generator (i.e. regulator concentration) to achieve the expected wild-type mating pathway dynamics. Using this scheme they were able to determine the necessary dynamics of the three critical regulators. They found that while static induction of SST2 can rescue the wild-type phenotype, dynamic control of MSG5 and GPA1 is required to rescue the defect in mating pathway regulation caused by knocking out these genes. This result, which could not be obtained using classical over- or under-expression experiments, highlights the utility of a biological signal generator for studying inherently dynamic cellular processes.

The signals generated by biological signal generators can themselves be used to control additional biological processes. Metabolic engineering is one area where there is significant potential for this kind of control. Organisms can be engineered with exogenous enzymes to produce valuable products such as drugs and fuels. However, the pathways engineered to synthesize these products divert resources and sometimes generate toxic intermediates, causing a burden on cell growth. Recently, Zhao, *et al* [95] used an optogenetic biological signal generator to control the concentration of metabolic enzymes in yeast engineered to produce isobutanol. By using the signal generator to regulate the concentration of enzymes shunting pyruvate through the natural metabolic pathway versus the engineered pathway they were able to design a signal that maximized isobutanol production by optimizing the trade-off between cell growth and production. Thus, the biological signal generator allowed researchers to balance the metabolic needs of the cells with production of a desirable product.

Another exciting aspect of biological signal generators is that they can be used to design dynamic control schemes that force cells to access cellular regimes that are not normally possible. Lugagne *et al* [153] used a biological signal generator to control the concentration of two repressors (lacI, tetR) involved in a bistable genetic toggle switch engineered in *E. coli* (Figure A.7.4B). By designing an appropriate output from the biological signal generator they were able to maintain the bistable genetic toggle switch near its unstable equilibrium, a state it could normally never maintain due to biological noise. This ability could find relevant applications in driving cellular decision-making, controlling cell fate, and understanding differentiation dynamics.

A.7.8 Conclusions and Perspectives

Recent advances show the potential of biological signal generator technology for elucidating and controlling biological networks. Though powerful, current limitations prevent this technology from being widely adopted. Most biological signal generators have been implemented in yeast, *E. coli*, or common mammalian cell lines, systems which have received the vast amount of synthetic biology development and for which many biological “plants” already exist. Further development of orthogonal conditional systems is necessary to allow more biological signal generators to be developed. Additionally, most biological plants used in biological signal generators manipulate protein concentration. Tools that allow protein activity and localization to be controlled would allow more varied intracellular signals to be generated. The measurement technology needed for closed-loop control also limits biological signal generator implementation. Sensors that allow real-time assessment of diverse cellular processes, such as gene expression and metabolism, could allow more sophisticated signal generators to be constructed.

Future work should also focus on democratizing biological signal generators. Biological signal generator construction has thus far required expertise in synthetic biology, control theory, and laboratory automation. This presents a barrier for many systems biologists. Open-source microfluidics or optogenetics hardware combined with controllers designed to allow biologists to implement control algorithms around their biological plant could allow many more laboratories to adopt this technology.

Ultimately, systems biology will be well-served by having the equivalent of an electrical engineer’s signal generator. It remains to be seen what biological discoveries and applications will be enabled by this technology.

A.7.9 Glossary

Input/Output Relationship (I/O): An input-output relationship describes the output of a circuit or biological network in response to specific inputs. I/O relationships are critical for developing models that can be used to design controllers.

Open-loop control: In open-loop control, also called non-feedback control, the control action or effector signal from the controller is independent of the actual output of the plant that is being controlled.

Closed-loop control: In closed-loop control, also called feedback control, at least part of the effector signal is determined by the output of the plant. Closed-loop systems are designed to automatically achieve and maintain the desired output by comparing the actual output with the desired output to create an error signal that is used by the controller to adjust the effector signal.

Disturbance rejection: Disturbance refers to unwanted inputs that affect the control system's output. Disturbance rejection is the (partial) elimination of the effects of these disturbances through an appropriate control scheme. Disturbance rejection is a possible feature of closed-loop control strategies.

System identification: The process of determining an appropriate model for the system under control based on experimental data.

Plant: The system under control is known as the plant. For example, the thermostat in your home controls the furnace (**plant**) such that a desired temperature is maintained.

Effector: In this article, we define an effector to be the component that regulates the biological plant. In a biological signal generator, the effector signal is determined by the controller and appropriate hardware and instrumentation is used to deliver the effector signal to the biological plant.

Bandwidth: Bandwidth determines how much information can be transmitted through a signaling pathway per unit time. The larger the bandwidth of a biological network, the more faithfully it can follow a rapidly varying input signal

Reference Signal: The reference signal is the user-defined setpoint for the system under control (*i.e.* the **plant**). The controller attempts to drive the plant such that the system output matches the reference signal, which may vary in time.

References

[1] J. H. Levine, Y. Lin, and M. B. Elowitz, “Functional Roles of Pulsing in Genetic Circuits,” *Science (80-.).*, vol. 342, no. 6163, pp. 1193–1200, Dec. 2013.

[2] S. L. Werner, D. Barken, and A. Hoffmann, “Stimulus specificity of gene expression programs determined by temporal control of IKK activity,” *Science (80-.).*, vol. 309, no. 5742, pp. 1857–1861, 2005.

[3] F. Christian, E. L. Smith, and R. J. Carmody, “The regulation of NF-κB Subunits by Phosphorylation,” *Cells*, vol. 5, no. 1, 2016.

[4] J. E. Purvis, K. W. Karhohs, C. Mock, E. Batchelor, A. Loewer, and G. Lahav, “P53 Dynamics Control Cell Fate,” *Science (80-.).*, vol. 336, no. 6087, pp. 1440–1444, 2012.

[5] A. Hafner, M. L. Bulyk, A. Jambhekar, and G. Lahav, “The multiple mechanisms that regulate p53 activity and cell fate,” *Nature Reviews Molecular Cell Biology*, vol. 20, no. 4. Springer US, pp. 199–210, 2019.

[6] N. Hao and E. K. O’Shea, “Signal-dependent dynamics of transcription factor translocation controls gene expression,” *Nat. Struct. Mol. Biol.*, vol. 19, no. 1, pp. 31–40, 2012.

[7] A. S. Hansen and E. K. O’Shea, “Promoter decoding of transcription factor dynamics involves a trade-off between noise and control of gene expression,” *Mol. Syst. Biol.*, vol. 9, no. 1, p. 704, Jan. 2013.

[8] A. S. Hansen and E. K. O’Shea, “Cis Determinants of Promoter Threshold and Activation Timescale,” *Cell Rep.*, vol. 12, no. 8, pp. 1226–1233, 2015.

[9] A. S. Hansen and E. K. O’Shea, “Limits on information transduction through amplitude and frequency regulation of transcription factor activity,” *Elife*, vol. 4, no. MAY, pp. 1–19, 2015.

[10] P. Lee, B.-R. Cho, H.-S. Joo, and J.-S. Hahn, “Yeast Yak1 kinase, a bridge between PKA and stress-responsive transcription factors, Hsf1 and Msn2/Msn4,” *Mol. Microbiol.*, vol. 14, no. 1, pp. 302–312, Nov. 2008.

[11] Y. W. Chang, S. C. Howard, and P. K. Herman, “The Ras/PKA signaling pathway directly targets the Srb9 protein, a component of the general RNA polymerase II transcription apparatus,” *Mol. Cell*, vol. 15, no. 1, pp. 107–116, 2004.

[12] D. Pincus, A. Aranda-díaz, I. A. Zuleta, P. Walter, and H. El-samad, “Delayed Ras / PKA signaling augments the unfolded protein response,” vol. 111, no. 41, 2014.

[13] M. Csete and J. Doyle, “Bow ties, metabolism and disease,” *Trends Biotechnol.*, vol. 22, no. 9, pp. 446–450, 2004.

[14] S. Y. Chen *et al.*, “Optogenetic Control Reveals Differential Promoter Interpretation of Transcription Factor Nuclear Translocation Dynamics,” *Cell Syst.*, vol. 11, no. 4, pp. 336-353.e24, 2020.

[15] L. Cai, C. K. Dalal, and M. B. Elowitz, “Frequency-modulated nuclear localization bursts coordinate gene regulation,” *Nature*, vol. 455, no. 7212, pp. 485–490, 2008.

[16] A. P. Gasch *et al.*, “Genomic Expression Programs in the Response of Yeast Cells to Environmental Changes,” *Mol. Biol. Cell*, vol. 11, no. 12, pp. 4241–4257, Dec. 2000.

[17] N. Petrenko, R. V. Chereji, M. N. McClean, A. V. Morozov, and J. R. Broach, “Noise and interlocking signaling pathways promote distinct transcription factor dynamics in response to different stresses,” *Mol. Biol. Cell*, vol. 24, no. 12, pp. 2045–2057, 2013.

[18] W. Görner *et al.*, “Nuclear localization of the C2H2 zinc finger protein Msn2p is regulated by stress and protein kinase A activity,” *Genes Dev.*, vol. 12, no. 4, pp. 586–597, 1998.

[19] C. K. Dalal, L. Cai, Y. Lin, K. Rahbar, and M. B. Elowitz, “Pulsatile dynamics in the yeast proteome,” *Curr. Biol.*, vol. 24, no. 18, pp. 2189–2194, 2014.

[20] S. Tay, J. J. Hughey, T. K. Lee, T. Lipniacki, S. R. Quake, and M. W. Covert, “Single-cell NF-κB dynamics reveal digital activation and analogue information processing,” *Nature*, vol. 466, no. 7303, pp. 267–271, Jul. 2010.

[21] N. Yissachar *et al.*, “Short Article Dynamic Response Diversity of NFAT Isoforms in Individual Living Cells,” *Mol. Cell*, vol. 49, no. 2, pp. 322–330, 2013.

[22] E. Batchelor, A. Loewer, C. Mock, and G. Lahav, “Stimulus-dependent dynamics of p53 in single cells,” *Mol. Syst. Biol.*, vol. 7, no. 1, p. 488, Jan. 2011.

[23] R. E. C. Lee, S. R. Walker, K. Savery, D. A. Frank, and S. Gaudet, “Fold change of nuclear NF-κB determines TNF-induced transcription in single cells,” *Mol. Cell*, vol. 53, no. 6, pp. 867–879, 2014.

[24] S. Sen, Z. Cheng, K. M. Sheu, Y. H. Chen, and A. Hoffmann, “Gene Regulatory Strategies that Decode the Duration of NFκB Dynamics Contribute to LPS- versus TNF-Specific Gene Expression,” *Cell Syst.*, vol. 10, no. 2, pp. 169-182.e5, 2020.

[25] Q. J. Cheng *et al.*, “NF-κB dynamics determine the stimulus specificity of epigenomic reprogramming in macrophages,” *Science (80-.).*, vol. 372, no. 6548, pp. 1349–1353, 2021.

[26] G. Lahav *et al.*, “Dynamics of the p53-Mdm2 feedback loop in individual cells,” vol. 36, no. 2, pp. 147–150, 2004.

[27] M. D. Harton, W. S. Koh, A. D. Bunker, A. Singh, and E. Batchelor, “p53 pulse modulation differentially regulates target gene promoters to regulate cell fate decisions,” *Mol. Syst. Biol.*, vol. 15, no. 9, pp. 1–15, Sep. 2019.

[28] J. Stewart-Ornstein *et al.*, “p53 dynamics vary between tissues and are linked with radiation sensitivity,” *Nat. Commun.*, vol. 12, no. 1, 2021.

[29] Y. Lin, C. H. Sohn, C. K. Dalal, L. Cai, and M. B. Elowitz, “Combinatorial gene regulation by modulation of relative pulse timing,” *Nature*, vol. 527, no. 7576, pp. 54–58, 2015.

[30] Y. Wu, J. Wu, M. Deng, and Y. Lin, “Yeast cell fate control by temporal redundancy modulation of transcription factor paralogs,” *Nat. Commun.*, vol. 12, no. 1, pp. 1–13, 2021.

[31] K. Lane *et al.*, “Measuring Signaling and RNA-Seq in the Same Cell Links Gene Expression to Dynamic Patterns of NF-κB Activation,” *Cell Syst.*, vol. 4, no. 4, pp. 458-469.e5, 2017.

[32] T. D. Scott, K. Sweeney, and M. N. McClean, “Biological signal generators: integrating synthetic biology tools and in silico control,” *Curr. Opin. Syst. Biol.*, vol. 14, pp. 58–65, Feb. 2019.

[33] A. P. Gasch *et al.*, “Single-cell RNA sequencing reveals intrinsic and extrinsic regulatory heterogeneity in yeast responding to stress,” pp. 1–28, 2017.

[34] J. Gutin, A. Sadeh, A. Rahat, A. Aharoni, and N. Friedman, “Condition-specific genetic interaction maps reveal crosstalk between the cAMP/PKA and the HOG MAPK pathways in the activation of the general stress response,” *Mol. Syst. Biol.*, vol. 11, no. 10, p. 829, Oct. 2015.

[35] Z. Akhavanaghdam, J. Sinha, O. P. Tabbaa, and N. Hao, “Dynamic control of gene regulatory logic by seemingly redundant transcription factors,” *Elife*, vol. 5, no. September2016, pp. 1–17, 2016.

[36] T. C. Kichuk, “Lights up on organelles : Optogenetic tools to control subcellular structure and organization,” no. May 2020, 2021.

[37] D. Niopek *et al.*, “Engineering light-inducible nuclear localization signals for precise spatiotemporal control of protein dynamics in living cells,” *Nat. Commun.*, vol. 5, pp. 1–11, 2014.

[38] D. Niopek, P. Wehler, J. Roensch, R. Eils, and B. Di Ventura, “Optogenetic control of nuclear protein export,” *Nat. Commun.*, vol. 7, p. 10624, 2016.

[39] H. Yumerefendi *et al.*, “Control of protein activity and cell fate specification via light-mediated nuclear translocation,” *PLoS One*, vol. 10, no. 6, pp. 1–19, 2015.

[40] J. Boyes, P. Byfield, Y. Nakatani, and V. Ogryzko, “Regulation of activity of the transcription factor GATA-1 by acetylation,” *Nature*, vol. 396, no. 6711, pp. 594–598, Dec. 1998.

[41] P. Louphrasitthiphol *et al.*, “Tuning Transcription Factor Availability through Acetylation-Mediated Genomic Redistribution,” *Mol. Cell*, vol. 79, no. 3, pp. 472-487.e10, 2020.

[42] W. Gu and R. G. Roeder, “Activation of p53 sequence-specific DNA binding by acetylation of the p53 C-terminal domain,” *Cell*, vol. 90, no. 4, pp. 595–606, 1997.

[43] S. Dovat, T. Ronni, D. Russell, R. Ferrini, B. S. Cobb, and S. T. Smale, “A common mechanism for mitotic inactivation of C2H2 zinc finger DNA-binding domains,” *Genes Dev.*, vol. 16, no. 23, pp. 2985–2990, 2002.

[44] D. Jantz and J. M. Berg, “Reduction in DNA-binding affinity of Cys2His2 zinc finger proteins by linker phosphorylation,” *Proc. Natl. Acad. Sci. U. S. A.*, vol. 101, no. 20, pp. 7589–7593, 2004.

[45] R. Rizkallah, K. E. Alexander, and M. M. Hurt, “Global mitotic phosphorylation of C2H2 zinc finger protein linker peptides,” *Cell Cycle*, vol. 10, no. 19, pp. 3327–3336, 2011.

[46] L. feng Chen, Y. Mu, and W. C. Greene, “Acetylation of RelA at discrete sites regulates distinct nuclear functions of NF-κB,” *EMBO J.*, vol. 21, no. 23, pp. 6539–6548, Dec. 2002.

[47] R. Kiernan *et al.*, “Post-activation turn-off of NF-κB-dependent transcription is regulated by acetylation of p65,” *J. Biol. Chem.*, vol. 278, no. 4, pp. 2758–2766, 2003.

[48] C. D. Crawley *et al.*, “DNA damage-induced cytotoxicity is mediated by the cooperative interaction of phospho-NF-κB p50 and a single nucleotide in the κb-site,” *Nucleic Acids Res.*, vol. 41, no. 2, pp. 764–774, 2013.

[49] T. Siggers *et al.*, “Principles of dimer-specific gene regulation revealed by a comprehensive characterization of NF-κB family DNA binding,” *Nat. Immunol.*, vol. 13, no. 1, pp. 95–102, 2012.

[50] C. K. Ea and D. Baltimore, “Regulation of NF-κB activity through lysine monomethylation

of p65," *Proc. Natl. Acad. Sci. U. S. A.*, vol. 106, no. 45, pp. 18972–18977, 2009.

[51] S. M. Sykes *et al.*, "Acetylation of the p53 DNA-Binding Domain Regulates Apoptosis Induction," *Mol. Cell*, vol. 24, no. 6, pp. 841–851, 2006.

[52] F. He *et al.*, "Interaction between p53 N terminus and core domain regulates specific and nonspecific DNA binding," vol. 116, no. 18, 2019.

[53] M. Vonderach, D. P. Byrne, P. E. Barran, P. A. Eyers, and C. E. Eyers, "DNA Binding and Phosphorylation Regulate the Core Structure of the NF-κB p50 Transcription Factor," *J. Am. Soc. Mass Spectrom.*, vol. 30, no. 1, pp. 128–138, 2019.

[54] J. Stewart-Ornstein, C. Nelson, J. Derisi, J. S. Weissman, and H. El-Samad, "Msn2 coordinates a stoichiometric gene expression program," *Curr. Biol.*, vol. 23, no. 23, pp. 2336–2345, 2013.

[55] W. Reiter *et al.*, "Yeast Protein Phosphatase 2A-Cdc55 Regulates the Transcriptional Response to Hyperosmolarity Stress by Regulating Msn2 and Msn4 Chromatin Recruitment," *Mol. Cell. Biol.*, vol. 33, no. 5, pp. 1057–1072, 2013.

[56] K. Kolar, C. Knobloch, H. Stork, M. Žnidarič, and W. Weber, "OptoBase: A Web Platform for Molecular Optogenetics," *ACS Synth. Biol.*, vol. 7, no. 7, pp. 1825–1828, Jul. 2018.

[57] K. Kolar and W. Weber, "Synthetic biological approaches to optogenetically control cell signaling," *Curr. Opin. Biotechnol.*, vol. 47, no. ii, pp. 112–119, 2017.

[58] L. J. Bugaj, G. P. O'Donoghue, and W. A. Lim, "Interrogating cellular perception and decision making with optogenetic tools," *J. Cell Biol.*, vol. 216, no. 1, pp. 25–28, Jan. 2017.

[59] K. P. Gerhardt *et al.*, "An open-hardware platform for optogenetics and photobiology," *Sci. Rep.*, vol. 6, no. November, pp. 1–13, 2016.

[60] "Iris," 2016. [Online]. Available: taborlab.github.io/Iris/.

[61] "TLC5941 Datasheet," 2008. [Online]. Available: www.ti.com/lit/ds/symlink/tlc5941.pdf.

[62] K. Sweeney, N. Moreno Morales, Z. Burmeister, A. J. Nimunkar, and M. N. McClean, "LPA Calibration Tools," 2019. [Online]. Available: github.com/mccleanlab/LPA-easy-calibrate.

[63] C. J. Stewart and M. N. McClean, "Design and implementation of an automated illuminating, culturing, and sampling system for microbial optogenetic applications," *J. Vis. Exp.*, vol. 2017, no. 120, p. 54894, 2017.

[64] J. Melendez, M. Patel, B. L. Oakes, P. Xu, P. Morton, and M. N. McClean, "Real-time optogenetic control of intracellular protein concentration in microbial cell cultures," *Integr. Biol. (United Kingdom)*, vol. 6, no. 3, pp. 366–372, 2014.

[65] M. A. Sheff and K. S. Thorn, "Optimized cassettes for fluorescent protein tagging in Saccharomyces cerevisiae," *Yeast*, vol. 21, no. 8, pp. 661–670, Jun. 2004.

[66] L. J. Bugaj and W. A. Lim, "High-throughput multicolor optogenetics in microwell plates," *Nat. Protoc.*, vol. 14, no. 7, pp. 2205–2228, 2019.

[67] K. Sweeney, N. Moreno Morales, Z. Burmeister, A. J. Nimunkar, and M. N. McClean, "Easy calibration of the Light Plate Apparatus for optogenetic experiments," *MethodsX*, vol. 6, pp. 1480–1488, 2019.

[68] E. O. S. Grødem and K. Sweeney, “optoPlate Calibration Tools,” 2020. [Online]. Available: github.com/mccleanlab/optoplate-96.

[69] H. E. Johnson, Y. Goyal, N. L. Pannucci, T. Schüpbach, S. Y. Shvartsman, and J. E. Toettcher, “The Spatiotemporal Limits of Developmental Erk Signaling,” *Dev. Cell*, vol. 40, no. 2, pp. 185–192, 2017.

[70] M. E. Lee, W. C. DeLoache, B. Cervantes, and J. E. Dueber, “A Highly Characterized Yeast Toolkit for Modular, Multipart Assembly,” *ACS Synth. Biol.*, vol. 4, no. 9, pp. 975–986, 2015.

[71] E. O. S. Grødem, K. Sweeney, and M. N. McClean, “Automated calibration of optoPlate LEDs to reduce light dose variation in optogenetic experiments,” *Biotechniques*, vol. 69, no. 4, pp. 313–316, 2020.

[72] P. Morel, “Gramm: grammar of graphics plotting in Matlab,” *J. Open Source Softw.*, vol. 3, no. 23, p. 568, 2018.

[73] L. Balkay, “fca_readfcs.” MATLAB Central File Exchange, 2022.

[74] K. Bodvard *et al.*, “Light-sensing via hydrogen peroxide and a peroxiredoxin,” *Nat. Commun.*, vol. 8, 2017.

[75] N. Hao, B. a Budnik, J. Gunawardena, and E. K. O’Shea, “Tunable Signal Processing Through Modular Control of Transcription Factor Translocation,” *Science (80-.).*, vol. 339, no. 6118, pp. 460–464, Jan. 2013.

[76] E. M. Zhao, M. A. Lalwani, J. M. Chen, P. Orillac, J. E. Toettcher, and J. L. Avalos, “Optogenetic Amplification Circuits for Light-Induced Metabolic Control,” *ACS Synth. Biol.*, vol. 10, no. 5, pp. 1143–1154, 2021.

[77] F. H. Lam, D. J. Steger, and E. K. O’Shea, “Chromatin decouples promoter threshold from dynamic range,” *Nature*, vol. 453, no. 7192, pp. 246–250, 2008.

[78] E. Sharon *et al.*, “Inferring gene regulatory logic from high-throughput measurements of thousands of systematically designed promoters,” *Nat. Biotechnol.*, vol. 30, no. 6, pp. 521–530, 2012.

[79] E. Durchschlag, W. Reiter, G. Ammerer, and C. Schüller, “Nuclear localization destabilizes the stress-regulated transcription factor Msn2,” *J. Biol. Chem.*, vol. 279, no. 53, pp. 55425–55432, 2004.

[80] A. Sadeh, N. Movshovich, M. Volokh, L. Gheber, and A. Aharoni, “Fine-tuning of the Msn2/4-mediated yeast stress responses as revealed by systematic deletion of Msn2/4 partners,” *Mol. Biol. Cell*, vol. 22, no. 17, pp. 3127–3138, 2011.

[81] S. Lallet, H. Garreau, C. Poisier, E. Boy-Marcotte, and M. Jacquet, “Heat shock-induced degradation of Msn2p, a Saccharomyces cerevisiae transcription factor, occurs in the nucleus,” *Mol. Genet. Genomics*, vol. 272, no. 3, pp. 353–362, Oct. 2004.

[82] J. Crocker, E. Preger-Ben Noon, and D. L. Stern, *The Soft Touch: Low-Affinity Transcription Factor Binding Sites in Development and Evolution*, 1st ed., vol. 117. Elsevier Inc., 2016.

[83] V. Pfanzagl *et al.*, “A constitutive active allele of the transcription factor Msn2 mimicking low PKA activity dictates metabolic remodeling in yeast,” *Mol. Biol. Cell*, vol. 29, no. 23, pp. 2848–2862, 2018.

[84] A. K. Aditham, C. J. Markin, D. A. Mokhtari, N. DelRosso, and P. M. Fordyce, "High-Throughput Affinity Measurements of Transcription Factor and DNA Mutations Reveal Affinity and Specificity Determinants," *Cell Syst.*, vol. 12, no. 2, pp. 112-127.e11, 2021.

[85] Y. Lin, C. H. Sohn, C. K. Dalal, L. Cai, and M. B. Elowitz, "Combinatorial gene regulation by modulation of relative pulse timing," *Nature*, vol. 527, no. 7576, pp. 54–58, 2015.

[86] D. Benzinger, S. Ovinnikov, and M. Khammash, "Synthetic gene networks recapitulate dynamic signal decoding and differential gene expression," *Cell Syst.*, vol. 13, no. 5, pp. 353-364.e6, May 2022.

[87] C. R. Lickwar, F. Mueller, S. E. Hanlon, J. G. McNally, and J. D. Lieb, "Genome-wide protein-DNA binding dynamics suggest a molecular clutch for transcription factor function," *Nature*, vol. 484, no. 7393, pp. 251–255, 2012.

[88] M. Chapal, S. Mintzer, S. Brodsky, M. Carmi, and N. Barkai, "Resolving noise-control conflict by gene duplication," *PLoS Biol.*, vol. 17, no. 11, pp. 1–25, 2019.

[89] T. Siggers, J. Reddy, B. Barron, and M. L. Bulyk, "Diversification of transcription factor paralogs via noncanonical modularity in C2H2 Zinc finger DNA binding," *Mol. Cell*, vol. 55, no. 4, pp. 640–648, 2014.

[90] N. Shen *et al.*, "Divergence in DNA Specificity among Paralogous Transcription Factors Contributes to Their Differential In Vivo Binding Article Divergence in DNA Specificity among Paralogous Transcription Factors Contributes to Their Differential In Vivo Binding," *Cell Syst.*, vol. 6, no. 4, pp. 470-483.e8, 2018.

[91] J. Gutin, D. Joseph-Strauss, A. Sadeh, E. Shalom, and N. Friedman, "Genetic screen of the yeast environmental stress response dynamics uncovers distinct regulatory phases," *Mol. Syst. Biol.*, vol. 15, no. 8, pp. 1–16, 2019.

[92] S. Li, D. M. Giardina, and M. L. Siegal, "Control of nongenetic heterogeneity in growth rate and stress tolerance of Saccharomyces cerevisiae by cyclic AMP-regulated transcription factors," *PLoS Genet.*, vol. 14, no. 11, pp. 1–42, 2018.

[93] K. V. Bhere, R. A. Haney, N. A. Ayoub, and J. E. Garb, "Gene structure, regulatory control, and evolution of black widow venom latrotoxins," *FEBS Lett.*, vol. 588, no. 21, pp. 3891–3897, 2014.

[94] M. A. Lalwani, H. Kawabe, R. L. Mays, S. M. Ho, and J. L. Avalos, "Optogenetic Control of Microbial Consortia Populations for Chemical Production," 2021.

[95] E. M. Zhao *et al.*, "Optogenetic regulation of engineered cellular metabolism for microbial chemical production," *Nature*, vol. 555, no. 7698, pp. 683–687, 2018.

[96] F. Estruch, "Two Homologous Zinc Finger Genes Identified by Multicopy Suppression in a SNF1 Protein Kinase Mutant of Saccharomyces cerevisiae," vol. 13, no. 7, pp. 3872–3881, 1993.

[97] M. T. Martínez-Pastor, G. Marchler, C. Schüller, A. Marchler-Bauer, H. Ruis, and F. Estruch, "The Saccharomyces cerevisiae zinc finger proteins Msn2p and Msn4p are required for transcriptional induction through the stress-response element (STRE)," *EMBO J.*, vol. 15, no. 9, pp. 2227–2235, 1996.

[98] A. C. Bergen, J. Hose, M. McClean, and A. P. Gasch, "Integrating multiple single-cell phenotypes links stress acclimation to prior life history in yeast," *bioRxiv*, p.

2021.09.08.459442, 2021.

[99] V. De Wever, W. Reiter, A. Ballarini, G. Ammerer, and C. Brocard, “A dual role for PP1 in shaping the Msn2-dependent transcriptional response to glucose starvation,” *EMBO J.*, vol. 24, no. 23, pp. 4115–4123, 2005.

[100] C. Garmendia-Torres, A. Goldbeter, and M. Jacquet, “Nucleocytoplasmic Oscillations of the Yeast Transcription Factor Msn2: Evidence for Periodic PKA Activation,” *Curr. Biol.*, vol. 17, no. 12, pp. 1044–1049, 2007.

[101] R. Martinez-Corral, E. Raimundez, Y. Lin, M. B. Elowitz, and J. Garcia-Ojalvo, “Self-Amplifying Pulsatile Protein Dynamics without Positive Feedback,” *Cell Syst.*, vol. 7, no. 4, pp. 453-462.e1, 2018.

[102] Y. Jiang, Z. AkhavanAghdam, L. S. Tsimring, and N. Hao, “Coupled feedback loops control the stimulus-dependent dynamics of the yeast transcription factor Msn2,” *J. Biol. Chem.*, vol. 292, no. 30, pp. 12366–12372, 2017.

[103] A. A. Granados, J. M. J. Pietsch, S. A. Cepeda-humerez, I. L. Farquhar, and P. S. Swain, “Distributed and dynamic intracellular organization of extracellular information,” 2018.

[104] E. Boy-Marcotte, C. Garmendia, H. Garreau, S. Lallet, L. Mallet, and M. Jacquet, “The transcriptional activation region of Msn2p, in Saccharomyces cerevisiae, is regulated by stress but is insensitive to the cAMP signalling pathway,” *Mol. Genet. Genomics*, vol. 275, no. 3, pp. 277–287, 2006.

[105] A. Sadeh, D. Baran, M. Volokh, and A. Aharoni, “Conserved motifs in the Msn2-activating domain are important for Msn2-mediated yeast stress response,” 2012.

[106] S. Lallet *et al.*, “Role of Gal11 , a component of the RNA polymerase II mediator in stress-induced hyperphosphorylation of Msn2 in Saccharomyces cerevisiae,” vol. 62, no. September, pp. 438–452, 2006.

[107] W. Görner *et al.*, “Acute glucose starvation activates the nuclear localization signal of a stress-specific yeast transcription factor,” *EMBO J.*, vol. 21, no. 1–2, pp. 135–144, 2002.

[108] N. Elfving, R. V. Chereji, V. Bharatula, S. Björklund, A. V. Morozov, and J. R. Broach, “A dynamic interplay of nucleosome and Msn2 binding regulates kinetics of gene activation and repression following stress,” *Nucleic Acids Res.*, vol. 42, no. 9, pp. 5468–5482, 2014.

[109] T. Y. Erkina, P. A. Tschetter, and A. M. Erkine, “Different Requirements of the SWI / SNF Complex for Robust Nucleosome Displacement at Promoters of Heat Shock Factor and Msn2- and Msn4-Regulated Heat Shock Genes □,” vol. 28, no. 4, pp. 1207–1217, 2008.

[110] S. Brodsky *et al.*, “Intrinsically Disordered Regions Direct Transcription Factor In Vivo Binding Specificity II,” *Mol. Cell*, vol. 79, no. 3, pp. 459-471.e4, 2020.

[111] Y. Hirata, T. Andoh, T. Asahara, and A. Kikuchi, “Yeast Glycogen Synthase Kinase-3 Activates Msn2p-dependent Transcription of Stress Responsive Genes,” *Mol. Biol. Cell*, vol. 14, no. 1, pp. 302–312, Jan. 2003.

[112] M. Linkert *et al.*, “Metadata matters: Access to image data in the real world,” *J. Cell Biol.*, vol. 189, no. 5, pp. 777–782, 2010.

[113] K. Sweeney, “Flow cytometry tools,” 2022. [Online]. Available: github.com/mccleanlab/nomoflowjo.

[114] N. E. Davey and D. O. Morgan, “Building a Regulatory Network with Short Linear Sequence Motifs: Lessons from the Degrons of the Anaphase-Promoting Complex,” *Molecular Cell*, vol. 64, no. 1. Elsevier Inc., pp. 12–23, 2016.

[115] N. E. Davey and D. 0 Morgan, “APC/C degron respository,” 2016. [Online]. Available: http://slim.icr.ac.uk/apc/index.php?page=degrons.

[116] M. Dobretsov and D. Romanovsky, “‘ Clock-scan ’ protocol for image analysis,” vol. 72205, pp. 869–879, 2022.

[117] N. M. Morales, M. T. Patel, C. J. Stewart, K. Sweeney, and M. N. Mcclean, “Optogenetic Tools for Control of Public Goods in Saccharomyces cerevisiae.”

[118] S. Gaudet and K. Miller-Jensen, “Redefining Signaling Pathways with an Expanding Single-Cell Toolbox,” *Trends Biotechnol.*, vol. 34, no. 6, pp. 458–469, 2016.

[119] J. E. Purvis and G. Lahav, “Encoding and decoding cellular information through signaling dynamics,” *Cell*, vol. 152, no. 5, pp. 945–956, 2013.

[120] M. Z. Wilson, P. T. Ravindran, W. A. Lim, and J. E. Toettcher, “Tracing Information Flow from Erk to Target Gene Induction Reveals Mechanisms of Dynamic and Combinatorial Control,” *Mol. Cell*, vol. 67, no. 5, pp. 757-769.e5, 2017.

[121] L. J. Bugaj *et al.*, “Cancer mutations and targeted drugs can disrupt dynamic signal encoding by the Ras-Erk pathway,” *Science (80-.).*, vol. 361, no. 6405, 2018.

[122] E. J. Olson, L. A. Hartsough, B. P. Landry, R. Shroff, and J. J. Tabor, “Characterizing bacterial gene circuit dynamics with optically programmed gene expression signals,” *Nat. Methods*, vol. 11, no. 4, pp. 449–455, 2014.

[123] E. J. Olson, C. N. Tzouanas, and J. J. Tabor, “A photoconversion model for full spectral programming and multiplexing of optogenetic systems,” *Mol. Syst. Biol.*, vol. 13, no. 4, p. 926, 2017.

[124] W. R. Farmer and J. C. Liao, “Improving lycopene production in Escherichia coli by engineering metabolic control,” *Nat. Biotechnol.*, vol. 18, no. 5, pp. 533–537, 2000.

[125] Y. Siu, J. Fenno, J. M. Lindle, and M. J. Dunlop, “Design and Selection of a Synthetic Feedback Loop for Optimizing Biofuel Tolerance,” *ACS Synth. Biol.*, vol. 7, no. 1, pp. 16–23, 2018.

[126] G. Lillacci, Y. Benenson, and M. Khammash, “Synthetic control systems for high performance gene expression in mammalian cells,” *Nucleic Acids Res.*, vol. 46, no. 18, pp. 9855–9863, 2018.

[127] O. Lipan and W. H. Wong, “The use of oscillatory signals in the study of genetic networks,” *Proc. Natl. Acad. Sci. U. S. A.*, vol. 102, no. 20, pp. 7063–7068, 2005.

[128] B. Mélykúti, E. August, A. Papachristodoulou, and H. El-Samad, “Discriminating between rival biochemical network models: Three approaches to optimal experiment design,” *BMC Syst. Biol.*, vol. 4, 2010.

[129] T. S. Shimizu, Y. Tu, and H. C. Berg, “A modular gradient-sensing network for chemotaxis in Escherichia coli revealed by responses to time-varying stimuli,” *Mol. Syst. Biol.*, vol. 6, no. 1, p. 382, Jan. 2010.

[130] C. J. Wang, A. Bergmann, B. Lin, K. Kim, and A. Levchenko, “Diverse sensitivity thresholds

in dynamic signaling responses by social amoebae," *Sci. Signal.*, vol. 5, no. 213, pp. 1–12, 2012.

[131] D. Muzzey, C. A. Gómez-Uribe, J. T. Mettetal, and A. van Oudenaarden, "A Systems-Level Analysis of Perfect Adaptation in Yeast Osmoregulation," *Cell*, vol. 138, no. 1, pp. 160–171, 2009.

[132] J. F. Apgar, J. E. Toettcher, D. Endy, F. M. White, and B. Tidor, "Stimulus design for model selection and validation in cell signaling," *PLoS Comput. Biol.*, vol. 4, no. 2, p. e30, 2008.

[133] E. J. Olson and J. J. Tabor, "Optogenetic characterization methods overcome key challenges in synthetic and systems biology," *Nat. Chem. Biol.*, vol. 10, no. 7, pp. 502–511, 2014.

[134] M. D. Engstrom and B. F. Pfleger, "Transcription control engineering and applications in synthetic biology," *Synth. Syst. Biotechnol.*, vol. 2, no. 3, pp. 176–191, 2017.

[135] J. Uhlendorf *et al.*, "Long-term model predictive control of gene expression at the population and single-cell levels," *Proc. Natl. Acad. Sci. U. S. A.*, vol. 109, no. 35, pp. 14271–14276, 2012.

[136] F. Menolascina *et al.*, "In-Vivo Real-Time Control of Protein Expression from Endogenous and Synthetic Gene Networks," *PLoS Comput. Biol.*, vol. 10, no. 5, 2014.

[137] G. Fiore, G. Perrino, M. Di Bernardo, and D. Di Bernardo, "In Vivo Real-Time Control of Gene Expression: A Comparative Analysis of Feedback Control Strategies in Yeast," *ACS Synth. Biol.*, vol. 5, no. 2, pp. 154–162, 2016.

[138] R. S. McIsaac *et al.*, "Fast-acting and nearly gratuitous induction of gene expression and protein depletion in Saccharomyces cerevisiae," *Mol. Biol. Cell*, vol. 22, no. 22, pp. 4447–4459, 2011.

[139] A. K. Brödel, A. Jaramillo, and M. Isalan, "Engineering orthogonal dual transcription factors for multi-input synthetic promoters," *Nat. Commun.*, vol. 7, p. 13858, 2016.

[140] R. W. Bradley, M. Buck, and B. Wang, "Tools and Principles for Microbial Gene Circuit Engineering," *J. Mol. Biol.*, vol. 428, no. 5, pp. 862–888, 2016.

[141] C. Fracassi, L. Postiglione, G. Fiore, and D. Di Bernardo, "Automatic Control of Gene Expression in Mammalian Cells," *ACS Synth. Biol.*, vol. 5, no. 4, pp. 296–302, 2016.

[142] C. Dong, J. Fontana, A. Patel, J. M. Carothers, and J. G. Zalatan, "Synthetic CRISPR-Cas gene activators for transcriptional reprogramming in bacteria," *Nat. Commun.*, vol. 9, no. 1, 2018.

[143] K. Kundert *et al.*, "Controlling CRISPR-Cas9 with ligand-activated and ligand-deactivated sgRNAs," *Nat. Commun.*, vol. 10, no. 1, pp. 1–11, 2019.

[144] P. Hersen, M. N. McClean, L. Mahadevan, and S. Ramanathan, "Signal processing by the HOG MAP kinase pathway," *Proc. Natl. Acad. Sci. U. S. A.*, vol. 105, no. 20, pp. 7165–7170, 2008.

[145] J. E. Toettcher, D. Gong, W. A. Lim, and O. D. Weiner, "Light-based feedback for controlling intracellular signaling dynamics," *Nat. Methods*, vol. 8, no. 10, pp. 837–839, 2011.

[146] M. J. Kennedy, R. M. Hughes, L. A. Peteya, J. W. Schwartz, M. D. Ehlers, and C. L. Tucker,

"Rapid blue-light-mediated induction of protein interactions in living cells," *Nat. Methods*, vol. 7, no. 12, pp. 973–975, 2010.

[147] A. Milias-Argeitis, M. Rullan, S. K. Aoki, P. Buchmann, and M. Khammash, "Automated optogenetic feedback control for precise and robust regulation of gene expression and cell growth," *Nat. Commun.*, vol. 7, no. May, pp. 1–11, 2016.

[148] R. Chait, J. Ruess, T. Bergmiller, G. Tkačik, and C. C. Guet, "Shaping bacterial population behavior through computer-interfaced control of individual cells," *Nat. Commun.*, vol. 8, no. 1, 2017.

[149] D. Benzinger and M. Khammash, "Pulsatile inputs achieve tunable attenuation of gene expression variability and graded multi-gene regulation," *Nat. Commun.*, vol. 9, no. 1, 2018.

[150] M. Rullan, D. Benzinger, G. W. Schmidt, A. Milias-Argeitis, and M. Khammash, "An Optogenetic Platform for Real-Time, Single-Cell Interrogation of Stochastic Transcriptional Regulation," *Mol. Cell*, vol. 70, no. 4, pp. 745-756.e6, 2018.

[151] J. G. Albeck, G. B. Mills, and J. S. Brugge, "Frequency-Modulated Pulses of ERK Activity Transmit Quantitative Proliferation Signals," *Mol. Cell*, vol. 49, no. 2, pp. 249–261, 2013.

[152] J. E. Toettcher, O. D. Weiner, and W. A. Lim, "Using Optogenetics to Interrogate the Dynamic Control of Signal Transmission by the Ras/Erk Module," *Cell*, vol. 155, no. 6, pp. 1422–1434, Dec. 2013.

[153] J. B. Lugagne, S. Sosa Carrillo, M. Kirch, A. Köhler, G. Batt, and P. Hersen, "Balancing a genetic toggle switch by real-time feedback control and periodic forcing," *Nat. Commun.*, vol. 8, no. 1, pp. 1–7, 2017.

[154] P. Harrigan, H. D. Madhani, and H. El-Samad, "Real-Time Genetic Compensation Defines the Dynamic Demands of Feedback Control," *Cell*, vol. 175, no. 3, pp. 877-886.e10, 2018.